

Characterization at the Atomistic Level of Defective Structures in Complex Materials: A Theoretical Study

THÈSE N° 8071 (2017)

PRÉSENTÉE LE 20 DÉCEMBRE 2017
À LA FACULTÉ DES SCIENCES DE BASE
LABORATOIRE DE SPECTROSCOPIE ET MICROSCOPIE ÉLECTRONIQUE
PROGRAMME DOCTORAL EN PHYSIQUE

ÉCOLE POLYTECHNIQUE FÉDÉRALE DE LAUSANNE

POUR L'OBTENTION DU GRADE DE DOCTEUR ÈS SCIENCES

PAR

Piyush AGRAWAL

acceptée sur proposition du jury:

Prof. V. Savona, président du jury
Prof. C. Hébert, Dr R. Erni, directeurs de thèse
Dr D. Passerone, rapporteur
Prof. U. J. Aschauer, rapporteur
Prof. D. Damjanovic, rapporteur



ÉCOLE POLYTECHNIQUE
FÉDÉRALE DE LAUSANNE

Suisse
2017



Acknowledgements

First of all, I would like to thank Dr. Rolf Erni and Dr. Daniele Passerone for their unfailing support and assistance during my PhD research. Thanks Rolf and Daniele, for patiently and skillfully guiding me all the time during these years of PhD.

A special thanks to Prof. Cécile Hébert for her continuous support over the past four years. Cécile, your several to and fro trips from Lausanne to EMPA and fruitful discussions with you has been invaluable to me.

I am also grateful to Dr. Marta D. Rossell for her efforts in the experiments for my projects. It was a privilege to work with you, from paper writing, scientific discussion to bridge experimental results and theoretical outputs.

A special gratitude goes to SNSF foundation for helping and providing the funding for the work.

I would also like to thank all the group members, both Electron Microscopy and Computational Materials Sciences groups at EMPA, Dübendorf. It was great sharing laboratory with you over last four years. Thanks for all your encouragement!

For chapter 2 and 4, the experimental HAADF/ABF, EDX and EELS measurements were carried out by Dr. Marta D. Rossell. EDX and HAADF experiments in chapter 3 were also carried out by Nicolas Bologna and the GaAs nanowires were grown by Moritz Knödler.

Acknowledgements

I also want to thanks Pu Yu and J. Guo for providing us the samples of SrMnO_3 for further measurements of EELS (chapter 2.2). I would also like to thanks Dr. Arthur Braun and Dr. Selma Erat for X-ray measurements of LFO and LFNO (chapter 2.3). I would like to specially thanks Prof. Andrew Rappe and his group at University of Pennsylvania for providing us the BVVS potentials within LAMMPS to simulate edge dislocation structure in BiFeO_3 (chapter 3). I also want to thanks Dr. Marco Campanini for his discussion about edge dislocation and for his ongoing experiments of electron holography on BiFeO_3 .

Words are short to express gratitude towards my beloved grandparents, parents, my wife, my sister and my all family members for their love and continuous support.

Abstract

Defects are key to enhance or deploy particular materials properties. In this thesis I present analyses of the impact of defects on the electronic structure of materials using combined experimental and theoretical Electron Energy Loss Spectroscopy (EELS) in (Scanning) Transmission Electron Microscopy (STEM/TEM). The energy loss near-edge structure (ELNES) in EELS reflects the element-specific electronic structure providing insights into bonding characteristics of individual atomic species. New electron optical devices have boosted the analytical capabilities by which materials can be investigated with atomic resolution and single atom sensitivity using STEM/TEM. With the help of aberration correctors for forming small electron probes, high intensity electron beams can nowadays be focused to clearly less than 100 pm which has enhanced the resolution and sensitivity in analytical STEM.

Various kinds of defects in different complex oxides were studied: point defects like oxygen vacancies in BiVO_4 and SrMnO_3 , edge-dislocations in BiFeO_3 , and planar defects in GaAs. By comparison with experimental data, structures for these systems were proposed based on the all-electron density functional theory (DFT) code Wien2k. By comparing theoretical calculations and experimental data, a pronounced surface reduction in the oxidation state of vanadium in BiVO_4 from +5 to +4 was unveiled, which is due to a high density of oxygen vacancies, and its importance in potential application of BiVO_4 in photoelectrochemical energy conversion. A similar study was performed on a series of SrMnO_3 thin films with different epitaxial strain where theoretical investigations revealed the impact of oxygen non-stoichiometry and strain on the O- K ELNES. In the next study, molecular dynamics simulations were combined with FEFF-based EELS calculations and its comparison with experiments was helpful

Abstract

for the correct prediction of the edge dislocation core structure in BiFeO_3 . This study also confirmed the presence of Fe atoms in the core of the edge dislocation which possibly makes these defects ferromagnetic whereas the bulk structure is known to be antiferromagnetic.

This thesis has established methodologies for utilizing different codes, illustrating how links between experimental and theoretical ELNES can be used in revealing structural information around defects and how defects affect materials properties. This tandem methodology of theory and experiments is applicable to various future materials where the reliable interpretation of EELS data is pivotal in unfolding mysteries of such technologically important materials.

Zusammenfassung

Defekte sind wichtig um Materialeigenschaften zu kontrollieren und zu verbessern. In dieser Arbeit präsentiere ich Analysen der Auswirkung von Defekten auf die elektronische Struktur von Materialien mittels einer Kombination aus experimenteller und theoretischer Elektronenenergieverlustspektroskopie (EELS) in der (Raster-) Transmissionselektronenmikroskopie (STEM/TEM). Die Energieverlust-Nahkantenstruktur (ELNES) in EELS spiegelt die elementspezifische elektronische Struktur wider, die Einblicke in die Bindungseigenschaften einzelner Atomspezies gewährt. Neue elektronenoptische Instrumente haben die analytischen Fähigkeiten erhöht, mit denen Materialien mit atomarer Auflösung und Einzelatomempfindlichkeit unter Verwendung von STEM/TEM untersucht werden können. Mit Hilfe von Aberrationskorrektoren zur Bildung kleiner Elektronensonden können nun hochintensive Elektronenstrahlen auf deutlich weniger als 100 pm fokussiert werden, was die Auflösung und Empfindlichkeit in analytischen STEM Anwendungen verbessert.

Verschiedene Arten von Kristalldefekten in komplexen Oxiden wurden untersucht: Punktdefekte wie Sauerstoffleerstellen in BiVO_4 und SrMnO_3 , Stufenversetzungen in BiFeO_3 und planare Defekte in GaAs. Im Vergleich zu experimentellen Daten basierten die berechneten Strukturen dieser Systeme auf dem All-Elektronendichtemessungstheorie (DFT) Algorithmus Wien2k. Durch Vergleich von theoretischen Berechnungen und experimentellen Daten wurde eine deutliche Oberflächenreduktion des Oxidationszustand von Vanadium in BiVO_4 von +5 auf +4 gefunden, was auf eine hohe Dichte an Sauerstoffleerstellen zurückzuführen ist, welche bedeutend für die photo-elektrochemische Energieumwandlung auf Basis von BiVO_4 ist. Eine ähnliche Studie wurde an einer Reihe von SrMnO_3 -Dünnschichten mit unterschiedlichen epitaktischen Spannungszustän-

Zusammenfassung

den durchgeführt, wobei theoretische Untersuchungen den Effekt von Sauerstoff-Nicht-Stöchiometrie und dessen Einfluss auf die O-K ELNES zeigten. In der nächsten Studie wurde aus einer Kombination von Molekulardynamik-Simulationen und FEFF-basierten EELS-Berechnungen ein Model für die Stufenversetzung in BiFeO_3 generiert, dessen Vergleich mit experimentellen Daten die Richtigkeit des Models besätigte. Diese Studie bestätigte auch das Vorhandensein von Fe-Atomen im Kern der Stufenversetzung, welches diese Defekte wahrscheinlich ferromagnetisch macht, wohingegen die ungestörte Struktur von BiFeO_3 bekanntermaßen antiferromagnetisch ist.

In dieser Arbeit wurden Methoden zur Nutzung verschiedener Algorithmen entwickelt, die zeigen, wie aus der Kombination von experimentellen und theoretischen ELNES Daten strukturelle Information über Defekte abzuleiten ist. Diese Tandem-Methodologie aus Theorie und Experimente ist auf verschiedene zukünftige Materialien anwendbar, wo zuverlässige Daten aus EELS-Daten Geheimnisse technologisch wichtiger Materialien aufdecken können.



List of Keywords

Complex oxides

Density Functional Theory

Electron Energy Loss Spectroscopy

Scanning Transmission Electron Microscopy

WIEN2k

Crystal defects

Edge dislocations

List of Abbreviations

- TMO..... Transition metal oxide
- STEM.... Scanning transmission electron microscopy
- DFT..... Density functional theory
- EELS.... Electron energy loss spectroscopy
- DDSCS... Double differential scattering cross section
- ELNES... Energy-loss near-edge structure
- EXELFS.. Extended energy-loss fine structure
- XANES... X-ray Absorption Near Edge Structure
- TEM..... Transmission Electron Microscopy
- LDA..... Local density approximation
- SCF..... Self-consistent field
- GGA..... Generalized gradient approximation
- HAADF.. High-angle annular dark field
- ABF.... Annular bright field
- MS..... Multiple scattering
- $v_{\text{O}}^{\bullet\bullet}$ oxygen vacancy with 2+ charge
- P-N..... Peierls Nabarro
- DOS..... density of states
- FEFF.... Abbreviation of the name of a code specialized in theoretical methods for spectroscopy.



Contents

Introduction	1
1 Techniques and Methods	4
1.1 Electron Microscopy (EM)	5
1.1.1 Transmission Electron Microscopy (TEM)	5
1.1.2 High Resolution TEM (HRTEM)	6
1.1.3 Scanning Transmission Electron Microscopy (STEM)	7
1.2 Spectroscopy in STEM	8
1.2.1 Electron Energy Loss Spectroscopy (EELS)	8
1.2.2 Core Loss EELS	11
1.3 Computing EELS Spectra	12
1.4 Density Functional Theory	14
1.4.1 Kohn-Sham Formalism	14
1.4.2 Exchange-Correlation Functional	15
1.4.3 Hybrid Functionals	16
1.4.4 DFT+ U	17
1.5 Bloch Theorem and K-point Sampling	18
1.6 WIEN2k	20
1.6.1 Calculating EELS Spectra	22
1.6.2 Calculating Bader Charges	22
1.6.3 Calculating Born Effective Charges	23
1.7 Real Space Green's Function Formalism (RSGF)	24
1.7.1 FEFF	25
1.7.2 XAS and EELS	26

Contents

1.7.3	General Approximation Used by the FEFF Code	26
1.7.4	Final State Rule and RPA	27
1.8	Comparison of WIEN2k and FEFF	28
1.9	Defects in Solids	29
1.10	Point Defects: Vacancies	29
1.11	Line Defect: Edge Dislocation	34
1.12	Planar Defects	40
2	Point Defects in Complex Oxides	43
2.1	Surface Reduction in Bismuth Vanadate - BiVO_4	43
2.1.1	Introduction	44
2.1.2	Experimental Section	45
2.1.3	Experimental Results	45
2.1.4	Highlights	51
2.1.5	Theoretical Calculation Details	52
2.1.6	Benchmarking the Models	53
2.1.7	Picture into Bonding and Charge Distribution	54
2.1.8	Conclusions	59
2.2	Strain Effects on Point Defects in SrMnO_3	61
2.2.1	Introduction	61
2.2.2	Experimental Details	62
2.2.3	Experimental Results	63
2.2.4	Highlights	67
2.2.5	Computational Details	68
2.2.6	Computational Results	69
2.2.7	Conclusion	74
2.3	Pre-peak in O- <i>K</i> Edge X-ray Spectra of Ni Substituted LaFeO_3	76
2.3.1	Introduction	76
2.3.2	Experimental Details	77
2.3.3	Highlights	79
2.3.4	Computational Details	80

2.3.5 Computational Results	80
2.3.6 Future Perspectives	81
2.4 Discussion	82
3 Line Defect: Edge Dislocation	83
3.1 Structural Configuration of Edge Dislocation Core in BiFeO ₃	83
3.1.1 Introduction	83
3.1.2 Experimental Details	85
3.1.3 Experimental Results	85
3.1.4 Highlights	88
3.1.5 Computational Details and Results	89
3.1.6 HAADF Image Simulations	95
3.1.7 EELS Calculated with FEFF	97
3.1.8 Conclusions	100
4 Planar Defects: Stacking Faults	101
4.1 Modeling Interacting Stacking Faults Resulting in Stair-rod Dislocations in GaAs Nanowires	101
4.1.1 Introduction	101
4.1.2 Experimental Details	102
4.1.3 Experimental Results	103
4.1.4 Highlights	106
4.1.5 Building the Stair-rod Dislocation Model and Computational De- tails	107
4.1.6 Computational Results	109
4.1.7 Conclusions	115
5 Conclusions and Outlook	117
5.1 Conclusions	117
5.2 Outlook	119
Bibliography	122

Contents

Curriculum Vitae

141



Introduction

Every segment of our daily lives is influenced by materials in one way or the other. Materials of different nature have numerous applications in medicine, electronics and various other consumer goods. Predicting, understanding and explaining the properties of a given material requires knowledge about its chemical composition, its dimensionality and, in particular, about the configuration and density of defects. The spectacular variation in the hardness of carbon when it transforms from diamond to graphite is the perfect example of the correlation of atomic structure of solids and its properties. In order to be able to derive an understanding about how the structure of a material is related to its physical properties, it is necessary to perform and understand experiments that unravel its atomic arrangement. With this knowledge, material scientists can tailor the properties to create custom or even brand new materials with properties designed for specific applications.

This dissertation concentrates on the characterization of defects in materials and profits from the following two facts which were helpful to investigate different material systems at the atomic level:

- 1) the availability of experimental techniques that allow to go to atomic resolution, even in complex systems like a crystal with defects;
- 2) the development of reliable modeling schemes (theory and algorithms) and the enhancement of computing resources, allowing to give insight and explain such experiments.

Modeling and experiments at the atomic level allow to study the influence of point, linear and two-dimensional modifications of the material on structural and electronic

Introduction

properties. The many applications envisaged of material “engineering” through defects can be more easily designed and realized thanks to the joint contributions of experiment and simulations. The present work reports the effort concerning modeling, mainly at the density functional theory level, embedded in a fruitful interplay with experimental techniques based on the electron microscopy and spectroscopy. My work which is reported in this thesis has concerned systems of different classes. The majority of them, however, can be ascribed to the category of complex oxides.

Crystals and defects in complex oxides

Transition metal oxides (TMOs) comprise a vast group of compounds that possess many possible functionalities like, for instance, ferroelectricity[1], ferromagnetism [2], and high-temperature superconductivity [3]. The nature of their electronic transport varies from insulating to semiconducting to metallic. The ABO_3 TMOs family which crystallizes into perovskite structure has received extensive attention. Figure 1 shows a model of the ABO_3 perovskite structure of TMO. The A and B sites support atoms with a wide range of size and number of valence electrons giving rise to a large variety of physical properties. TMOs are suited for the study of electron correlations, because the transition metal s electrons are transferred to the oxygen ions, and the remaining electrons are strongly correlated d ones. Furthermore, their properties are highly sensitive to perturbations from strain, structural defects, and various other effects providing new routes to engineer different functionalities in these materials. With growing interest in studying various defects in this kind of materials, there has been a sizeable amount of activity to manipulate known functionalities and also create new ones using these TMOs.

These functional materials rely on the ability to optimize electrical, magnetic and structural properties to enable new applications. The basis of this optimization lies in the control over defect behavior and formation, as the properties in question are inevitably linked to the nature and arrangement of such defects. Crystal defects can have a large impact on the characteristics and performance of a material affecting its

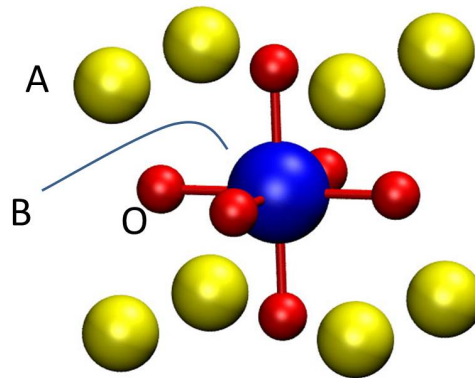


Figure 1 – Cartoon of ABO₃ type TMO where B is the transition metal.

electronic structure and physical properties. In the presence of higher impurity levels, controlling the formation and behavior of the defects is considerably more difficult. There are several factors responsible for the defect formation in the crystalline materials. Point defects are thermodynamically driven while others are due to the nature of the synthesis process or caused by plastic deformation of the material. Within TMOs, epitaxial thin films have attracted the attention of the research community especially because of their exceptional properties over polycrystalline thin films. Thin films show different physical properties than bulk materials because of the smaller size of the crystallites and in particular because of the presence of many crystallographic defects such as dislocations, vacancies, grain boundaries and stacking faults. Advances in thin film deposition have triggered intense research to understand how their structure is governing their functional properties in various devices[4–6]. Therefore, in order to design a material with a certain set of target properties, it is pivotal to characterize the defects and understand their impact on the electronic structure of the material.

This work focuses mainly on Electron Energy Loss (EEL) spectroscopy simulations performed on a model obtained via theoretical structure optimization validated by high-resolution Scanning Transmission Electron Microscopy (STEM) imaging. The validated model is further used to obtain insights about the impact of the defect on the local physical properties of the material. Properties of such defects play an important role in the control and optimization of physical properties of new materials.

1 Techniques and Methods

In order to investigate the functional properties of any kind of defects in crystalline three-dimensional materials, it is important to first characterize those defects and have a clear picture of the structural changes that occur at the atomic level. This information is helpful to build a theoretical model for calculating the physical properties of these defects and their effect on the material's properties. Among the many available experimental tools for investigating defects in crystalline materials, electron microscopy has emerged as a particularly powerful one. I will briefly introduce the experimental techniques, which are relevant for the current work, as the central part of the thesis focuses on theoretical investigations of the defects within complex oxides. I will discuss two main electron probe methods here: 1) Transmission Electron Microscopy, and 2) Scanning Transmission Electron Microscopy. I will also discuss several techniques within these two categories which are crucial in determining the structural arrangement of atoms and also the elemental composition at the atomic level. Then, I will give special emphasis on Electron Energy Loss Spectroscopy (EELS) which is the main theme of this dissertation. I will discuss both the experimental aspects as well as the theoretical background needed to get insights into EELS simulations.

1.1 Electron Microscopy (EM)

The wavelength λ of the radiation used for a particular microscopy technique is used to determine the maximum resolution available. Using Abbe's equation, one can determine the resolution limit, d , for a perfect microscope.

$$d = \frac{\lambda}{2n \sin(\alpha)} \quad (1.1)$$

where n is the refractive index of the medium and α is the half of the opening angle of the objective lens. In electron microscopy, electrons are accelerated with typically 60-300 kV and the wavelength of electrons can be thus 10^5 times smaller than that of light, resulting in a theoretical resolution limit to be smaller than (~ 50 pm) the interatomic distance. In an electron microscope, however, the actual resolution is determined by the lens aberrations and the stability of microscope.

1.1.1 Transmission Electron Microscopy (TEM)

TEM is a very powerful technique for investigating phenomena at the atomic level. Almost all kinds of solid samples can be characterized by TEM. In a TEM, the electrons are emitted by an electron gun at the top of the microscope and then accelerated by an anode at typically 60-300 kV with respect to the cathode. As shown in figure 1.1, the high energy electron beam is controlled by a set of electromagnetic lenses named condenser lenses. These condenser lenses are above the sample and have apertures which are used to select the maximum opening of the electron beam. The fast electrons then interact with the sample and are transmitted through the specimen and further focused by the objective lens to form the image. TEM provides high resolution, even capable of imaging atomic lattice patterns in high resolution TEM (HRTEM) images. Such an image formed by the objective lens is then magnified by a series of lenses and is recorded on a digital camera. Besides HRTEM, there are other image contrast formation mechanisms. In the bright field (BF) mode, the most common mode of operation, an aperture is placed in the back focal plane of the

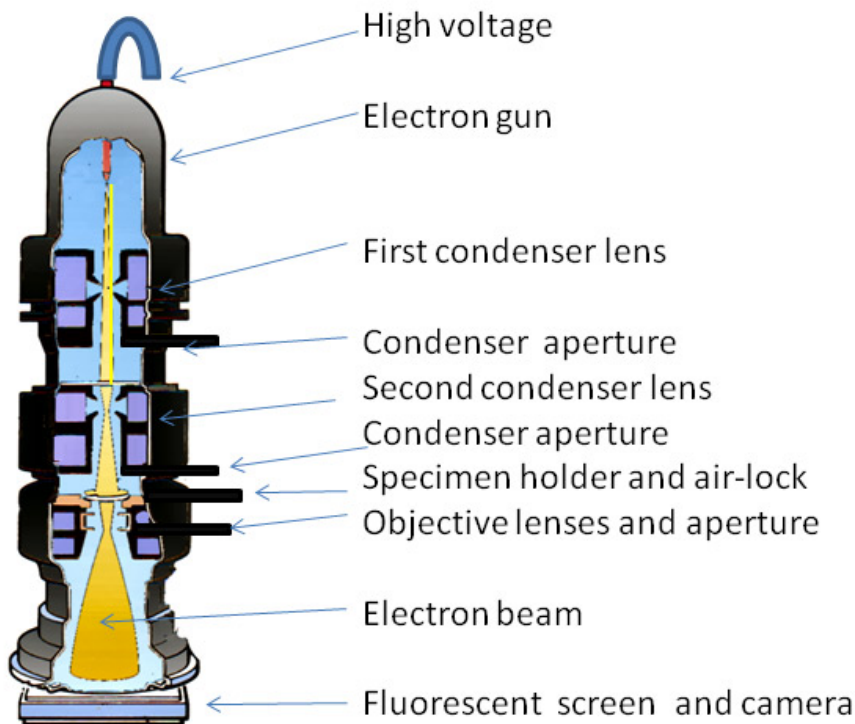


Figure 1.1 – Sketch of a Transmission Electron Microscope. Figure adapted from Ref[7].

objective lens which allows only the direct beam to pass. The image results from a weakening of the direct beam by its interaction with the sample. Therefore, mass-thickness and diffraction contrast contribute to the image formation. Conversely, in dark field (DF) mode, a diffracted beam is allowed to pass instead of the undiffracted beam. Dark field studies play an important role in studying linear and planar crystal defects such as dislocations or stacking faults at a resolution above 1 nm. In general, the contrast formation mechanism is more complex than briefly outlined here.

1.1.2 High Resolution TEM (HRTEM)

When the electron wave interacts with the sample, its phase changes relative to the unscattered incident wave. The contrast in an HRTEM image arises from the interference of the undiffracted beam with diffracted beams in the image plane. It is difficult to directly interpret the contrast as defocus and lens aberrations heavily influence the

image by applying phase shifts to the diffracted beams. The spherical and chromatic aberrations of the lens are responsible for the limited resolution of transmission electron microscopes. In spite of best efforts from lens designers, standard round lenses restrict the resolution to about 1.2 Å which is far above the wavelength of the electron. Often the resolution is derived by the spherical aberration and the wavelength of the incident electrons[8] and is given by the formula

$$D_{\text{res}} \approx C_s^{1/4} \lambda^{3/4} \quad (1.2)$$

where C_s is the coefficient of spherical aberration and λ is the wavelength of the incident electron. Rays away from the optical axis fail to converge at the same point and as a result, the image of a point object appears as a disk of finite size. The point resolution limit, therefore, can be improved either by reducing or eliminating C_s , or by decreasing λ or in other words by increasing the accelerating voltage of the microscope. In other routes, Scherzer[9] in 1947 proposed ways of correcting the spherical aberration. Multipole lenses are able to generate negative values of C_s and hence can cancel the positive C_s of the round lens. The chromatic aberration (C_c) is an effect resulting from dispersion in which the lens fails to converge rays of different wavelengths at the same focal point. This effect of C_c can be eliminated by ensuring that all electrons have the same energy, or by a complex corrector for C_c .

1.1.3 Scanning Transmission Electron Microscopy (STEM)

STEM is a variation of TEM where the electron beam is focused to a small probe and scanned over the sample. Similar to TEM, specimens for STEM are relatively thin and are suitable for several other techniques such as energy dispersive X-ray (EDX) spectroscopy, annular dark field imaging or electron energy loss spectroscopy. Aberration correctors enable electron probes to be focused to diameters in the sub-angstrom level and have made it possible to detect individual atomic columns in crystalline specimens. Figure 1.2 shows DF and BF STEM images of SrMnO₃. EELS in combination with STEM can be used for chemical mapping at atomic resolution. As

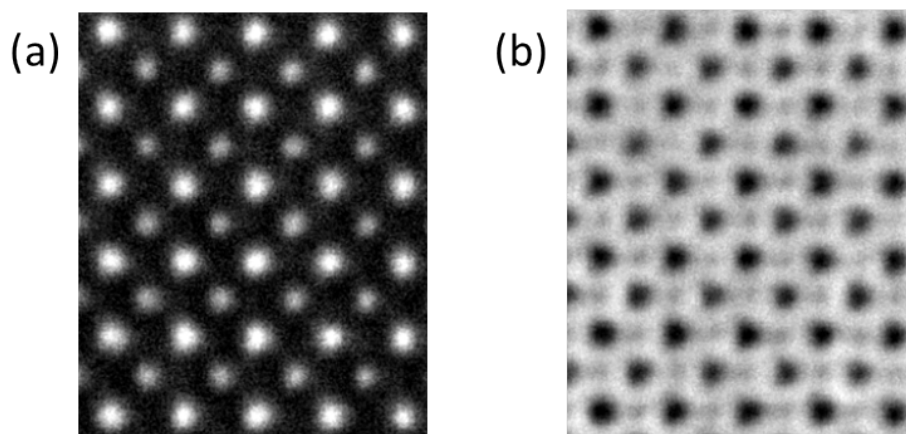


Figure 1.2 – (a) Dark-field and (b) bright-field STEM images of SrMnO₃ recorded by Marta Rossell.

shown in figure 1.3, there are three different kinds of detectors to record an image: a) Bright field (BF): this region represents the electrons with very small scattering angle. b) Annular bright field detector (ABF): is the outer rim of the BF detector. ABF signal is proportional to Z^n ($n \sim \frac{1}{3}$) and helps to record the electron scattering from atoms with low Z value in the presence of high Z value atoms. c) High Angle Annular dark field detector (HAADF): HAADF signal is proportional to Z^n ($n \sim 1.6 - 2.0$) and records electrons scattered at higher angles.

1.2 Spectroscopy in STEM

1.2.1 Electron Energy Loss Spectroscopy (EELS)

EELS is a technique where the energy lost by the electron, due to inelastic scattering, is measured by an electron spectrometer. It is used to identify features such as ionization edges or e.g. plasmons or valence losses. The valence losses are due to transitions, of electrons in the crystal, made between the valence states and the unoccupied states, which account for the low loss signals, whereas transition from core states account for core losses which shows an energy loss near edge structure (ELNES) that reflects the bonding state of the element. A typical EELS spectrum is shown in figure 1.4 and is divided into three different regions namely zero-loss, plasmon loss and ionization

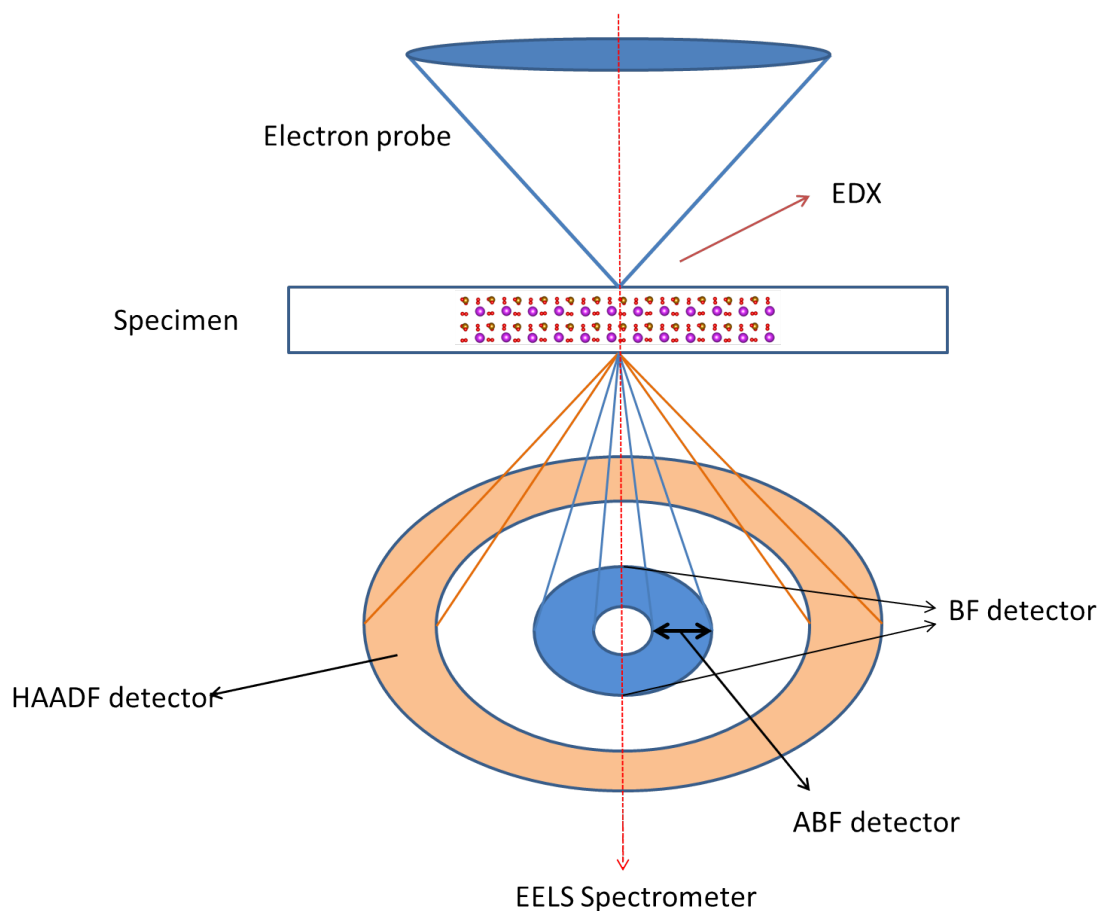


Figure 1.3 – Schematic diagram of common imaging modes in STEM.

edge regions. The zero loss peak is the most intense feature corresponding to electrons that undergo no energy loss while passing through the sample. The width of the zero loss peak gives a good idea of the energy resolution of the recorded spectrum which depends on the monochromaticity of the electron source of the microscope as well as on the stability of instrument. Modern day instruments with monochromator attain energy resolution of less than 0.2 eV. The next intense feature of an EELS spectrum is usually represented by the plasmon peak which is often a fairly broad peak ranging from 5-35 eV energy loss. The plasmon peak corresponds to collective oscillation of electrons.

The core-loss region corresponds to the excitation of electrons from inner core shells (K,L,M) of atoms in the specimen to unoccupied sites above the Fermi level. These

Chapter 1. Techniques and Methods

signals are termed as ionization edges and can be used for chemical analyses. Features in this signal represent the local bonding and coordination for that particular atom. These features provide insight into the electronic structure of the materials and further allow us to explore its properties. These features are divided into two regions, called Electron Energy Loss Near-Edge Structure (ELNES) and Extended Electron Energy Loss Fine Structure (EXELFS). Typically the first 30 eV region above the threshold is considered the ELNES and the region beyond 50 eV it is considered the EXELFS. The ELNES is interpreted as a signature of the local electronic structure giving information about bonding, charge transfer, configuration etc. The EXELFS, on the other hand, gives information about interatomic distances and coordination numbers [10, 11]. This dissertation focuses on core loss EELS and in particular on the ELNES to study the electronic structure of materials based on theoretical simulations.

For our research, most of the experimental data was obtained from a double-

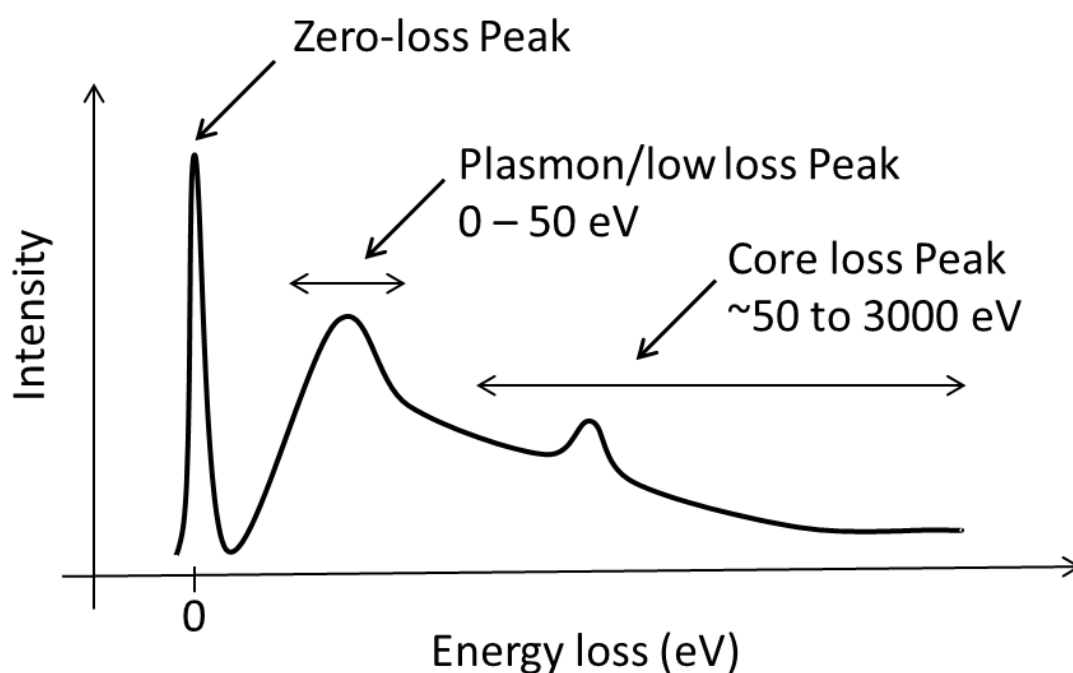


Figure 1.4 – Structure of EELS graph divided into three regions.

aberration-corrected cold-FEG STEM/TEM microscope which is equipped with high-resolution spectrometer with dual-EELS capabilities and operated at the facilities

at IBM Zurich. The experimental data for the work in this dissertation have been recorded by Dr. Marta D. Rossell. Having access to high-resolution core-loss EELS provides insight into the electronic structure of individual atomic species containing information about their bonding characteristics such as, e.g., charge transfer, oxidation state, and site coordination. Yet this information cannot be derived directly from EELS spectra, but is buried in the spectral fine structure which can be regarded as a fingerprint of the bonding characteristics.

1.2.2 Core Loss EELS

It was recognized by Hillier and Baker [12] that there is considerable relevance in measuring the energy lost by the incident electrons in inelastic collisions corresponding to the specific energy levels of electrons in various atomic orbitals. These specific energy levels indicate the elements present in the sample. The edges are named by the corresponding element and the core shell from where the excitation takes place. For e.g., O-*K* for the excitations from O 1s shell and Fe *L1* for the excitation from Fe 2s and Fe *L2*, *L3* for the excitation from Fe 2p.

From an experimental point of view, measuring an EEL spectrum and its analysis are challenging. If an inelastically scattered electron undergoes another energy loss event, that is termed as 'plural scattering'. One of the main challenges is to avoid plural scattering of the incident electrons while recording an EELS spectrum. The effect of plural scattering becomes dominant with increasing thickness of the sample. Because of this, it is best to work with thin samples. This corresponds to work with samples which have a thickness less than half the inelastic mean free path. In this dissertation, the thickness of different samples ranges from ≈ 40 -70 nm, for which inelastic mean free path ranges between ≈ 120 -160 nm.

1.3 Computing EELS Spectra

In EELS, the incident electrons inelastically interact with atoms of the specimen. This means that these electrons lose energy and are deflected from their original path. Figure 1.5 shows the scattering geometry of the incident electron after passing through the sample. The EELS spectrometer separates the transmitted electrons with their respective energy loss, and sums the number of electrons for each energy loss and produces the spectrum. The scattering geometry of the incident electrons can be

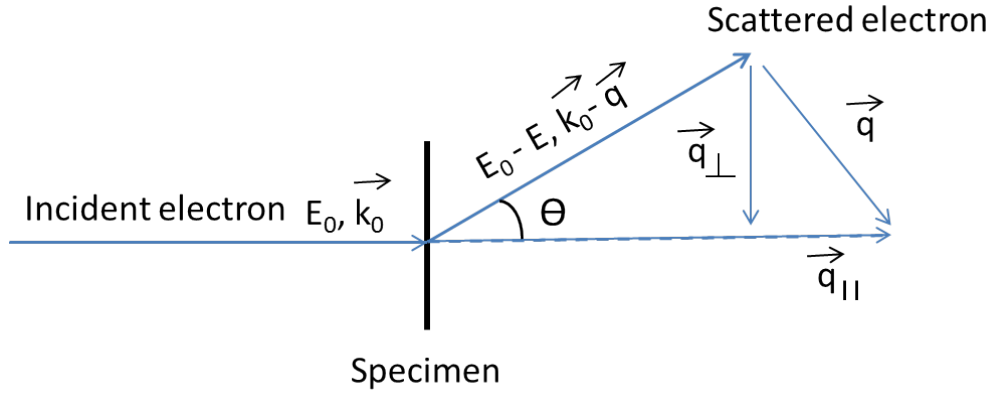


Figure 1.5 – Scheme of electron passing through the sample in electron microscope. Scattering geometry of incident electrons after passing through sample.

defined using the primary energy E_0 and the wave vector \vec{k}_0 as shown in figure 1.5. As the electron passes through the sample, it loses energy by E and changes its wave vector by \vec{q} . This wave vector transfer \vec{q} can be further broken down into parallel and perpendicular components. At the same time, the electron from the atom in the sample is excited from the initial state to the final state. The whole process is described using the double differential scattering cross section (DDSCS), proportional to the probability of finding an electron per unit of solid angle Ω and per unit of energy lost E , transferring wave vector \vec{q} to the sample. Using Fermi's golden rule, the expression is written as

$$\frac{\partial^2 \sigma}{\partial \Omega \partial E} = \left[\frac{4\gamma^2}{a_0^2 q^4} \right] \frac{k_f}{k_i} \sum_{i,f} |\langle f | e^{i\vec{q} \cdot \vec{r}} | i \rangle|^2 \delta(E_i - E_f - E) \quad (1.3)$$

1.3. Computing EELS Spectra

where E represents the energy loss, E_i and E_f are the energies of the initial and final states of the excited electron, respectively. The summation is performed over all occupied initial and unoccupied final electron states represented by the wave function i and f . Eq. 1.3 can be written in form of the unoccupied density of states (DOS) $\chi(E)$ using the approximation given by Nelheibel[13],

$$\frac{\partial^2 \sigma}{\partial \Omega \partial E}(E, q) = \sum_{l_F} |M_{l_F}(q, E)|^2 \chi_{l_F}(E) \quad (1.4)$$

where the unoccupied DOS is given by the $\chi_{l_F}(E)$ of the available states l_F (s,p,d) multiplied by the smooth and slowly decaying function represented as matrix $M_{l_F}(\vec{q}, E)$.

In another technique called X-ray absorption spectroscopy (XAS), similar absorption edges are measured. In this technique, instead of electrons, a beam of photons is used to excite core electrons into the unoccupied states. This makes the calculation of XAS similar to EELS. As in EELS, the DDSCS for XAS is expressed as,

$$\frac{\partial \sigma}{\partial E} \propto \sum_{i,f} |\langle f | \vec{\epsilon} \cdot \vec{r} | i \rangle|^2 \quad (1.5)$$

where $\vec{\epsilon}$ is the polarization vector which is equivalent to momentum transfer vector \vec{q} in EELS. The equivalent of ELNES is known as X-ray Absorption Near Edge Structure (XANES).

There are mainly two approaches available to calculate EELS spectra:

- 1) the approach based on Density Functional Theory (DFT) - used to calculate the density of unoccupied states $\chi_{l_F}(E)$.
- 2) the approach based on the Multiple Scattering (MS) theory - in this approach the excited electron in the final state is considered as a wave scattering off the atoms in the sample.

The work in this dissertation is based on both approaches where each of them has its specific advantages. In the next section, I will present these approaches.

1.4 Density Functional Theory

Density functional theory (DFT) was introduced by Hohenberg and Kohn[14] and it has been very popular since 1970 for solid state calculations after the implementation of the Kohn-Sham solution approach. In this section, I will discuss DFT to understand its application for calculating EEL spectra.

1.4.1 Kohn-Sham Formalism

The first Hohenberg-Kohn theorem[14] states that the external potential, and thus the total energy, of a many-electron system is uniquely determined by the electron density function which reduces the dimension to 3 instead of $3N$ for a wave function of a N -particle system. The external potential is also determined as a unique functional of the density. The second Hohenberg-Kohn theorem states that the minimum of the energy functional corresponds to the correct ground state electron density for the system.

According to Kohn-Sham[15] the Schrödinger equation of a system of non-interacting particles under an effective external potential produces the same density as any given system of interacting particles. This effective potential is defined by $V_s(\vec{r})$ or $V_{\text{eff}}(\vec{r})$ and is called Kohn-Sham potential. The Kohn-Sham equation [atomic units are used throughout] is expressed as

$$\left[\frac{-\nabla^2}{2} + V_{\text{ext}}(\vec{r}) + V_c[\rho(\vec{r})] + V_{\text{xc}}[\rho(\vec{r})] \right] \phi_i(\vec{r}) = \varepsilon_i \phi_i(\vec{r}) \quad (1.6)$$

$$\left(\frac{-\nabla^2}{2} + V_{\text{eff}}(\vec{r}) \right) \phi_i(\vec{r}) = \varepsilon_i \phi_i(\vec{r}) \quad (1.7)$$

And the Kohn-Sham potential is written as

$$V_{\text{eff}}(\vec{r}) = V_{\text{ext}}(\vec{r}) + e^2 \int \frac{\rho(\vec{r}')}{|\vec{r} - \vec{r}'|} d\vec{r}' + \frac{\partial E_{\text{xc}}[\rho]}{\partial \rho(\vec{r})} \quad (1.8)$$

where E_{xc} is the exchange correlation energy and the exchange correlation potential can be defined as

$$V_{xc}(\vec{r}) = \frac{\partial E_{xc}[\rho]}{\partial \rho(\vec{r})} \quad (1.9)$$

This potential also includes the correlation and exchange effects between the electrons. As an electron moves, the other electrons feel its Coulomb potential and thus the motion of all electrons is correlated. The exact solution of this problem is impossible even for simple systems, due to this correlation.

The total energy of a system is expressed as a functional of the charge density as,

$$E[\rho] = T_s[\rho] + \int V_{\text{ext}}(\vec{r})\rho(\vec{r})d\vec{r} + E_H[\rho] + E_{xc}[\rho] \quad (1.10)$$

where $T_s[\rho]$ is the Kohn-Sham kinetic energy, $E_H[\rho]$ is the Hartree energy.

1.4.2 Exchange-Correlation Functional

$E_{xc}[\rho]$ as defined in eq. 1.9 is the sum of a) the difference between the kinetic energies from the interacting particle system and the independent one and b) the difference between the real interaction energy of electrons and the Hartree energy. $E_{xc}[\rho]$ can be separated in two terms:

$$E_{xc}[\rho] = E_x[\rho] + E_c[\rho] \quad (1.11)$$

$E_x[\rho]$ the exchange energy and $E_c[\rho]$ the correlation energy. But the exact form of $E_{xc}[\rho]$ is unknown, which is one of the limitation of the Kohn-Sham approach. There are several approximations to the $E_{xc}[\rho]$ functional. The simplest approximation is the local density approximation (LDA)[15] which assumes that the density can be treated locally as for an homogeneous electron gas. In this approximation, the $E_{xc}[\rho]$ at each point solely depends on the value of electron density at that point and is taken to be that of an homogeneous electron gas which would have the density $\rho(\vec{r})$. As a further remedy, generalized gradient approximation (GGA) [16] was proposed by considering

the gradient of the density. But, this also fails where the density changes rapidly. Several other approximations can be found in literature for detailed study. Most of these functionals fail to define the localized nature of d or f electrons appropriately. Particularly for TMO, it is important to treat d -shell electrons correctly. The two main methodologies to deal with these shortcomings are hybrid functionals and the DFT+ U [17] method. I will describe both of these techniques briefly.

With the interest of this thesis, I focus on a particular hybrid functional known as Heyd-Scuseria-Ernzerhof (HSE) screened functional.

1.4.3 Hybrid Functionals

Practical applications of DFT are usually achieved by solving the Kohn-Sham equations, which map the original many-electron problem into an equivalent single-electron Hamiltonian. The practical success of the mapping depends on the nature of the approximate exchange and correlation functionals. One class of functionals which has gained considerable interest, is represented by the “hybrid functionals”. They are obtained by mixing a fixed amount of non-local Fock exchange to semi-local functionals. One of the most used functionals of this class is B3LYP[18, 19], which includes 20% of the exact exchange and has been very successful in study of thermochemistry of atoms and molecules. One such example of this class is HSE screened hybrid functional[20]. The Coulomb interaction operator is partitioned into short-range and long-range components, respectively:

$$\frac{1}{\vec{r}} = \frac{\text{erfc}(w\vec{r})}{\vec{r}} + \frac{\text{erf}(w\vec{r})}{\vec{r}} \quad (1.12)$$

where w is an adjustable parameter that describes the range of short-range interactions, $\text{erf}(w\vec{r})$ is the error function and $\text{erfc}(w\vec{r}) = 1 - \text{erf}(w\vec{r})$ is its complement. For HSE screened hybrid functional, the construction of the short range part is based on admixture of both HF and PBE-GGA exchange. The HSE exchange-correlation functional is expressed by:

$$E_{xc}^{HSE} = bE_x^{HF,SR}(w) + (1-b)E_x^{PBE,SR}(w) + E_x^{PBE,LR} + E_c^{PBE} \quad (1.13)$$

where b is the mixing parameter. For the HSE hybrid functional, b has a value of 0.25. The HSE functional with increased locality of Fock exchange as compared to PBE provides better agreement of the estimation of band-gaps to experimental results. The main shortcoming of the hybrid functional is that the mixing parameter b and range separation adds further complexity. So, another way of dealing with d and f -electrons is the Hubbard and Anderson model, which is used to approximate electron repulsion integrals locally for well-localized orbitals.

1.4.4 DFT+ U

The LDA and GGA functionals tend to delocalize electrons over the crystal. That's why they fail to describe the localized electrons (d and f electrons) correctly. A way to avoid this problem is to add an additional Hubbard-like term, to the LDA/GGA functional. This method is known as DFT+ U . The localized d or f orbitals are treated with strong on-site Coulomb interaction, while the rest of valence electrons are treated with standard approximate DFT functionals (LDA or GGA). The Hubbard Hamiltonian can be written as,

$$H_{\text{Hub}} = t \sum_{\langle i,j \rangle, \sigma} (c_{i,\sigma}^\dagger (c_{j,\sigma} + h.c.) + U \sum_i n_{i,\uparrow} n_{i,\downarrow}) \quad (1.14)$$

where $\langle i, j \rangle$ denotes nearest-neighbor atomic sites, $c_{i,\sigma}^\dagger$, $c_{j,\sigma}$ and $n_{i,\sigma}$ are electronic creation, annihilation and number operators for electrons of spin σ on site i . Using this equation, the motion of strongly localized electrons is described by a ‘‘hopping’’ process from one atomic site to its neighbors (first term of Eq. (1.14)) whose amplitude t is proportional to the dispersion (the bandwidth) of the valence electronic states and represents the single-particle term of the total energy. In virtue of the strong localization, the Coulomb repulsion is only accounted between electrons on the same atom through a term proportional to the product of the occupation numbers of atomic states on the same site, whose strength is U (the ‘‘Hubbard U ’’). The DFT+ U energy is

defined by,

$$E_{\text{DFT}+U} = E_{\text{DFT}} + E_{\text{Hub}} - E_{\text{dc}} \quad (1.15)$$

where E_{dc} is used to subtract the double counting term. This term is used to eliminate the already contained interaction energy in E_{Hub} from the DFT energy functional E_{LDA} . Generally, the delocalized s and p electrons are described well by LDA or GGA. But, quite often, the localized d orbitals require the DFT+ U treatment. There are several approaches available in the literature to incorporate the strong correlation between d electrons using DFT+ U method[15, 21, 22].

1.5 Bloch Theorem and K-point Sampling

To perform electronic structure calculations in solids, it is important to understand the method to handle the infinite crystal structure. In crystals, the arrangement of atoms is periodic. It is described in terms of the primitive lattice vectors \vec{a}_1 , \vec{a}_2 , \vec{a}_3 and the position of atoms inside a primitive unit cell. The lattice vectors \vec{R} are formed by all the possible combinations of primitive lattice vectors, multiplied by integers:

$$\vec{R} = n_1\vec{a}_1 + n_2\vec{a}_2 + n_3\vec{a}_3 \quad (1.16)$$

The basis for describing the behavior of electrons in a crystal is the reciprocal lattice, which is the inverse space of the real lattice. The reciprocal primitive lattice vectors are defined by:

$$\vec{b}_1 = \frac{2\pi(\vec{a}_2 \times \vec{a}_3)}{\vec{a}_1 \cdot (\vec{a}_2 \times \vec{a}_3)}, \quad \vec{b}_2 = \frac{2\pi(\vec{a}_3 \times \vec{a}_1)}{\vec{a}_2 \cdot (\vec{a}_3 \times \vec{a}_1)}, \quad \vec{b}_3 = \frac{2\pi(\vec{a}_1 \times \vec{a}_2)}{\vec{a}_3 \cdot (\vec{a}_1 \times \vec{a}_2)}, \quad (1.17)$$

Similar to eq. 1.16, the reciprocal lattice vectors \vec{G} can be written as:

$$\vec{G} = m_1\vec{b}_1 + m_2\vec{b}_2 + m_3\vec{b}_3 \quad (1.18)$$

1.5. Bloch Theorem and K-point Sampling

By construction, the dot product of any vector \mathbf{R} and vector \mathbf{G} is:

$$\vec{\mathbf{G}} \cdot \vec{\mathbf{R}} = 2\pi l, \text{ where } l = n_1 m_1 + n_2 m_2 + n_3 m_3 \quad (1.19)$$

where l is always an integer and this also gives:

$$e^{i\vec{\mathbf{G}} \cdot \vec{\mathbf{R}}} = 1 \quad (1.20)$$

According to Bloch's theorem, if potential V in the single-particle hamiltonian has the translational periodicity of the Bravais lattice, such that

$$V(\vec{\mathbf{r}}) = V(\vec{\mathbf{r}} + \vec{\mathbf{R}}) \quad (1.21)$$

then, the wave function of an electron in an infinite crystal can be written as,

$$\psi_{\vec{\mathbf{k}}}(\vec{\mathbf{r}}) = u_{\vec{\mathbf{k}}}(\vec{\mathbf{r}}) \cdot e^{i\vec{\mathbf{k}} \cdot \vec{\mathbf{r}}} \quad (1.22)$$

where $u_{\vec{\mathbf{k}}}(\vec{\mathbf{r}})$ has the same periodicity as of the potential V . The periodic part is indexed by $\vec{\mathbf{k}}$ can take as many values as there are periodic units N .

$$\vec{\mathbf{k}} = \frac{\pi n}{aN}, \text{ where } n = -\frac{N-1}{2}, \dots, 0, \dots, \frac{N-1}{2} \quad (1.23)$$

The function $u_{\vec{\mathbf{k}}}(\vec{\mathbf{r}})$ can be expanded as a set of plane waves,

$$u_{\vec{\mathbf{k}}}(\vec{\mathbf{r}}) = \sum_{\vec{\mathbf{G}}} c_{\vec{\mathbf{k}}}(\vec{\mathbf{G}}) e^{i\vec{\mathbf{G}} \cdot \vec{\mathbf{r}}} \quad (1.24)$$

where $\vec{\mathbf{G}}$ is the reciprocal lattice vector and $c_{\vec{\mathbf{k}}}(\vec{\mathbf{G}})$ is the Fourier expansion coefficient of the reciprocal lattice vector. The number of terms in this expansion in practical calculations is finite and determined by a parameter called cutoff which is set based on the required accuracy. To determine $u_{\vec{\mathbf{k}}}(\vec{\mathbf{r}})$, this form of wavefunction is inserted in the single-particle Schrödinger equation. Instead of solving the wave function over infinite space, it is solved for the restricted k-points which lie within the first Brillouin zone. The first Brillouin zone is a uniquely defined primitive cell in reciprocal space. So, for

Chapter 1. Techniques and Methods

large systems, the Brillouin zone is very small and only a few \mathbf{k} -points are required to describe the variation across the Brillouin zone accurately. This significantly simplifies the task of calculating quantities like electron density, written as:

$$\rho_{\vec{k}}(\vec{r}) = \sum_{n, \epsilon_{\vec{k}}^{(n)} < \epsilon_F} |\psi_{\vec{k}}^{(n)}(\vec{r})|^2, \quad \rho(\vec{r}) = \int \frac{d\vec{k}}{2\pi^3} \rho_{\vec{k}}(\vec{r}) \quad (1.25)$$

where $\vec{k} \equiv \text{BZ}$ stands for all values in Brillouin zone. Therefore, with the use of very few \mathbf{k} -points one can obtain excellent approximation to the integral in eq. 1.26. These are called special \mathbf{k} -points. For further details please refer to chapter 3 of the book *Atomic and Electronic Structure of Solids* [23].

1.6 WIEN2k

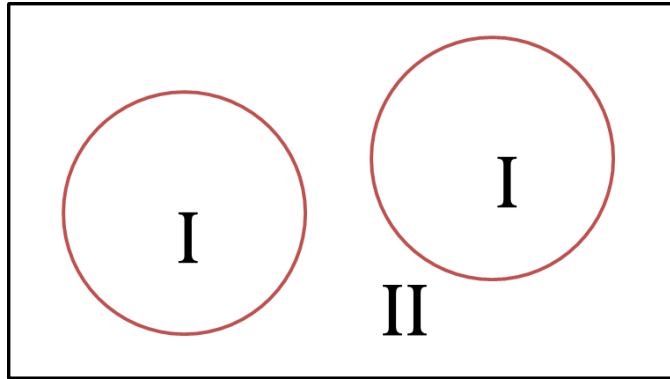


Figure 1.6 – Partition of unit cell into two regions (I) atomic spheres (II) interstitial region.

WIEN2k uses the full-potential linearized augmented plane wave (FP-LAPW) method to define the basis set. The LAPW method is considered to be one of the most accurate methods to solve the Kohn-Sham equations. In this method, the basis functions are constructed by dividing the unit cell into two regions (I) non-overlapping atomic spheres centered on atomic sites, also known as Muffin-tin spheres (MT) and (II) the interstitial region which is the remaining space outside the spheres, as shown in figure 1.6. Atomic spheres are expressed in the form of a linear combination of radial wave

functions multiplied by spherical harmonics, whereas the plane wave expansion is used for the interstitial region. Every plane wave is augmented by a corresponding atomic solution inside every atomic sphere. The equation of the basis functions can be written as:

$$\psi_{\vec{k}_n} = \begin{cases} \frac{1}{\sqrt{\omega}} e^{i\vec{k}_n \cdot \vec{r}}, & \text{when } \vec{r} \in \text{interstitial region} \\ \sum_{lm} [A_{lm, \vec{k}_n} u_l(\vec{r}, E_l) + B_{lm, \vec{k}_n} \dot{u}_l(\vec{r}, E_l)] Y_{lm}(\vec{r}), & \text{when } \vec{r} \in \text{spheres} \end{cases} \quad (1.26)$$

where, $u_l(\vec{r}, E_l)$ is the regular solution of the radial Schrödinger equation for the energy E_l , $\dot{u}_l(\vec{r}, E_l)$ which is the energy derivative of u_l evaluated at the energy E_l . The coefficients A_{lm} and B_{lm} which are functions of \vec{k}_n are determined by matching the basis function in value and slope for each plane wave. Sjöstedt, Nordström and Singh (2000) have shown that this method can be made more efficient by adding functions to linearize the basis set[24]. In pure plane wave codes, the atomic states near the nuclei are represented by pseudo wave functions which make EELS calculation complicated[25, 26]. The WIEN2k basis has the flexibility to describe both atomic-like deep core states around nuclei and free electron-like states in the interstitial region. That's why WIEN2k is known as an 'all electron code'.

The solutions of the Kohn-Sham equations are expanded in this combined basis set of LAPW according to the linear variation method

$$\psi_{\vec{k}_n} = \sum_n c_n \phi_{\vec{k}_n} \quad (1.27)$$

where the coefficients c_n are determined by the Rayleigh-Ritz variational principle. The plane wave cutoff energy parameter is used to define how many plane waves are used in the basis set to describe the valence electrons. All plane waves with energy less than this cutoff are included in the basis set. For, FP-LAPW methods it is specified as the maximum value of $|\vec{K}|$ for a plane wave, defined as \vec{K}_{max} .

Similarly in the two regions the potential is expanded in the following way:

$$V(r) = \begin{cases} \sum_{LM} V_{LM}(\vec{r}) Y_{LM}(\vec{r}), & \text{inside sphere} \\ \sum_{\vec{k}} V_{\vec{k}} e^{i\vec{k}\cdot\vec{r}}, & \text{outside sphere} \end{cases} \quad (1.28)$$

1.6.1 Calculating EELS Spectra

The TELNES[27, 28] module within WIEN2k is used to calculate EELS. This program calculates the DDSCS on a grid of wave vector transfer and energy loss values. Using eq. 1.4, the calculation of cross terms and non-dipole terms, and an integration of the cross-section over wave vector transfers allowed by the collection and convergence angles of the electron microscope can be performed with this module. An additional module “broadening” allows to calculate the final spectra incorporating instrumental and lifetime broadening. The latest version of TELNES 3.0 implemented in the WIEN2k code takes into account relativistic effects due to the high velocity of the electrons in the TEM.

1.6.2 Calculating Bader Charges

The output of the quantum mechanical calculations is the continuous charge density obtained from solving the Schrödinger equation. There have been different schemes proposed to calculate electronic charges on individual atoms. In one of the approach, Henkelman et. al[29] have implemented a fast and robust algorithm based on Bader partitioning scheme [30]. This scheme allows to partition the continuous charge density in different regions and each of these regions is centered on each atom. These regions are known as Bader volumes. The boundary of each Bader volume is defined as the surface through which the charge density gradient has a zero flux. Figure 1.7 shows an example of partitioning of water molecule into three different volumes. The charge enclosed within this volume is a good indication to the total electronic charge belonging to an atom. Bader analysis is implemented within WIEN2k in the module

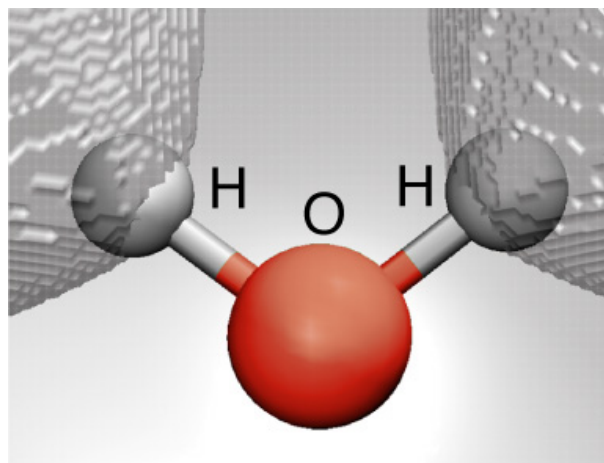


Figure 1.7 – Bader volumes of individual atoms in H₂O. Image courtesy of Henkelman's group[29].

called AIM. Further details on implementation and mathematical description can be found in [30, 31].

1.6.3 Calculating Born Effective Charges

The Born-effective charge Z^* was introduced by Born [32] in 1933. Unlike Bader analysis which calculates the static charge, the Born effective charge is a dynamic concept in the sense that it concerns the response to an atomic displacement. It is directly related to the change of polarization created by atomic displacement which can be measured experimentally. According to the so-called modern theory of polarization, the polarization of a material is not a bulk property and it is ill defined [33, 34]. Instead, only the difference between the two configurations due to external perturbation is a well defined property:

$$\delta P = P^{(1)} - P^{(0)} = \Omega^{-1} \int dt \int_{\text{cell}} dr j(r, t) \quad (1.29)$$

where $j(r,t)$ is the local transient current density resulting from a charge redistribution inside the bulk unit cell. For periodic solids, the Born effective charge of atom ω is a tensor defined as the coefficient of proportionality at the linear order and under the condition of zero macroscopic electric field, between the macroscopic polarization

per unit cell created in direction β and a cooperative displacement of atoms ω in direction α [35]:

$$Z_{\omega,\alpha,\beta}^* = \Omega_0 \left. \frac{\partial P_\beta}{\partial \tau_{\omega,\alpha}} \right|_{\epsilon=0} \quad (1.30)$$

where Ω_0 is the unit cell volume.

The polarization of a given state consists of two components: ionic and electronic

$$P = P_{\text{ion}} + P_{\text{el}} \quad (1.31)$$

The calculation of the ionic contribution is based on the position of atomic nuclei and the corresponding ionic charges. The electronic part is related to the spatial distribution of the electron density, which can be expressed in terms of a geometry phase[36, 37]. Within WIEN2k, the Born-effective charges are computed by using additional software known as Berry-pi[38].

1.7 Real Space Green's Function Formalism (RSGF)

In band structure calculations, Fermi's golden rule is used to calculate the final state Hamiltonian which ignores many body effects and looks as a computational bottleneck to systems which do not have high symmetry. The real space Green's function formalism (RSGF) is based on the quasi-particle theory[39] and addresses these limitations. The RSGF approach is represented by the following equation:

$$G(E) = \frac{1}{E - h' + i\Gamma} = \sum_f |f\rangle \frac{1}{E - E_f + i\Gamma} \langle f| \quad (1.32)$$

where h' is the final state Hamiltonian which includes the screened core hole and Γ is the core hole lifetime and $|f\rangle$ are the quasi-particle eigenstates of h' . The final state Hamiltonian is expressed as

$$h' = \frac{p^2}{2m} + V'_{\text{coul}} + \Sigma(E) \quad (1.33)$$

1.7. Real Space Green's Function Formalism (RSGF)

where V'_{coul} is the Coulomb potential including core hole and $\Sigma(E)$ is the self-energy which is an analog of the exchange-correlation potential V_{xc} of the DFT. However $\Sigma(E)$ is important at higher energies and accounts for losses in the final state. For the near edge spectra, it is equivalent to V_{xc} of DFT. In this equation, the summation over the final states is calculated implicitly reducing the computational effort to calculate it explicitly. This makes the procedure faster as compared to band structure calculations.

1.7.1 FEFF

The name FEFF is derived from f_{eff} , the effective scattering amplitude in the EXAFS equation which was the first application of this code. FEFF is based on the MS theory [40–42] which is a mathematical formalism used to describe the propagation of a wave through a collection of scatterers. Similarly, the outgoing photoelectron can be viewed as a wave that spreads over the solid and then the amplitude of all reflected electron waves are summed at the absorbing atom. The summation is either constructive or destructive to the outgoing photoelectron and it modulates the matrix element between the initial and final state. Further details of implementation of MS theory in FEFF can be found in [43].

FEFF [43, 44] is self-consistent and corresponds to a largely parameter free implementation of the Real Space Multiple Scattering (RSMS) method. It is based on the ab-initio all-electron, real space relativistic Green's function formalism. There are few parameters to be adjusted, like corrections to the Fermi energy, experimental broadening and Debye-Waller (DW) factors. DW factors are used to describe the attenuation of electron scattering caused by thermal motion. These DW factors add extra broadening to the calculated spectra. The scattering process is described using Green's functions. FEFF calculates various spectroscopic properties including x-ray absorption structure (XAS), spin-polarized x-ray absorption, Compton scattering or non-resonant inelastic x-ray spectroscopy (NRIXS). The focus of this dissertation is on ELNES/XANES and I keep my discussion limited to this topic.

1.7.2 XAS and EELS

As discussed in section 1.3, the XAS and EELS are based on similar physics. FEFF was initially designed for calculating XAS and is defined as following in terms of structure factor as follows,

$$\frac{\partial\sigma}{\partial E} = \frac{e^2}{4c\epsilon_0} S(\vec{\epsilon}, E) \quad (1.34)$$

and EELS in FEFF is given by

$$\frac{\partial^2\sigma}{\partial\Omega\partial E} = 4\gamma^2 a_0^{-2} q^{-4} \frac{\vec{k}_f}{\vec{k}_i} S(\vec{q}, E) \quad (1.35)$$

Initially, XAS was used without modification to calculate EELS by multiplying the XAS by a factor f , given by,

$$f = \frac{4\gamma^2}{a_0^2} \frac{\vec{k}_f}{\vec{k}_i} \frac{4c\epsilon_0}{e^2} \vec{q}^{-p} E^{-1} \quad (1.36)$$

where $p=2$ for dipole terms and 0 for quadrupole terms. Later on, the relativistic corrections were incorporated in FEFF to calculate orientation resolved EELS [45].

1.7.3 General Approximation Used by the FEFF Code

Firstly, FEFF uses the muffin tin approximation to calculate the atomic potentials. Within this scheme, the potential is assumed to be spherical in the defined muffin tin spheres for each atom and it becomes constant outside the sphere. This makes it easier to implement theoretical and numerical problems of multiple scattering. The self-energy is calculated and included with the scattering potentials. Ideally, the self-energy can be calculated using the GW approximation [46], but this procedure is computationally demanding. In turn, local density approximations are commonly used for the self-energy. Within FEFF there are two choices to include the self-energy: 1) The Hedin Lundqvist self-energy based on the plasmon-pole model for an electron gas[47] is used for solids whereas 2) The Dirac-Hara self energy[48] based on static

1.7. Real Space Green's Function Formalism (RSGF)

exchange is used for small molecular systems.

Secondly, FEFF approximates the transformation of the N -electron many body problem into a simpler single particle problem. FEFF creates a cluster of atoms of finite size in real space. The self-consistent potentials are calculated by converging the calculations with respect to the cluster size. At the same time, the Fermi level, charge transfer, the DOS and the electron density are also calculated self-consistently. Typically, for EELS calculations, one should consider a cluster of atoms in the range of 100-150 atoms. However, in some cases bigger cluster sizes are required. One should increase this size in order to check the convergence of the calculated spectra. The self-consistent field (SCF) potentials are important to calculate accurate near edge EELS structures.

1.7.4 Final State Rule and RPA

For systems with more than one inequivalent atoms, the sum of the spectra from each of them has to be calculated with an appropriate weight. It is common to calculate EELS in the presence of a core hole because of the effects of the self-energy on the spectra. By default, FEFF calculates the spectrum in the presence of a core hole. FEFF does not use periodic boundary conditions and therefore only one core hole is used in the calculation unlike the supercell size issues of band structure codes[49]. However, it is also possible to calculate EELS spectra without core-hole. For insulators, a core hole is essential whereas for metals the core hole effect is supposed to be completely screened out. Core hole calculations can be implemented using the final state rule or the linear response random phase approximation (RPA) screening. It was found that the screened hole in FEFF calculated with RPA can be comparable to the Bethe-Salpeter equation approach[50].

For the final state rule, different SCF calculations are performed for both initial and final states to incorporate them in the Hamiltonian using Fermi's golden rule. In addition, spectral broadening is added in form of the lifetime of the core state, the lifetime of final state and instrumental broadening. In principle, all excited states have a finite lifetime. The shorter the lifetime of the involved states, the broader the

spectral lines. The lifetime broadening factors are contained in the imaginary part of the FEFF calculated self-energy. Instrumental broadening can be set by the user, based on the instrument used to record the EELS spectra. There are other parameters like orientational dependence which can be kept similar to the experimental parameters.

1.8 Comparison of WIEN2k and FEFF

Table 1.1 – Comparison between WIEN2k and FEFF

No.	WIEN2k	FEFF
1)	works in reciprocal Space	both real and reciprocal space
2)	periodic systems	aperiodic, periodic and molecules
3)	accurate Near edge structure	accurate Extended Structure
4)	band structure calculations	multiple scattering calculations
5)	precise for <i>K</i> -edges	precise also for <i>L</i> -edges
6)	full-potential - slow	finite cluster size - Fast
7)	also used for structural optimization	Used only to calculate spectra

Each of the two methods have their specific advantages. WIEN2k works by solving the Schrödinger equation in reciprocal space using DFT and is limited to periodic systems. Systems with defects require larger supercell sizes making it computationally very expensive for WIEN2k. On the other hand, FEFF describes finite systems by calculating the Green's function in real space using MS theory. This makes FEFF fast and applicable to non-periodic systems. FEFF also includes self-energy, Debye-Waller factors for thermal effects, and other useful features that make it particularly well suited for large energy regions above the edge threshold. But, FEFF uses spherical muffin tin potentials, and it can lead to finite cluster effects when describing solids. On the other hand, WIEN2k considers full-potential and describes the electronic structure accurately and can also be used for structural optimization. But, WIEN2k only involves the near edge region.

1.9 Defects in Solids

A saying by Colin Humphrey reads: “Crystals are like people: it is the defects in them which tend to make them interesting”. Defects indeed have a profound impact on materials properties. In several cases, defects are deliberately incorporated in materials to improve their efficiency. For example, defects are responsible for the color and the price of diamonds. Also, introducing defects by forging a metal increases its strength. In general, there are three basic classes of defects divided based on their dimension:

1. Point defects: This class includes lattice-vacancies, self-interstitials and substitutional impurity atoms, Frenkel pairs, interstitials, anti-site defects etc.
2. Linear defects: This class mainly consists of dislocations. It includes edge, screw, mixed and partial dislocations.
3. Planar defects: This class is majorily formed by twin boundaries, stacking faults, interfaces, surfaces.

From here on, I will discuss some of these defects in detail which are in the interest of this thesis.

1.10 Point Defects: Vacancies

Vacancy sites are characterized by missing of an atom at a crystallographic position. Vast amounts of theoretical and experimental work have been published on different kinds of vacancies in the ABO_3 type perovskite. In this chapter, I will particularly focus on oxygen vacancies (v_o). To control such defects, it is necessary to determine their location, distribution, clustering or segregation and understand how they affect the local structure and functional properties. The quantitative determination of the spatial distribution of oxygen-ion vacancies is limited by the difficulty in directly observing oxygen atoms. There are indirect spectroscopic methods like EELS which can

Chapter 1. Techniques and Methods

estimate the concentration of v_{O} by recording the fine structure of the reduced cation surrounded by vacancy sites. The role of first-principle EELS simulations becomes crucial here in determining the 3D position of oxygen vacancies and further establishing the relation between structural aspects of oxygen vacancies and properties of the material. This kind of calculations not only confirm the experimental findings but also helps in obtaining important quantities like formation energies and the characteristics of the wave-function of the defect state.

The task of simulating the effect of oxygen vacancies becomes easier if there is beforehand information available about the crystal structure and the v_{O} concentration. In many cases, oxygen atoms are occupying inequivalent sites in a crystal structure and they can have different v_{O} formation energy. The site with lower v_{O} formation energy will be preferred over others. Such issues can also be resolved by calculating the v_{O} formation energy for each inequivalent site in the crystal structure. This would help in building the correct structure with the appropriate v_{O} concentration. For example, Zhang et al. [51] show the significance of v_{O} in a perovskite-type material barium-strontium-cobalt-ferrite by calculating different v_{O} concentrations in its bulk structure. Figure 1.8 shows the number of different oxygen atoms present in this material, denoted by different numbers. For all these possible defects the v_{O} formation energy was calculated. In another study by Morgan et al.[52], the v_{O} formation energy was calculated for different surfaces of rutile TiO_2 . The variation of the v_{O} suggested differences between the surfaces with respect to their catalytic behavior. The size of the supercell is vital in order to perform v_{O} formation energy calculations. The size of the supercell should be large enough to avoid artificial interactions between defect and its neighboring periodic image. The origin of such artificial interactions lies in overlapping of wave functions and, in case of charged defects, the unphysical electrostatic interaction of the defect with its periodic images. The effect of such interactions can be reduced by increasing the lattice constant L , but the defect energy decays asymptotically in the form of $\frac{q^2}{L}$, where q is the defect charge. Significant efforts have been taken to design several correction schemes to avoid such errors[53–55]. The

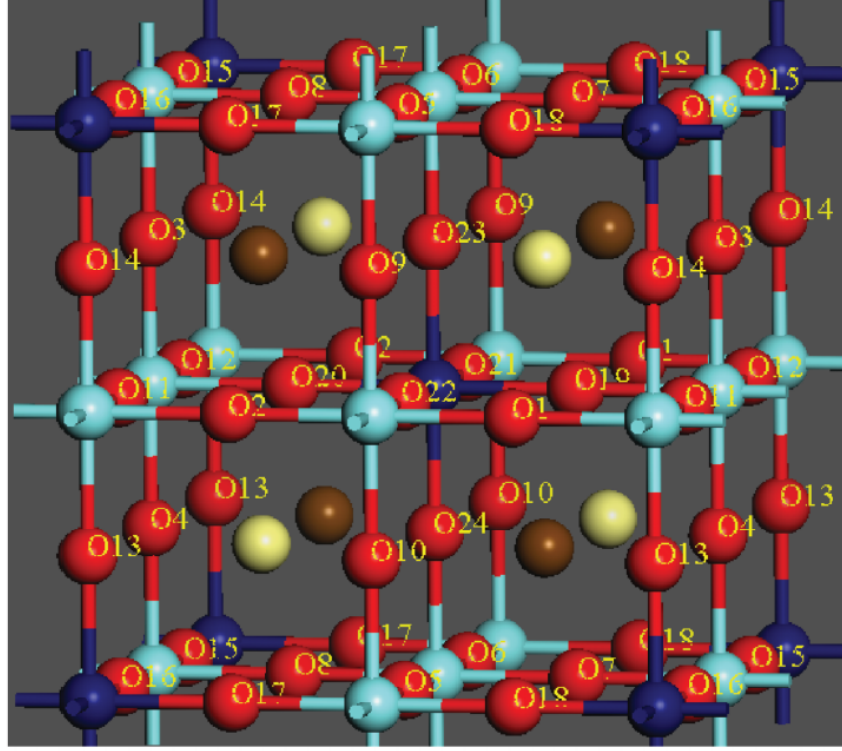


Figure 1.8 – Model structure of $\text{Ba}_{0.5}\text{Sr}_{0.5}\text{Co}_{0.75}\text{Fe}_{0.25}\text{O}_3$ (BSCF). The light and dark brown circles represent Sr and Ba respectively, the light and dark blue circles represent Co and Fe respectively, and the labelled red circles are O ions. This figure is directly adapted from ref[51].

formation energy of the defect X in charge state q is defined as [56, 57],

$$E^f[X^q] = E_{\text{tot}}[X^q] - E_{\text{tot}}[\text{bulk}] - \sum_i n_i \mu_i + qE_{\text{F}} + E_{\text{corr}} \quad (1.37)$$

where $E_{\text{tot}}[X^q]$ is the total energy of the supercell containing defect X , $E_{\text{tot}}[\text{bulk}]$ is the total energy of the bulk supercell and n_i is the number of atoms of type i removed from the supercell. The chemical potential of the corresponding species used for vacancy is μ_i , E_{F} is the Fermi energy and E_{corr} is the correction term that accounts for the errors due to finite k-point sampling, and electrostatic and elastic interactions between the periodic images of defects.

The flexibility of accommodating v_0 is more pronounced in perovskites containing transition-metals because of their ability to adopt a variety of valence states. Hence,

Chapter 1. Techniques and Methods

they can accommodate the associated change in the formal charge. Very fine changes in the concentration of v_o can lead to dramatic changes in the functional properties of the material. Epitaxial strain has been widely used for thin films to play with functional properties of a material by controlling the amount of oxygen vacancies. Given the relevance of the v_o in the functional properties, there have been numerous studies using first-principle calculations to correlate the effect of strain on the v_o formation energy. For e.g., Aschauer et al. [58] showed that the tensile strain lowers the v_o formation energy in CaMnO_3 . The v_o formation energy was computed from:

$$\Delta E_{\text{form}}(\epsilon, \mu_{\text{O}}) = E_{\text{tot},V_o} - E_{\text{tot},\text{stoi}} + \mu_{\text{O}} \quad (1.38)$$

where ϵ and μ_{O} are the strain and the oxygen chemical potential respectively. $E_{\text{tot},\text{stoi}}$ and E_{tot,V_o} are the total DFT energy of the stoichiometric cell and that containing one oxygen vacancy respectively. Figure 1.9(a) shows the crystal structure of unstrained CaMnO_3 and figure 1.9(b) shows the calculated formation energy of two inequivalent oxygen atoms as a function of applied strain. In chapter 2 of this thesis, I present

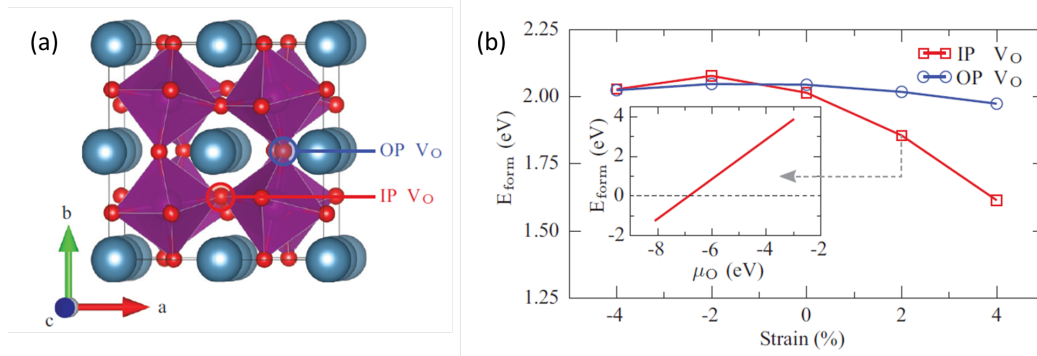


Figure 1.9 – (a) The crystal structure of bulk, unstrained CaMnO_3 . The two inequivalent v_o positions, which are adjacent to Mn ions in the strained ac plane (IP) and perpendicular to it (OP) are indicated. Color code: Ca: blue; Mn: purple; O: red. The v_o formation energies for the two in-equivalent v_o positions in the $Pnma$ tilted CaMnO_3 structure at an oxygen chemical potential of 5 eV, corresponding to typical growth conditions under air. The inset shows the formation energy of the IP v_o at 2% tensile strain as a function of the oxygen chemical potential. This figure is directly adapted from ref[58].

a similar study on different strained-films of SrMnO_3 . The electronic structure of

SrMnO₃ corresponding to differently strained films were investigated using HAADF-STEM, EELS and DFT simulations to understand the effect of strain on v_o and on the features of the corresponding O-K edge EELS spectra.

There are numerous examples present in literature where systems with oxygen vacancies are exploited using both experimental techniques and computational methods. Cheng et al.[59] reported the effect of v_o on the electronic and crystal structure in the

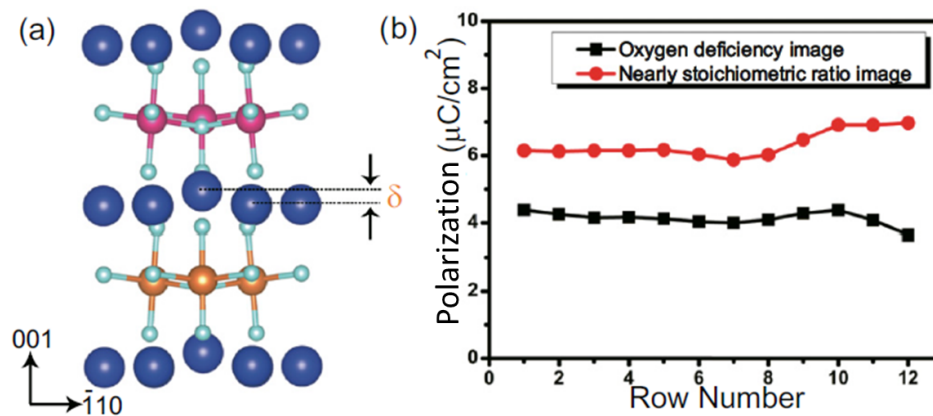


Figure 1.10 – (a) YMnO₃ hexagonal crystal model from [110] zone axis with displacement defined by δ . (b) Calculated polarization values from HRTEM images. This figure is directly adapted from ref[59].

multiferroic material YMnO₃ using a combined study of TEM/EELS and DFT calculations. Figure 1.10(a) shows the hexagonal crystal structure of YMnO₃ and figure 1.10(b) shows the calculated polarization with and without v_o . This study also explains that the incorporation of v_o in this structure reduces the amount of displacement induced polarization of the material. It also shows how the Mn ion positions are altered due to vacancies and their role in impairing the ferroelectricity of the material.

The above mentioned examples reflect the importance of studying the consequences of v_o on potential applications of known materials. These examples also reflect the role of first-principle simulations to further investigate in depth information of the v_o and their correlation with the crystalline structure, electronic structure and the material's functionality. Similarly, in this thesis, I present two different systems in chapter 2 where the study of v_o were studied experimentally and theoretically.

1.11 Line Defect: Edge Dislocation

Dislocations are central to the understanding of the mechanical behavior and growth of crystalline materials. With the interest of this thesis, I keep my discussion limited

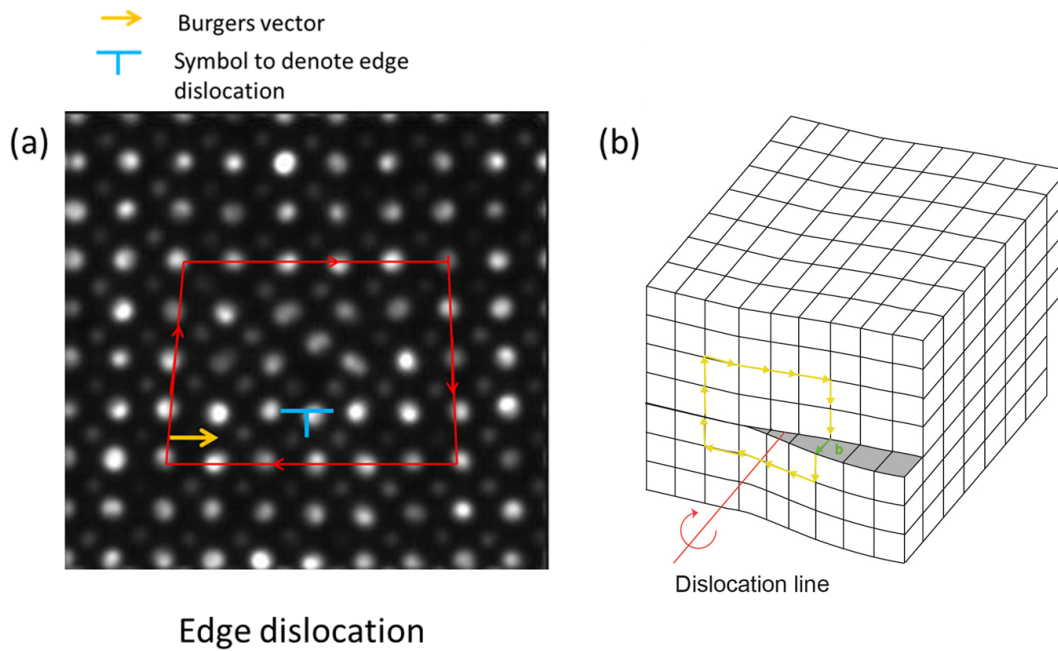


Figure 1.11 – (a) HAADF-STEM simulated image of an edge dislocation in BiFeO_3 with Burgers vector (yellow) and symbol (blue) to specify the edge dislocation. (b) Model of screw dislocation [60].

to edge dislocations. An edge dislocation (figure 1.11(a)) can be visualized where an extra half-plane of atoms is introduced mid way through the crystal, distorting and stressing surrounding planes. The line running along the bottom of the extra half plane is called as “dislocation line”. When an external force is applied from one side of the crystal structure, this extra plane glides through plane of atoms breaking and joining the bonds. Conversely, in a screw dislocation (figure 1.11(b)), one can imagine cutting the sample along a plane and slipping one half across the other plane by a lattice vector. The magnitude and direction of the distortion to the lattice are represented by Burgers vector. For edge dislocations, Burgers vector is perpendicular to the dislocation line whereas for screw dislocation they are parallel. Figure

1.11(a) shows the simulated edge dislocation model in BiFeO_3 with Burgers vector and symbol “T” which is used to represent an edge dislocation. The dislocation core

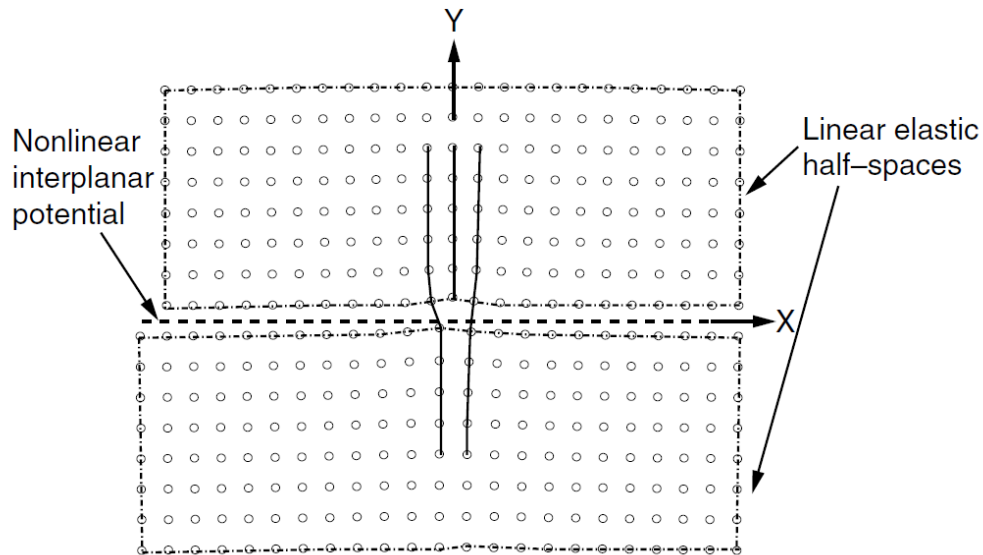


Figure 1.12 – A schematic description of edge dislocation in crystal structure divided into linear and non-linear atomistic region. Figure is directly adapted from ref[61].

structure and its physical properties control the mobility of a dislocation and are responsible for the interaction with the neighboring dislocations. All these factors are relevant for the study of plastic deformation. That’s why there has been a great deal of interest in describing the dislocation core structure on the atomic scale and in further investigating their properties. There are two types of theoretical approaches to study dislocation core properties. The first approach is based on atomistic simulations using empirical interatomic potentials or ab-initio calculations. Though, ab-initio calculations are considerably more accurate, they are computationally expensive to investigate dislocation core properties. The Peierls-Nabarro (P-N) theory is another approach, other than atomistic simulations to study dislocation core properties. P-N models bridges both continuum theory and atomistic theory to provide quantitative estimations of atomistic properties of the dislocations. As shown in figure 1.12, it is described by dividing the solid region into two halves joined by atomic-level forces across their common interface, known as the slip plane. The P-N model assumes that the misfit region of inelastic displacement is restricted to that slip plane, whereas

Chapter 1. Techniques and Methods

linear elasticity applies far from it. The continuous distribution of shear along the slip plane is represented by $S(x)$ (x is the coordinate along the displacement direction of the dislocation in the slip plane). The stress generated by shear displacement $S(x)$ can be represented by a continuous distribution of infinitesimal dislocations with density $\rho(x)$

$$\rho(x) = \frac{dS(x)}{dx} \quad (1.39)$$

The restoring force, F , acting between atoms on either side of the interface is balanced by the resultant stress of the distribution leading to the well-known Peierls–Nabarro (P-N) equation:

$$F(S(x)) = \frac{K}{2\pi} \int_{+\infty}^{-\infty} \frac{1}{x-x'} \left[\frac{dS(x')}{dx'} \right] dx' = \frac{K}{2\pi} \int_{+\infty}^{-\infty} \frac{\rho(x')}{x-x'} dx' \quad (1.40)$$

where K , the energy coefficient, is a function of the dislocation character. Vitek et al.[62] suggested that the solution of the P-N equation can be numerically found by introducing a restoring force simply defined as the gradient of generalized stacking fault (GSF) energy γ ,

$$F(S) = -\frac{\partial\gamma}{\partial S} \quad (1.41)$$

First-principles calculations are used to calculate the GSF energies along the Burgers vector direction for several slip systems to find out the potential slip systems in the material. The favorable slip system depend intimately on the structure and bonding of the material. The GSF energies for the potential slip systems are then used as an input for the PN model. In the original model, the P-N equation was solved by introducing a sinusoidal restoring force yielding a well known analytical solution. However, Joos et al.[63] pointed out that, in a real crystal, the restoring force could be quite different from sinusoidal. The $S(x)$ was further obtained by searching for a solution in the form:

$$S(x) = \frac{b}{2} + \frac{b}{\pi} \sum_{i=1}^N \alpha_i \arctan \frac{x-x_i}{c_i} \quad (1.42)$$

1.11. Line Defect: Edge Dislocation

where α_i, x_i and c_i are variational constants. The magnitude of the Burgers vector is b . The aim of this P-N model is to find slip distribution $S(x)$ across the slip plane which minimizes the total energy of the system. The energy comes from two distinct contribution: the energy penalty for misfit across the glide plane and second the elastic energy stored in two elastic half-spaces. The edge dislocation produces planar strain defined by $u_z = 0$. The displacements along x and y can be derived by integrating the strain in each direction. The final equations to determine the coordinates of atoms are given by,

$$u_x = \frac{b}{2\pi} \left[\tan^{-1} \frac{y}{x} + \frac{xy}{2(1-\nu)(x^2 + y^2)} \right] \quad (1.43)$$

$$u_y = -\frac{b}{2\pi} \left[\frac{1-2\nu}{4(1-\nu)} \ln(x^2 + y^2) + \frac{x^2 - y^2}{4(1-\nu)(x^2 + y^2)} \right] \quad (1.44)$$

Using these equations, one can find out the elastic displacements of the atom around a dislocation core. The elastic energy of an edge dislocation can be obtained by integrating the deformation energy over the whole volume of the deformed crystal. The elastic energy per unit length is given by:

$$U = \frac{Gb^2}{4\pi(1-\nu)} \ln \frac{r_1}{r_0} \quad (1.45)$$

where G is the shear modulus, ν is Poisson's ratio and r_1 is the cut-off radius for outer boundary of the elastic field. The elastic energy depends logarithmically on r_1 . A good value r_1 is around $10 \mu\text{m} - 10 \text{nm}$. The elastic energy also depends on r_0 , which is the radius of the core. Energy in the core of the dislocations is given by

$$E_{\text{core}} = \frac{Gb^2}{2\pi} \quad (1.46)$$

And the total energy of dislocation is given by:

$$E_{\text{tot}} \approx Gb^2 \quad (1.47)$$

Chapter 1. Techniques and Methods

There are numerous studies which have used the P-N theory to model the dislocation structure in a crystal. For example, Ferré et al.[64] analyzed the dislocation core structures in SrTiO₃ using the P-N model coupled with first-principle calculations of GSF.

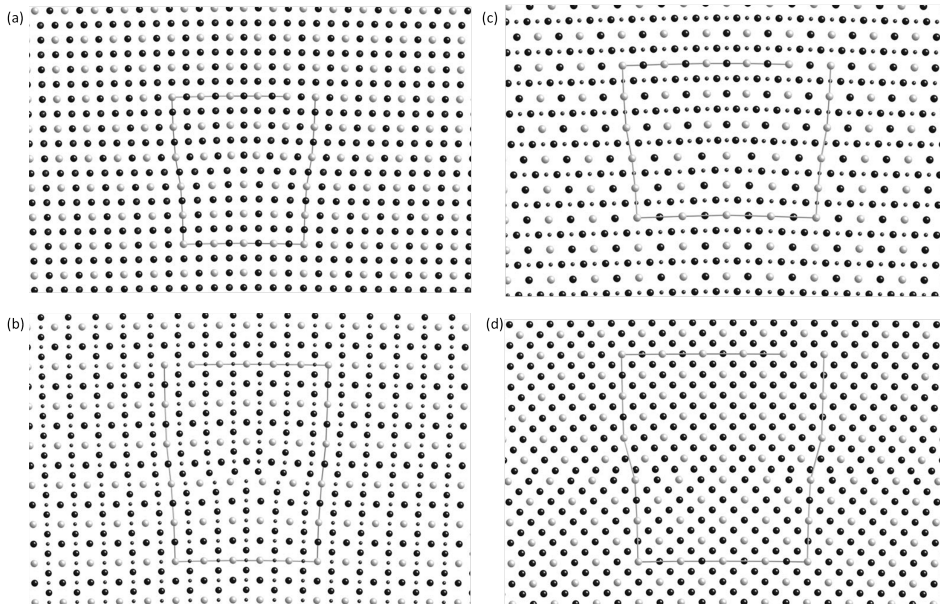


Figure 1.13 – Atomistic models for edge dislocations in the SrTiO₃ perovskite calculated for the following slip systems: (a) $\langle 100 \rangle \{010\}$, (b) $\langle 100 \rangle \{011\}$, (c) $\langle 110 \rangle \{001\}$, and (d) $\langle 110 \rangle \{1\}$. For the four structures, light gray spheres correspond to Sr, small black spheres to Ti, and large black spheres to O. Figure is directly adapted from ref[64].

Figure 1.13 shows the final shape of the lattice planes obtained for four different slip planes. Further validation was done by comparing the configuration obtained from the P-N model with experimental HRTEM images. In another work, Sydow et al. [66] presented a detailed study of Shockley partial dislocations using GSF surface energies calculated by first-principles as an input for the P-N model. Besides the P-N model, there are other studies reported in the literature using ab-initio methods to model edge dislocation cores as discussed below.

From an experimental point of view, the TEM/STEM techniques are used to image dislocations and high-resolution imaging can be further used to reveal the dislocation core structure. Especially, the STEM mode is helpful by acquiring different images and spectroscopy signals to examine the internal structure and composition of the dislocation core. This kind of investigation is helpful for building a theoretical model

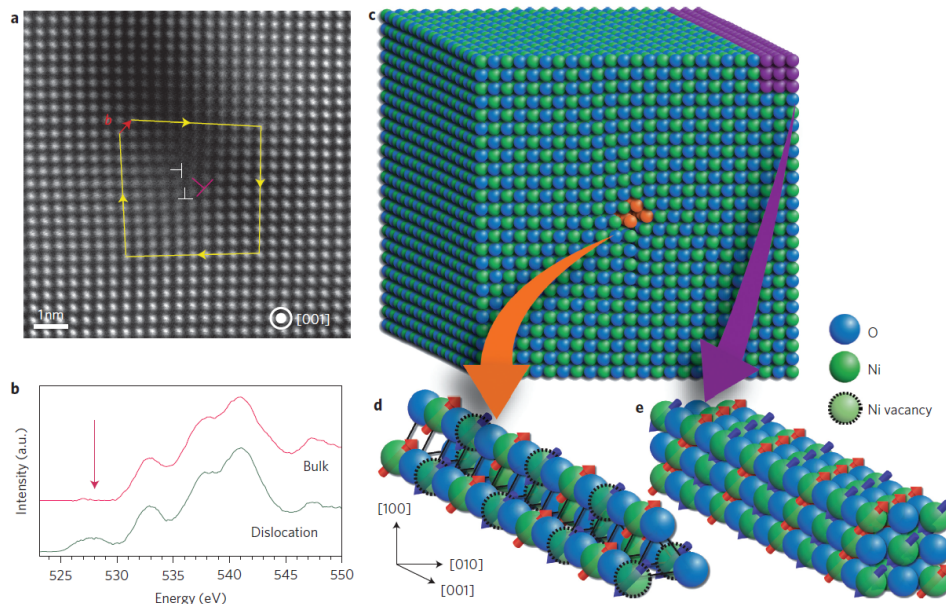


Figure 1.14 – a) Typical ADF-STEM image of a dislocation core in the NiO thin film. The dislocation core is indicated by the label in red. b) O *K*-edge EEL spectra measured at the dislocation core and in the bulk region. A peak appears around 526 eV (indicated by the arrow) in the spectrum of the dislocation cores; this is absent in the bulk spectrum. c,d,e) Atomistic model of the dislocation cores in NiO. Figure is directly adapted from ref[65].

for atomistic simulations. For example, in a recent study, Sugiyama et al. [65] characterized the edge dislocation structures in NiO thin films using annular dark-field STEM and EELS. Figure 1.14(a) and (b) show the HAADF-STEM image of the edge dislocation and the O-*K* edge EEL spectra recorded from the dislocation core and the bulk. Features in the O-*K* edge EEL spectra at the dislocation core and away from the core were helpful in modeling the dislocation core using DFT simulations. Simulations confirmed that the changes in the O-*K* edge EEL spectrum were due to the presence of Ni vacancies in the dislocation core. Figure 1.14(c-e) show the atomistic model of the dislocation core structure. It was shown by this study that dislocations can be the unique sources of magnetic properties and could be used for future magnetic and electronic devices.

The above mentioned examples show the importance of characterizing such defects and determine their local structure to get valuable insights to understand their impact on the functional properties of bulk materials. Apart from static dislocations, it is

also very interesting to study dynamics of dislocations. Ishida et al.[67] discovers the role of dislocation movement in electric nanocontacts. From the thesis point of view, I only deal with static dislocations and limit my discussion here to modeling of such dislocations. Particularly, in chapter 3 of this thesis, I discuss an example of modeling an edge dislocation core structure in BiFeO₃ using both P-N theory and ab-initio simulations.

1.12 Planar Defects

This category of defects mainly consists of stacking faults, grain boundaries, interfaces, twin boundaries, surfaces etc. However, with the interest of this thesis, I will keep my discussion limited only to stacking faults. Generally, a stacking fault is a local deviation from one of the stacking sequences to the other one. For example, a perfect FCC crystal with stacking sequence along $\langle 111 \rangle$ direction isABCABCABC....., the intrinsic stacking fault is equivalent to removal of one layer (.....ABCACABC.....) whereas extrinsic stacking fault (.....ABCABACABC.....) is equivalent to insertion of a layer. Generally, stacking faults are formed during crystal growth or because they evolve from other defects or due to plastic deformation. The edge of the stacking fault or the junction of two different faults is known as partial dislocation. A perfect dislocation might dissociate into two partial dislocations as it lowers the total energy. For example, Burgers vector of perfect dislocation $b=a/2[110]$, may decompose into two partials $a/6[121]$ and $a/6[2,1,-1]$. The energy of the perfect dislocation is given by:

$$E_{\text{tot}} = Gb^2 = G(a/2 \langle 110 \rangle)^2 = \frac{Ga^2}{2} \quad (1.48)$$

whereas, energy of two partial dislocations is given by:

$$E_{\text{tot}} = 2Gb^2 = 2G(a/6 \langle 121 \rangle)^2 = \frac{Ga^2}{3} \quad (1.49)$$

A stacking fault perturbs the electronic energy levels of the bulk material which are more pronounced around the Fermi level. These perturbations deserve special

attention because they may affect the electronic properties of a material, especially in the case of semiconductors. From past few decades, structural and electronic characterization of such defects have been investigated in numerous studies using both experimental techniques and theoretical methods. For example, Camarda et al.[68] presented a new class of a bar-shaped stacking fault in SiC identified using microphotoluminescence measurements and HRTEM. A peak at 2.9 eV was observed in photoluminescence measurements, which is 0.3 eV below the conduction band. This was further validated by calculations of the Kohn-Sham electronic band structure and the defect formation energy. In another work, Han et al.[69] presented a computational model for low-energy extended defects in bulk zeolitic imidazolate frameworks. They demonstrated the thermodynamic stability of such defects and examined their impact on pore diffusion and surface accessible area. It was found that there was no significant change in the diameter of the pores but the stacking fault results in a larger cavity, which may imply a lower diffusion rate. This kind of studies shows the importance of computational methods to get insights into the structural and physical properties of stacking faults in materials. Similarly, Li et al.[70] presented a combined study of aberration corrected STEM and DFT calculations to determine the atomic configurations of dislocation pairs in a II-IV semiconductor compound cadmium-telluride (CdTe). Figure 1.15 (a),(b) shows high-resolution STEM images of intrinsic and extrinsic stacking faults with Cd and Te as unpaired atomic columns at a pair of partial dislocations. With the help of DFT calculations it was shown that such stacking faults do not introduce gap states but cause a significant band bending due to charge transfer between the Te- and Cd- dislocation core. A similar example of a stacking fault in III-V semiconductor compound gallium-arsenide (GaAs) is studied experimentally and theoretically in chapter 4 of this thesis.

Theoretically, it requires a lot of effort to model this kind of defects because of the requirement of large supercells. The size of the supercell is crucial to avoid spurious interactions between defects and their neighboring periodic images. In general, 5-10 atomic layers are sufficient to avoid these unwanted interactions. As a result, it leaves a supercell with too many atoms to simulate for DFT simulation. This is the reason why in many cases classical potentials are very important to simulate this kind of

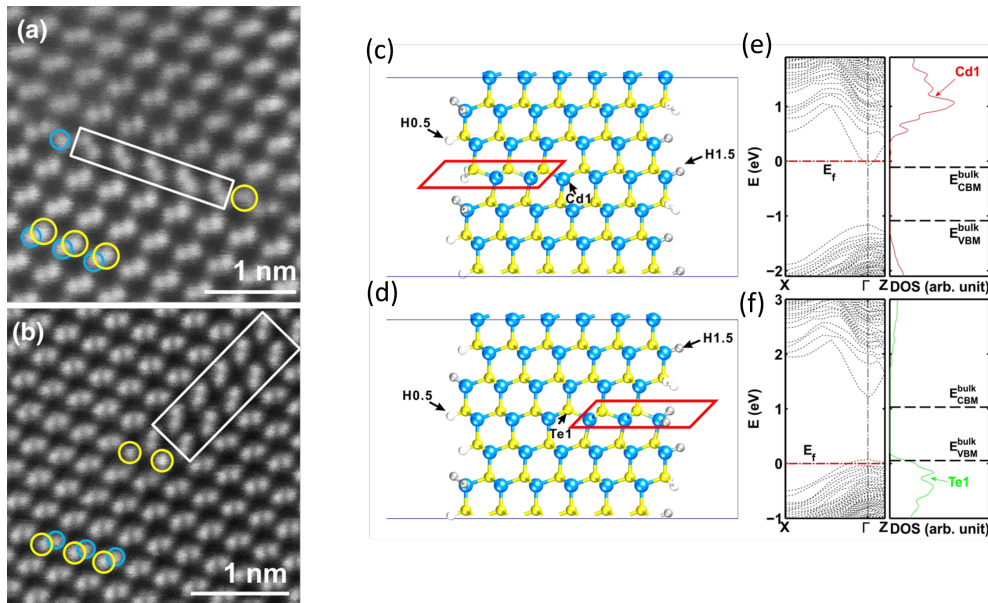


Figure 1.15 – a) A large number of dislocations are generated by high-temperature deformation. b) Metallic Ti film is deposited on the sapphire plate containing straight dislocations. c) an individual Cd core and (d) an individual Te core of an intrinsic stacking fault. The red boxes indicate the intrinsic stacking fault. Band structure and DOS of individual cores: (e) Cd core; (f) Te core. Figure is directly adapted from ref[70].

defects. This also evokes the design of new empirical and semi-empirical potentials to deal with such large systems to investigate their structural configuration and get insights into their physical properties. Liu et al. has designed bond-valence vector summation (BVVS) potential for BiFeO_3 [71] and PbTiO_3 [72] to study the domain wall energies and dynamics for ferroelectric-to-paraelectric transitioned phases. This potential is based on the bond-valence conservation principle. I discuss one example in chapter 3 of this thesis where I used BVVS potential to study the dislocation core structure in BiFeO_3 .

2 Point Defects in Complex Oxides

In this dissertation, the main focus will be on oxygen vacancy and substitutional point defects. I discuss three sub-chapters in this section:

- 1) Surface reduction in BiVO_4
- 2) Effect of strain in SrMnO_3
- 3) Effect of Nickel substitution in LaFeO_3

2.1 Surface Reduction in Bismuth Vanadate - BiVO_4

The following part in the section has been extracted with some modifications from the article titled as "Direct Evidence of Surface Reduction in Monoclinic BiVO_4 " [73] published by myself together with Marta Rossell, Andreas Borgschulte, Cécile Hébert, Daniele Passerone and Rolf Erni. The experimental measurements were performed by Marta Rossell, theoretical simulations and interpretation with experiments were done by myself, the XPS measurements were done by Andreas Borgschulte (not discussed in the thesis), and Cécile Hébert, Daniele Passerone and Rolf Erni guided me through this work. I would like to thank all of them for their great effort and contribution.

2.1.1 Introduction

From the last two decades, BiVO_4 (BVO) is known to be a promising candidate for photoelectrochemical water splitting and wastewater treatment [74–77]. The main advantage of BVO over TiO_2 is its ability to use visible light rather than ultraviolet light irradiation to split water and to break down organic pollutants in sewage water. Additionally, the abundance and nontoxicity of its constituent elements make BVO a low-cost and environmentally friendly photocatalyst.

BVO is known to exist in three natural crystalline polymorphs: orthorhombic pucherite[78, 79], tetragonal dreyerite[80], and monoclinic clinobisvanite[80]. However, BVO synthesized in the laboratory normally does not adopt the pucherite structure. Among the three phases, the monoclinic clinobisvanite BVO (m-BVO) phase exhibits a much higher photocatalytical activity due to its favorable band gap (2.4–2.5 eV) in the visible region of the electromagnetic spectrum, and a valence band position suitable for driving water oxidation under illumination[74, 81, 82]. The conduction band, however, is reported to be positioned too low relative to the proton reduction potential for hydrogen evolution [83]. Nonetheless, the overall water splitting reaction can be accomplished by using a separate hydrogen evolution catalyst in tandem, commonly a noble- or transition-metal catalyst [77, 84, 85]. Due to its poor charge carrier ability BVO shows very low photoconversion efficiency for practical applications. Several doping strategies have been examined to enhance its efficiency[84, 86]. Some of these doping improve the transport while others alter the formation of defects [87].

Formation of defects in form of oxygen vacancies, the intrinsic defects in m-BVO, have been recognized to play a key role in the performance of BiVO_4 . According to Kho et al.[76], v_{O} act as harmful photogenerated carrier traps. However, according to Wang et al.[88] the excess of v_{O} increases the donor densities and hence enhances the charge transport in bismuth vanadate. These contradictory opinions highlight the importance of gaining a deeper understanding of the concentration and spatial distribution of v_{O} and its effect on charge transport. In this section of the chapter, I will present the structural properties and the electronic behavior of BVO using a combination of scanning transmission electron microscopy (STEM), and electron

2.1. Surface Reduction in Bismuth Vanadate - BiVO₄

energy-loss spectroscopy (EELS). To characterize the BVO, reference EELS spectra of different Vanadium oxidation were obtained from bulk V₂O₃, VO₂, and V₂O₅ samples.

2.1.2 Experimental Section

The m-BVO samples was purchased from Alfa Aesar. The vanadium reference sample (V₂O₃, VO₂, and V₂O₅) were supplied by Sigma-Aldrich. X-ray diffraction patterns were obtained using Stoe P powder X-ray diffractometer in transmission mode (Cu K_{α1} radiation, Ge-monochromator, Dectris Mythen silicon strip detector).

Samples for transmission electron microscopy were prepared by dispersing the m-BVO powder in ethanol and dropping the dispersion onto a lacey carbon coated copper grid, followed by a very gentle oxidizing plasma treatment to remove hydrocarbon contamination. In order to preserve the surface properties of the m-BVO particles, a very short plasma exposure (10 s) was applied using a Fischione shielded holder port which reduces the plasma density by reducing the cross sectional area available to the plasma near the holder tip.

The m-BVO particles were studied by high-angle annular dark field (HAADF) STEM using JEOL JEM-ARM200F microscope operated at 200 kV. A probe semiconvergence angle of 25.3 mrad was set yielding a calculated probe size of about 78 pm. The annular semidetection range of the annular dark-field detector was calibrated at 68–280 mrad. Other details regarding experimental measurements are describe in detail in Rossell et al. [73].

2.1.3 Experimental Results

Figure 2.1(a) shows the XRD pattern of the commercially ordered BiVO₄ powder with the monoclinic clinobisvanite (m-BVO) structure. The XRD pattern collected at room temperature proves that the sample consists entirely of the monoclinic phase (JCPDS file no. 14-0688) with no traces of other phases. The obvious splitting of the (101) and (0 $\bar{1}$ 1) peaks around 18.5° and of the (200) and (0 $\bar{2}$ 0) peaks around 35° provides evidence for distinguishing the monoclinic from the tetragonal phase.

Chapter 2. Point Defects in Complex Oxides

Figure 2.1(b) shows the model of monoclinic BVO along the [100] crystallographic direction and it consists of rows of isolated VO_4 tetrahedra separated by Bi atoms coordinated with eight O atoms to form BiO_8 dodecahedra. Both Bi^{3+} and V^{5+} cations are displaced from the centrosymmetric sites along the same c direction, with the direction of the displacement alternating up and down along the c-axis. This results in a layered-like structure of VO_4 and BiO_8 groups separated in nonequidistant planes. The m-BVO particles have a random morphology with sizes between a few nanome-

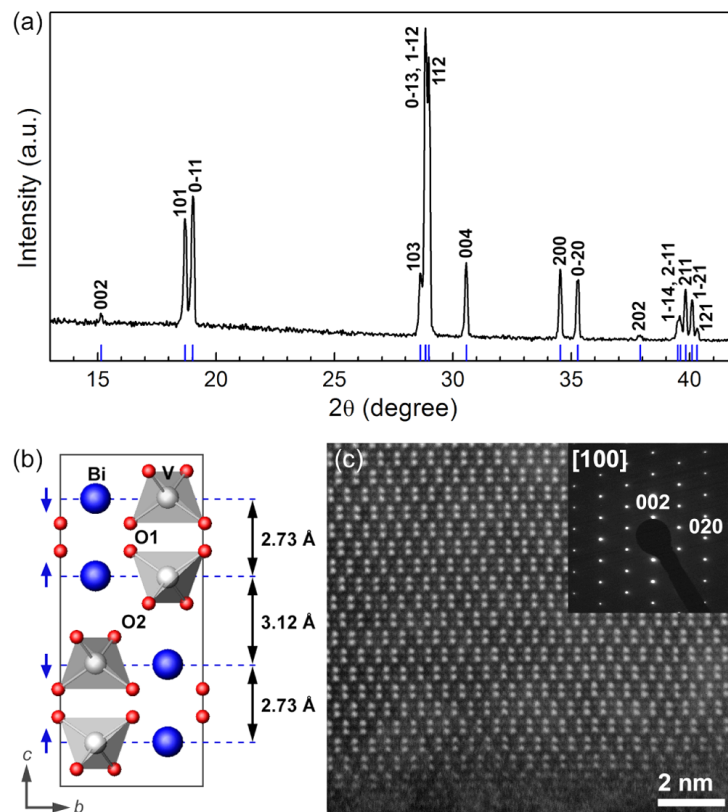


Figure 2.1 – (a) XRD pattern of the sample showing the characteristic split of the monoclinic clinobisvanite phase. (b) Rendering of the m-BVO structure along [100] with (blue) Bi, (gray) V, and (red) O columns. The V is at the center of a distorted tetrahedron. The blue arrows show the displacement of the Bi^{3+} and V^{5+} cations from the centrosymmetric positions. (c) Atomic resolution HAADF-STEM image of the m-BVO crystal structure imaged along the [100] zone axis. Inset: corresponding electron diffraction pattern. This figure is adapted from ref[73].

ters up to several micrometers. An atomic resolution HAADF-STEM image of the edge of one m-BVO particle imaged along the [100] zone axis is shown in figure 2.1(c). Due

2.1. Surface Reduction in Bismuth Vanadate - BiVO_4

to the strong atomic-number contrast, the brighter dots correspond to Bi columns and the weaker ones are V columns. It is clear from the images that the sample consists of monoclinic BVO, because in the tetragonal dreyerite phase the Bi^{3+} and V^{5+} cations are located in centrosymmetric sites in equidistant planes along c . Additionally, no structural modifications or reconstructions were detected at the edge of the displayed m-BVO particle or in any other studied particle. Further, EELS is used to investigate

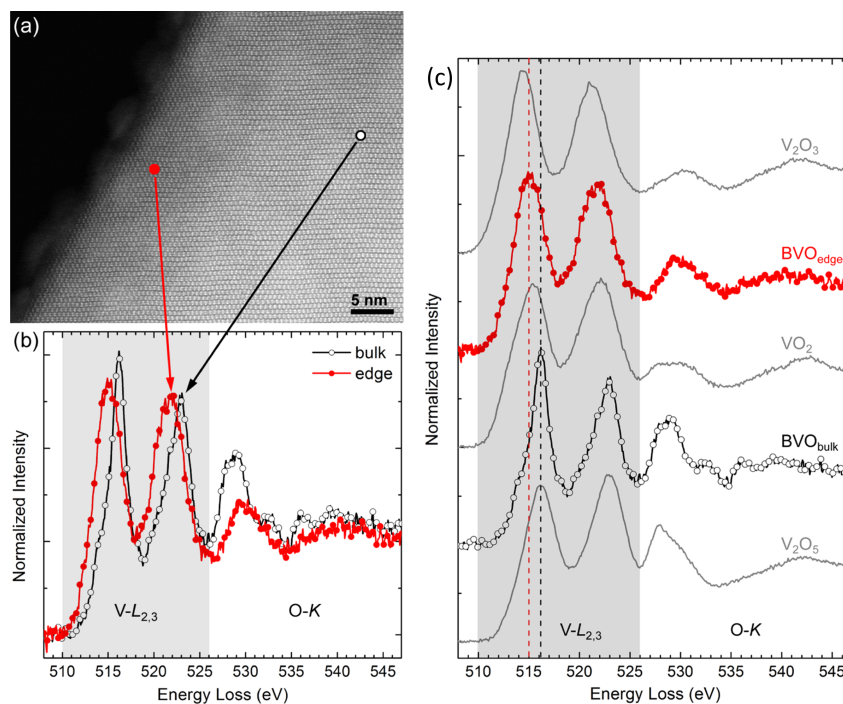


Figure 2.2 – (a) HAADF-STEM image of the edge of a m-BVO particle imaged along $[100]$ showing no structural modifications at the surface. (b) Vanadium $L_{2,3}$ edge and oxygen K edge spectra taken from the areas indicated in panel a. For better comparison, the spectra were normalized to the intensity maxima of the L_2 line. (c) Comparison of the m-BVO spectra with the V_2O_3 , VO_2 , and V_2O_5 reference spectra revealing that vanadium exists in multiple valence states on the surface of the m-BVO particles (red BVO_{edge} spectrum). This figure is adapted from ref[73].

the oxidation state of the vanadium ions in m-BVO by probing the vanadium $L_{2,3}$ edge. Figure 2.2(b) shows the spectra acquired at the edge of the particle and at approximately 25 nm from the edge. Significant changes of the $V-L_{2,3}$ and the $O-K$ edge fine structures are observed at the surface of all scanned particles. The probe was scanned in a small area of about 4 nm^2 around the red and white dots (figure 2.2(a)) to reduce

beam damage, during acquisition of the experimental spectra. For clarity, the spectra

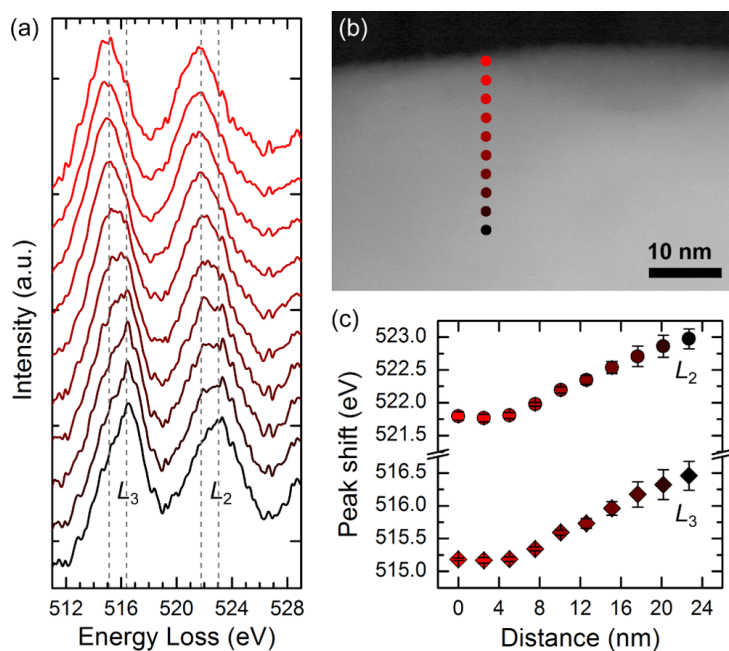


Figure 2.3 – (a) Vanadium L edge showing the L_3 and the L_2 white lines acquired across a line perpendicular to the surface of a m-BVO particle. For better comparison, the spectra were normalized to the intensity maxima of the L_2 line. (b) HAADF-STEM image with the probing path indicated by the dotted line. (c) Energy shift of the V- $L_{2,3}$ white lines across the probing path. Vertical bars indicate standard errors. This figure is adapted from ref[73].

were background subtracted by fitting a decaying power-law function to an energy window just in front of the vanadium edge onset and subsequently normalized to the intensity maxima of the L_2 edge. The extraction of the O- K edge is however hindered by the proximity of the V- $L_{2,3}$ edge. On the surface of the particle, a shift of the V- $L_{2,3}$ edge of ~ 1.2 eV to lower energies is observed. Additionally, the small shoulders appearing at the lower energy side of the L_2 and L_3 white lines of the “bulk” (black) spectrum are not observable at the “edge” (red) spectrum due to the broadening of the peaks. These observations are indicative of the presence of V^{4+} and V^{3+} species, as reported in previous EELS[89, 90] and X-ray absorption spectroscopy[91] studies of $LaVO_3$ and $LaVO_4$. The change of the oxidation state of the near-surface vanadium ions could also be related to the presence of structural defects or impurities. Yet, the measurements did not reveal the presence of defects in any of the studied particles.

2.1. Surface Reduction in Bismuth Vanadate - BiVO₄

Thus, the oxidation state of the surface vanadium ions is found to change owing to oxygen deficiency at the surface.

To explore the extent of the reduction shell, V- $L_{2,3}$ spectra is measured across a line perpendicular to the edge of a m-BVO particle as schematically indicated by the solid dots in figure 2.3(b). The interval between two neighboring spectra is ~ 2.5 nm. Figure 2.3(a) shows the result of the scan across the first 24 nm from the surface. The energy shift of the V- $L_{2,3}$ edge was obtained by fitting each white line to a Gaussian peak using a nonlinear least-squares routine. The result of this fit is depicted in figure 2.3(c). Interestingly, the energy loss of the V- $L_{2,3}$ peaks is approximately the same for the first three surface spectra. An energy shift of ~ 1.2 eV is observed between these surface spectra and the “bulk” (black) spectrum. On the other hand, the energy shift for the intermediate spectra is progressively reduced toward the center of the particle, as these spectra are a linear combination of surface and bulk contributions. Hence, the thickness of the reduction shell is estimated to be approximately 5 nm. The reproducibility of this result was confirmed in all studied grains regardless of the direction of the line scan.

Figure 2.2(c) shows reference spectra obtained from bulk V₂O₃, VO₂, and V₂O₅ together with the m-BVO spectra. The oxidation state of the surface vanadium atoms is determined by using reference V- $L_{2,3}$ spectra for V³⁺, V⁴⁺, and V⁵⁺. It is found that by decreasing the vanadium oxidation state, the V- L_3 peak position shifts toward lower energies by ~ 0.8 eV (V⁵⁺ \rightarrow V⁴⁺) and by ~ 1.7 eV (V⁵⁺ \rightarrow V³⁺). These results are in excellent agreement with previously reported values[89]. Additionally, the position of the L_2 and L_3 peaks for the BVO bulk spectrum and the V₂O₅ spectrum are almost identical, indicating that the oxidation state of the bulk vanadium atoms is +5. On the other hand, the L_3 and L_2 edges of the BVO edge spectrum appear at 515.2 and 521.8 eV, respectively. These values are found to be between those of V₂O₃ and VO₂, implying that vanadium atoms are in the form of V³⁺ and V⁴⁺ at the surface of the m-BVO particles. The oxidation state of the surface vanadium atoms is estimated by fitting a linear regression to the experimental peak positions of all three reference spectra over the vanadium oxidation state. The linear regression produced the following equation of the least-squares line: $E_{V-L_3} = 0.85x + 511.97$ (where x is the vanadium oxidation

Chapter 2. Point Defects in Complex Oxides

state and E_{V-L3} is the peak position), with a regression coefficient R^2 of 0.9988. Thus, the average oxidation state x of the surface vanadium atoms is +3.8, and the fractional contributions of V^{3+} and V^{4+} to the surface spectra are determined as 0.2 and 0.8, respectively. The v_o concentration δ is directly related to the vanadium oxidation state x by $\delta = (5 - x)/2$. This results in a surface composition $BiV^{3.8+}O_{4-\delta}\square_{\delta}$ with $\delta = 0.6$ (where \square represents an v_o). Thus, the m-BVO structure incorporates ~15% of v_o at the surface of the particles. This is not surprising considering that the clinobisvanite phase adopts the scheelite structure, which is known to easily accommodate cations with various oxidation states[92] and to tolerate a significant number of cation and v_o [93, 94]. Moreover, recent calculations have predicted that v_o in m-BVO have very low formation energies[87, 88].

2.1.4 Highlights

The main experimental achievements can be summarized as follows:

- The changes in the V *L*-edge EELS between bulk and surfaces were rationalized.
- Reference V *L*-edge EELS were measured for different vanadium oxides V₂O₃, VO₂ and V₂O₅ to experimentally measure the oxidation state of Vanadium atoms on surface and bulk of BVO.
- Based on the experimental results, it was confirmed that the change in EELS is solely due to the presence of v₀ on the surface.

Theoretical achievements:

- Using ab-initio simulations and comparing the WIEN2k-calculated V *L*-edge EELS with the experimental EELS, the presence of v₀ was confirmed.
- Bonding of Vanadium on surface and the effect of v₀ on the electronic structure of the bulk BVO were investigated further by plotting DOS and 3D electron density for atoms on the surface.
- Further perspectives about the effect of v₀ in BVO were envisaged by summarizing the results of ab-initio simulations.

Here, the “surface” shell comprises the first 5 nm of the material, as evidenced by the experimentally measured 1.2 eV energy shift shown in Figure 3. From experiments, the estimated v_{O} on surface is estimated to be $\sim 15\%$ based on the shift observed in V- $L_{2,3}$ edge spectra. To get better insight into the energy shift of the V- $L_{2,3}$ edge with the presence of v_{O} comparison of theoretical ELNES was made with experimental spectra. Firstly, models with appropriate v_{O} concentration were benchmarked with this comparison. Secondly, the benchmarked models were further used to investigate the electronic structure and its effect on the bulk properties. In this context, it is acceptable to model the system by using a simplified bulk model structure and neglecting the effects of the broken symmetry at the surface.

2.1.5 Theoretical Calculation Details

WIEN2k code with TELNES 3.0 program is employed to investigate the change in the DOS and in the ELNES spectra due to the presence of v_{O} in BVO. A $2 \times 2 \times 2$ supercell was used for all the calculations. The exchange and correlation potential was treated by PBE functional within the framework of spin-polarized calculations. As input structure for the calculations, the clinobisvanite structure[80] with space group I2/b is used; lattice parameters $a = 5.1935 \text{ \AA}$, $b = 5.0898 \text{ \AA}$, $c = 11.6972 \text{ \AA}$, and $\gamma = 90.387^\circ$; and atomic positions given by Bi (0, 1/4, 0.6335), V (0, 1/4, 0.130), O1 (0.1465, 0.5077, 0.2082), and O2 (0.2606, 0.3810, 0.4493); see Figure 1(b). Three cases were studied:

1. BiVO_4 with no vacancies.
2. 12.5% v_{O} simulated with four O1 atoms removed out of 32 oxygen atoms.
3. 12.5% v_{O} simulated with four O2 atoms removed out of 32 oxygen atoms.

In particular, either four O1 or four O2 atoms were removed out of 32 oxygen atoms from the proximity of four different vanadium ions. Thus, both modified m-BVO structures contain 12.5% v_{O} , very close to the $\sim 15\%$ oxygen deficiency required to balance the vanadium reduction observed experimentally at the surface of the m-BVO particles. For BVO with vacancy, the AFM spin-ordering of V atoms is slightly

(20-50 meV) lower in energy as compared to other spin-ordered structures. Therefore, AFM-ordering were studied for all the calculations of BVO with vacancy. The lattice parameters of all structures were relaxed internally using the minimization program `min_lapw`. The following parameters were used for the simulations: the muffin-tin radii R_{mt} were selected as 2.43, 1.67, and 1.51 au for Bi, V, and O atoms, respectively; the valence and core states were separated by 6.0 Ry of energy, and the plane-wave cutoff parameter $R_{\text{mt}} \times k_{\text{max}}$ was set to 7.00. Uniform $5 \times 7 \times 5$ mesh of k points is used to sample the Brillouin zone. An electron beam energy of 200 keV, semicollection angle of 5.0 mrad, and semiconvergence angle of 1.8 mrad were used for the EELS calculations in the TELNES module. A broadening of 1.2 eV was used to account for the instrumental energy resolution.

2.1.6 Benchmarking the Models

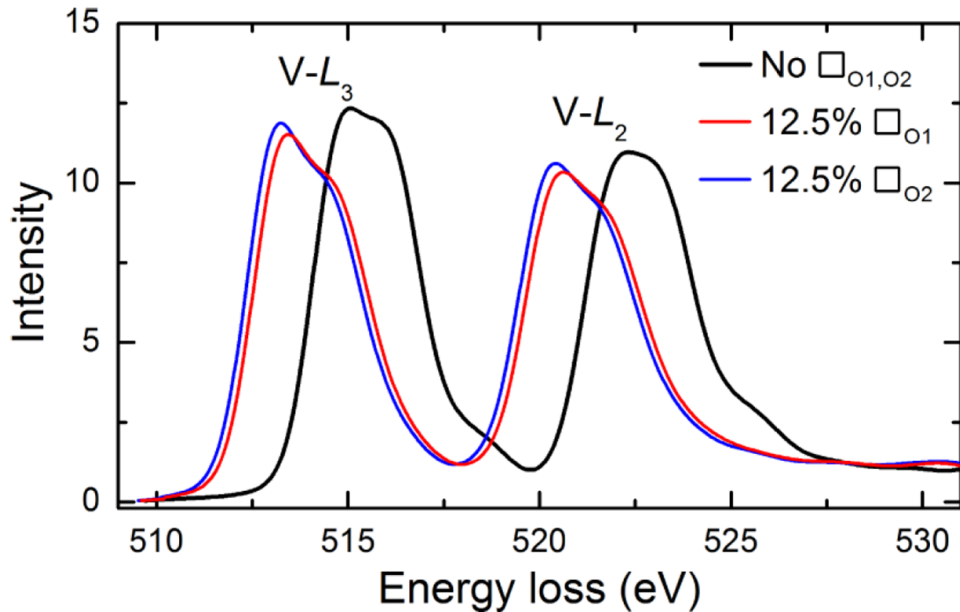


Figure 2.4 – Calculated vanadium $L_{2,3}$ spectra for m-BVO with and without v_0 . The V-L peak positions of the structures containing v_0 (represented by \square) at the O1 and O2 positions are found at lower energies than those of the unmodified m-BVO structure. This figure is adapted from ref[73].

Figure 2.4 shows the calculated V- $L_{2,3}$ ELNES of the unmodified m-BVO structure (black spectrum) and of the v_0 models (red and blue spectra). The calculated spectra

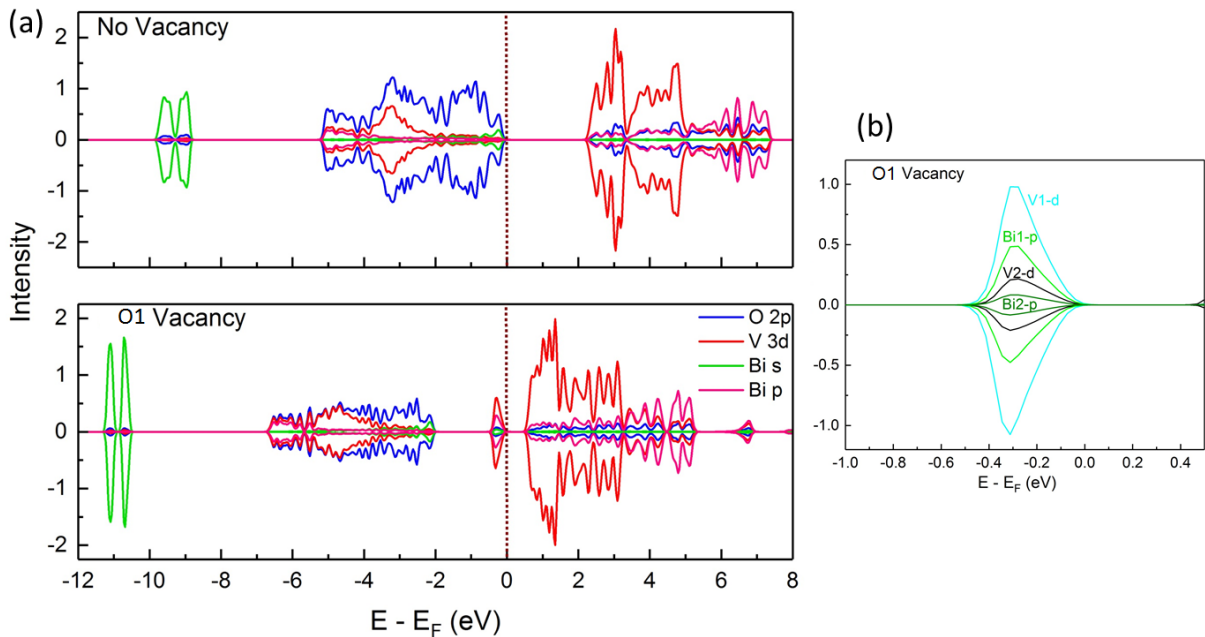


Figure 2.5 – (a) DOS for all three atoms without v_o (top) and with 12.5% O1 v_o (bottom). In both panels, the vertical dashed line at zero-energy marks the Fermi level. (b) V1 and Bi1 indicate the vanadium and bismuth atoms located closer to the O1 vacancy, while V2 indicates the vanadium atom located far from the O1 vacancy. The different atom contributions are indicated by distinct colors.

of both reduced structures are almost identical and very similar to that of the unmodified m-BVO (figure 2.4). The main difference is found in the position of the $V-L_{2,3}$ edges; the edges of the reduced structures are shifted to lower energies by ~ 1.6 eV. Thus, considering the inherent limited precision of DFT calculations in predicting absolute values for energy losses, the theoretical calculations qualitatively reproduce the experimental data.

2.1.7 Picture into Bonding and Charge Distribution

For the interpretation of the EELS spectra, the pDOS for the m-BVO structure with and without v_o were calculated. Shown in figure 2.5(a) are the pDOS for O-2p, V-3d, Bi-6s, and Bi-6p. Both spin-up and spin-dn are equivalent to each other for both unmodified BVO and BVO with vacancy. The results of the unmodified m-BVO structure are in excellent agreement with previously reported theoretical results [95–

2.1. Surface Reduction in Bismuth Vanadate - BiVO₄

97]. The valence band is dominated by O-2*p* states between 0 and -5 eV. Hybridization with V-3*d* states is observed at -3.2 eV, while the top of the valence band is mainly composed of O-2*p* and Bi-6*s* states. Additionally, two additional peaks of primarily Bi-6*s* character are found between -9 and -10 eV. The conduction band is found to be dominated by V-3*d* states, with significant contributions from O-2*p* and Bi-6*p*. When comparing the pDOS for the structure with no vacancies and with 12.5% vacancies, it is evident that the V-3*d* conduction states have shifted by ~1.5 eV toward the Fermi level. A shift of ~2 eV is also observed for all occupied DOS away from the Fermi level. Additionally, in the unmodified m-BVO, a prominent resonance between the O-2*p* and V-3*d* bands is evident at $E - E_F = -3.2$ eV. Such resonance is still present in the BVO structure with vacancies ($E - E_F = -4.5$ eV) but is depleted due to the v_o and subsequent electric distribution. More interestingly, v_o give rise to new localized donor states close to the Fermi level, about 0.64 eV below the conduction band. These defects are shallow donors as determined by previous transition-energy calculations[87]. They are dominated by V-3*d* states, implying that vanadium is reduced and contains more occupied *d* states as compared to the unmodified structure. The states near the Fermi level are decomposed (see figure 2.5(b)) in order to find out the contribution of each atom. The largest contribution to the new localized donor states arises from the vanadium atom (V1) located closer to the O1 vacancy, and also from Bi1-6*p* states (where Bi1 is the bismuth atom located closer to the O1 vacancy). The other states (V2-3*d* and O1-2*p*) have a negligible impact. Thus, the calculations support the reduction of vanadium to a lower oxidation state. Additionally, the calculated magnetic moments of the Vanadium ions close to vacancy is around $0.011 \mu_B$. To explicitly address the nature of the localized states observed in the DOS, the charge density is computed restricted to an energy window containing these states. These valence charge density maps are used to generate a visual representation of a given selection of bands and are computed using the *lapw5* package of WIEN2k. This package is used to obtain 2D slices from the electronic density file calculated by WIEN2k. The 3-dimensional visualization of charge density was extracted by combining the calculated 2D slices using the *wien2venus* script written by Masao Arai[98]. Figure 2.6 shows the charge density plot constructed from the donor band corresponding to the electronic

Chapter 2. Point Defects in Complex Oxides

Table 2.1 – Selected interatomic distances for the BVO structures with and without vacancies.

No vacancy		12.5% vacancy	
Distance in (Å)			
V···O1	1.767	V1···O1	1.728
V···O1	1.691	V1···O2	1.722
			1.719
		V2···O1	1.767
			1.786
		V2···O2	1.747
			1.685

states induced by a O1 vacancy in m-BVO. The localized states corresponding to this particular valence band mostly have V1-3*d* characteristics, with participation of Bi1-6*p* states. More importantly, the present results indicate a charge localization of the two defect electrons on an ideal bond joining the vanadium (V1) neighboring the O1 vacancy and the bismuth (Bi1) atom at the other side (see figure 2.6). On other hand, the defect states are least concentrated on the vanadium atom (V2) and bismuth atom (Bi2) which are away from the O1 vacancy. Additionally, by comparing the bond distances of the pristine bulk structure with those of the reduced structure, it is observed that the rearrangement following the O1 removal is shown by a significant displacement of the V1 neighbor away from the vacancy site with a shortening of the V1-O1 distance and an increase of the V1-O2 distances (see Table 2.1).

In order to find out the formal charge state of the vanadium ion close to the v_0 and to compare it with the vanadium charge state in the bulk m-BVO structure the topological analysis of the electron density is performed introduced by Bader[99, 100]. One should be aware that Bader charges do not match the formal charge state. For example, the Bader charge of vanadium in the bulk m-BVO structure is calculated to be +2.186 |e| (see Table 2.2). Thus, a more meaningful result is obtained by using reference states. For this reason, Bader charges for V^{3+} , V^{4+} , and V^{5+} were calculated by using the AIMS module of WIEN2k from three reference vanadium oxides, namely V_2O_3 , VO_2 , and V_2O_5 . Then, the same analysis was carried out for the unmodified bulk

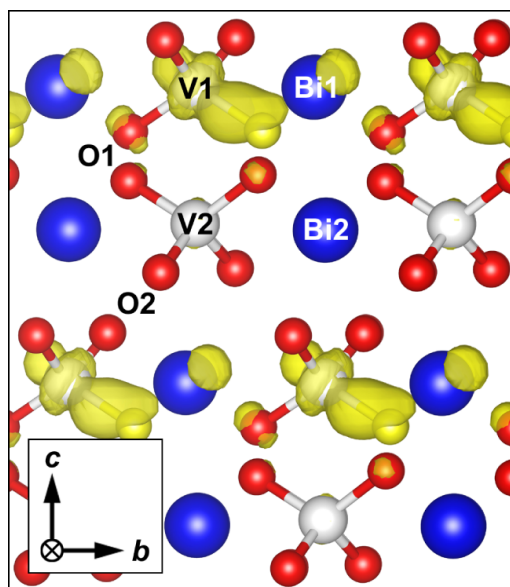


Figure 2.6 – Spatial representation of the charge density plot constructed from the donor band corresponding to the electronic states induced by an O1 vacancy in m-BVO. Regions with an excess charge and O1 vacancies are shown as yellow lobes and spheres, respectively. This figure is adapted from ref[73].

m-BVO structure and for BVO with vacancies (see Table 2.2). Surprisingly, although the structural environment of the V1 and V2 ions in the BVO structure with vacancies is very different, the values for the Bader charge are almost the same for V1 and V2 (+2.07 and +2.09 |e|), and very close to the VO_2 reference (+2.05 |e|), resulting the oxidation state of vanadium to be +4. This analysis contradicts the charge density presentation in figure 2.6. According to figure 2.6, only one of the vanadium atom (V1) which is close to the O1 vacancy has most of the defect states and there are almost no states on vanadium atom (V2) which is away from the vacancy. However, Bader analysis was unable to provide any quantitative differences between the two vanadium atoms. Such shortcomings have been reported in previous studies[101, 102] where Bader analysis were not helpful to provide quantitative differences of charge disproportionation in various materials. This problem is mainly due to the admixture of ionic and covalent bonding which is not detected in Bader charge analysis.

To overcome this problem, the Born-effective charges (BEC) were computed using Berry-pi module[38] with WIEN2k. The BEC tensor was computed which provides the polarized charges induced by the application of an electric field. The diagonal

Chapter 2. Point Defects in Complex Oxides

Table 2.2 – Bader charges of vanadium atoms in three reference vanadium oxides, and in BVO with and without vacancies.

Vanadium atom	Bader charge
V^{3+} - V_2O_3	+1.81
V^{4+} - VO_2	+2.05
V^{5+} - V_2O_5	+2.21
bulk m-BVO	
V^{5+}	+2.186
12.5% (O1) vacancy	
V1	+2.07
V2	+2.09
12.5% (O2) vacancy	
V1	+2.09
V2	+2.07

elements of BEC tensor were calculated by displacing the atom in x,y and z directions and then average is calculated for vanadium atoms in BVO (with and without oxygen vacancy) and vanadium oxides (V_2O_5 and VO_2). Table 2.3 shows the computed Born-effective charges. The Born-effective charges for vanadium atoms in V_2O_5 and VO_2 are reasonably to their nominal oxidation states. For V_2O_5 (+5.32) it is higher than +5 and for VO_2 (+3.86) it is slightly lower than +4. This shows an uncertainty of ± 0.32 in determining the oxidation state of vanadium oxides. For, BVO bulk, the Born-effective charge of Vanadium ion is around +4.83 (close to +5) whereas for BVO with vacancy the two vanadium ions have clearly different charges. As expected, the V1 atom closer to the O1 vacancy has Born-effective charge of +3.53 and the V2 atom which is away from vacancy has a value of +5.04. Hence, the Born-effective charge analysis clearly distinguishes between the two vanadium atoms by indicating that only the Vanadium atom closer to the vacancy (V1) is reduced and the one away from vacancy (V2) is not affected. Thus, the average oxidation state of the two vanadium atoms is around +4.25. This value is slightly higher than the experimentally measured vanadium oxidation state of +3.8. The slight difference in the results can be due to consideration of 12.5% v_0 in calculation instead of 15% v_0 observed from the experiments. The Born-effective charge analysis also shows an uncertainty of around

2.1. Surface Reduction in Bismuth Vanadate - BiVO₄

Table 2.3 – Born-effective charges of vanadium atoms in reference vanadium oxides, and in BVO with and without vacancies.

Vanadium atom	Born-effective charge
V ⁴⁺ - VO ₂	+3.85
V ⁵⁺ - V ₂ O ₅	+5.32
bulk m-BVO	
V ⁵⁺	+4.83
12.5% (O1) vacancy	
V1	+3.52
V2	+5.02
12.5% (O2) vacancy	
V1	+5.04
V2	+3.54

± 0.32 in determining the oxidation of vanadium oxides. Considering this error bar the calculated average oxidation state of vanadium ions in BVO with vacancy is closer to the experimental value of +3.8.

Also, due to the finite supercell size, the simulations with high oxygen vacancy of 12.5% also creates a perfectly ordered array of vacancies owing to periodic boundary conditions. But in reality with experimental sample of BVO, the oxygen vacancy are not ordered but distributed evenly as evident from HAADF-STEM images. This can be avoided by considering large supercell with disordered oxygen vacancy distribution. Given a very good agreement of calculated-EELS with the experimental recorded data and to reduce computation time, I kept my theoretical calculations limited to the smaller supercell size.

2.1.8 Conclusions

Calculations show that v_0 in m-BVO give rise to localized donor states about 0.64 eV below the conduction band. These defects act as shallow donors and are responsible for the n -type conductivity, as previously suggested by Yin et al.[87] . Thus, the presence of a reduction shell in the studied m-BVO particles creates an $n^+ - n$ homojunction, which is known to enhance the charge-separation efficiency [103, 104].

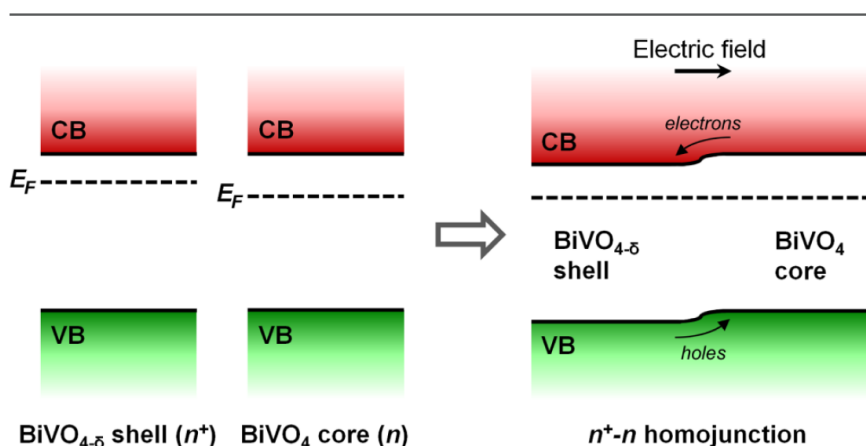


Figure 2.7 – Schematic energy bands of the separate phases (left) and after the formation of the n^+n homojunction (right). The valence band, conduction band, and Fermi level are indicated as VB, CB, and E_F , respectively. When BiVO₄ and BiVO_{4-δ} are brought into contact, the Fermi levels of both phases align, causing a bending of the energy bands. This figure is adapted from ref[73].

However, as opposed to previous results on homojunctions in m-BVO [103, 104], in the present case the homojunction is reversed, i.e. the bulk (core) m-BVO is a n -type semiconductor and the reduction shell is an n^+ -type semiconductor (figure 2.7). Thus, in this situation an inner electrical field is established in the direction of the n^+ -type to the n -type semiconductor (from the shell to the core of the BVO particles). As a result, the energy bands of the core BVO would shift upward while those of the reduced BVO shell shift downward in order to align the Fermi levels of both semiconductors. At this band edge position, the photogenerated electrons of the conduction band of the n -type core transfer to that of the n^+ -type shell, and simultaneously, holes on the valence band of the n^+ -type shell move to that of the n^- type core under the influence of the potential setup by the band energy difference. As a consequence, the oxygen evolution reaction at the surface of the m-BVO particles is expected to be greatly reduced. Thus, these findings suggest that the photochemical behavior of "pristine" m-BVO needs to be interpreted in terms of a distinct surface shell of different properties than the actual bulk BVO. This result emphasizes the importance of surface and grain boundary effects in this new candidate for photoelectrochemical energy conversion and wastewater purification.

2.2 Strain Effects on Point Defects in SrMnO₃

The following part in the section has been extracted with some modifications from the article titled as "Strain-driven oxygen deficiency in multiferroic thin films SrMnO₃" [105] published by myself together with Pu Yu, Jingyi Guo, Cécile Hébert, Daniele Passerone, Rolf Erni and Marta Rossell. The SMO films on five different substrates were grown by Jingyi Guo and Pu Yu at Tshingua University, China, and the experimental measurements were performed by Marta Rossell, theoretical simulations and interpretation with experimental results were done by myself, and Cécile Hébert, Daniele Passerone and Rolf Erni guided me through this work. I would like to thank all of them for their great effort and contribution.

2.2.1 Introduction

In the past decade, there has been a flurry of research activities aimed at discovering new multiferroic materials exhibiting simultaneous magnetic and ferroelectric order with strong magnetoelectric coupling above room temperature. The tremendous interest in this class of multiferroics is motivated by the expectation of integrating them into low-power spintronic nanodevices, where the magnetic order is controlled by low energy consuming electric fields instead of magnetic fields. The formation of magnetic moments usually results from partially filled *d* shells [106] of transition metal cations which are available for hybridization with the *p* orbitals of the surrounding oxygen anions. This limitation has boosted intense research on alternative routes to combine ferroelectricity and magnetism in a single phase [107].

Using first principles calculations, Fennie and Rabe [108] predicted that by applying tensile strain to EuTiO₃, normally an antiferromagnetic-paraelectric (AFM-PE) material [109], a ferromagnetic-ferroelectric (FM-FE) phase could be produced as a result of a strong interaction between the spin ordering and the lattice phonons, i.e., by the so-called "spin-phonon coupling" [110]. Yet, a very weak magnetoelectric coupling was experimentally confirmed [110]. The origin of the weak ferroic coupling in EuTiO₃ was ascribed to magnetism and ferroelectricity originating from different

Chapter 2. Point Defects in Complex Oxides

lattice sites [111]. More recently, theoretical calculations suggested that, similarly to EuTiO_3 , strain-driven multiferroicity associated with spin-phonon coupling should arise in strained SrMnO_3 (SMO) [112]. In bulk form, SMO is observed to have a PE cubic perovskite structure with G-type AFM ordering arising from linear Mn-O-Mn superexchange interactions. Under epitaxial strain a polar instability in the FM phase leads to a substantial decrease in energy, which stabilizes the FM-FE multiferroic phase over the bulk AFM-PE phase [112]. However, one aspect that was overlooked in the theoretical predictions is the tendency of the SMO structure to incorporate v_{O} , which makes it very difficult to synthesize fully stoichiometric SMO samples [113, 114]. Thus, for example, the large dispersion reported in literature for the Néel temperature of unstrained SMO (between 233 and 260 K) [115–118] is ascribed to differences in the oxygen stoichiometry of the samples used. Moreover, epitaxial strain is known to critically affect the v_{O} concentration in conventional perovskites.

In this section, I describe several SMO thin films grown under different strains and analysed by aberration-corrected high-angle annular dark-field scanning transmission electron microscopy (HAADF-STEM) and electron energy-loss spectroscopy (EELS). Experimental EELS results are used to further investigate the effect of v_{O} on the O-K edge of SMO using WIEN2k.

2.2.2 Experimental Details

Five SMO thin films with thicknesses in the range of 10-13 nm grown by PLD assisted reflection high-energy electron diffraction (RHEED) assisted pulsed laser deposition on $\text{LaSrAlO}_4(001)_t$, $\text{LaAlO}_3(001)_{pc}$, $(\text{La}_{0.3}\text{Sr}_{0.7})(\text{Al}_{0.65}\text{Ta}_{0.35})\text{O}_3(001)_{pc}$, $\text{SrTiO}_3(001)_c$, and $\text{DyScO}_3(110)_o$ substrates, where t, pc, c, and o denote tetragonal, pseudocubic, cubic, and orthorhombic indices, respectively. For simplicity, from now on I will refer to them as LSAO, LAO, LSAT, STO, and DSO. These substrates were used to induce nominal epitaxial strain values of -1.30%, -0.32%, 1.63%, 2.56%, and 3.78%, respectively. Detailed experimental details can be found in Agrawal et al. [105].

2.2.3 Experimental Results

HAADF-STEM images of all five SMO films are shown in figure 2.8(a)-(e). Representative lattice parameter maps showing the variation in lattice parameter along the out of plane (OOP) and in-plane (IP) directions are shown in the central and right panels of figure 2.8(a)-(e), respectively. Overall, the IP parameters of the SMO films and the substrate materials show negligible differences indicating that the SMO films are fully strained. Besides, the OOP parameters are homogeneously strained over the whole thickness of the thin films. Thus no strain gradients from the substrate interface towards the upper layers of the films were detected, as reported in Ref. [113]. Subsequently, the IP and OOP lattice parameters for each film were determined from each image by averaging over a rectangular area containing the whole SMO film. The obtained values as well as the c/a ratio (where c/a is the ratio between the OOP and IP pseudocubic lattice), and the unit-cell volume are plotted against the epitaxial strain in figure 2.9. One can see that the first two quantities change linearly as a function of the imposed strain between -1.30% and 2.56%, that is, excluding the SMO/DSO film. However, from purely geometrical considerations, one would expect the c/a ratio to be smallest for the SMO/DSO film. But the presence of cracks in the SMO films grown on DSO, shown in Agrawal et al.[105] most likely formed during TEM sample preparation is the reason of the mismatch. Nevertheless, it is found that the IP lattice parameters of the SMO films grown on LSAT, STO, and DSO are larger than the OOP parameters, while this is reversed for the SMO films grown on LSAO and LAO.

Figure 2.10(a) and 2.10(b) shows a comparison of the manganese $L_{2,3}$ and oxygen K edges among the series of SMO films. The obtained spectra show clear changes in peak-height changes and energy shifts as a function of strain. The Mn- $L_{2,3}$ edge corresponds to excitations of the Mn $2p$ electrons into empty Mn $3d$ states. They are indicated as L_3 and L_2 in figure 2.10(a), respectively. The L_3 peaks corresponding to the films under tensile strains appears at lower energy than those corresponding to the compressed SMO films. Additionally, the relative intensity of the L_2 line with respect to the L_3 line progressively decreases from LSAO (black curve) to DSO (red curve). These observations indicate an increase of the electron doping of the Mn $3d e_g$

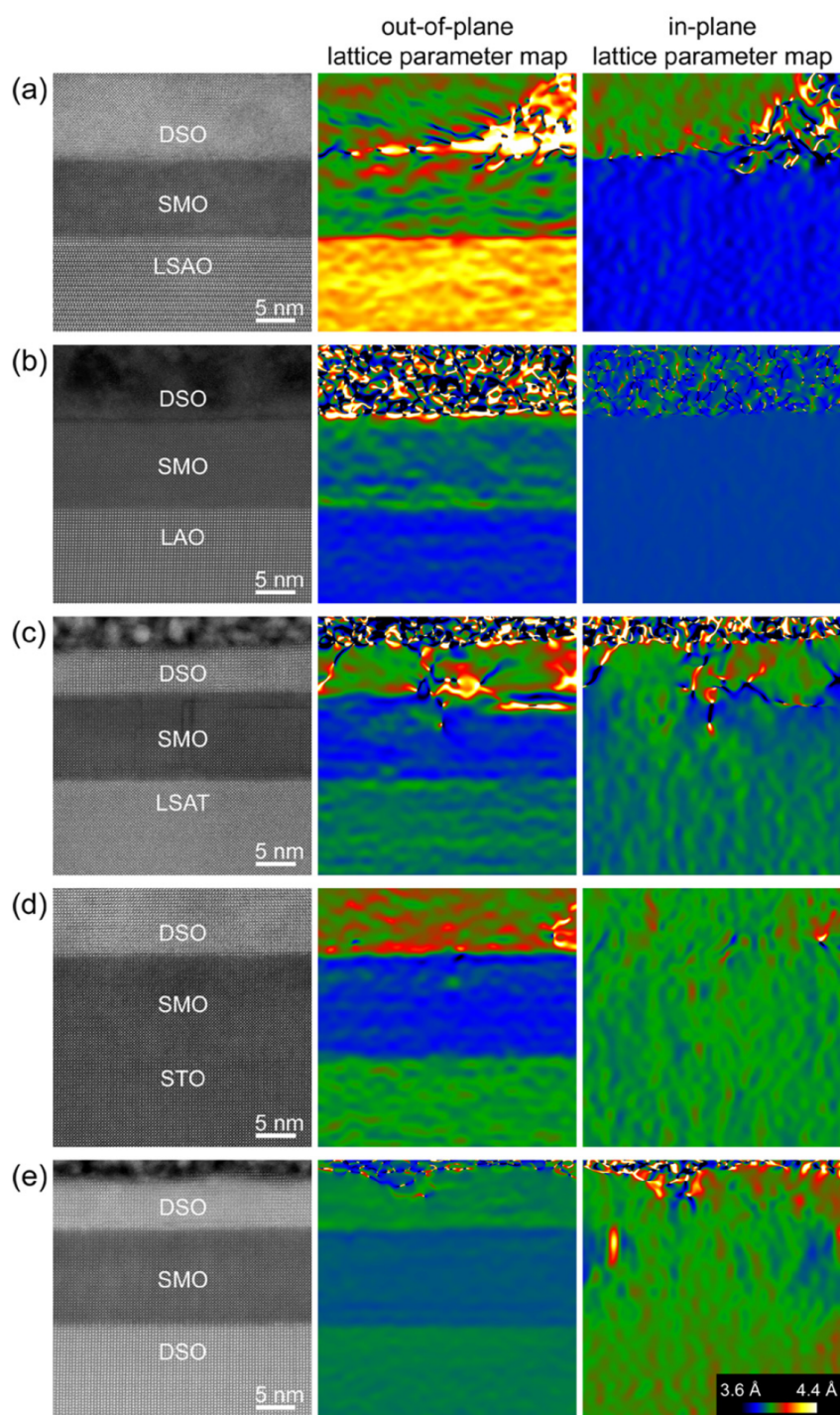


Figure 2.8 – Strain analysis of SMO films grown on (a) LSAO, (b) LAO, (c) LSAT, (d) STO, and (e) DSO. Maps of out-of-plane (middle panels) and in-plane (right panels) lattice parameters determined from GPA of HAADF-STEM images (left panels). The color scale is the same for all panels. This figure is adapted from ref[105].

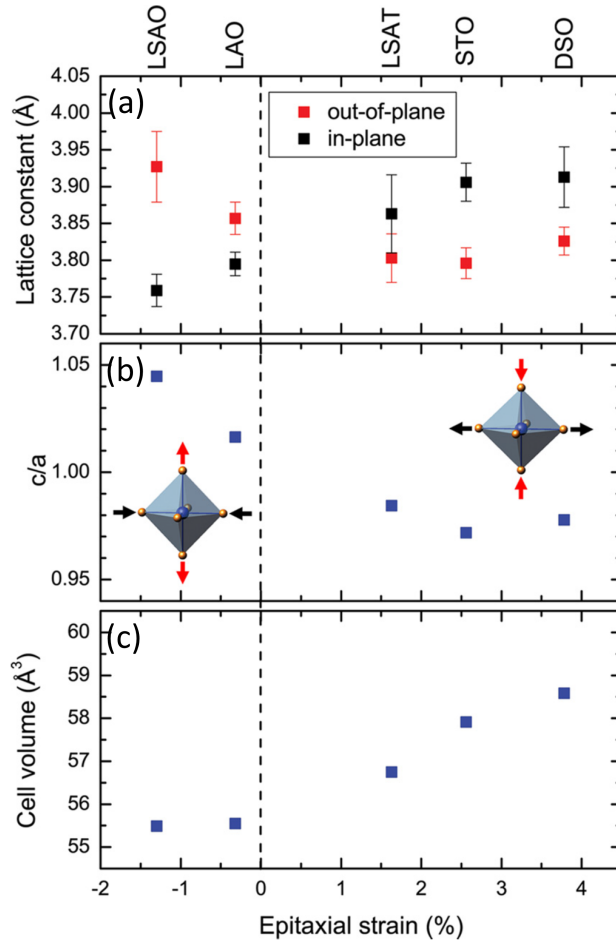


Figure 2.9 – Structural parameters obtained by GPA of HAADF-STEM images as function of nominal strain. (a) Out-of-plane and in-plane lattice parameters of the SMO pseudocubic unit cell; (b) c/a lattice parameter ratio; (c) unit-cell volume. This figure is adapted from ref[105].

band with tensile strain. Complementary information can be obtained from the O- K edge, resulting from excitations of O $1s$ electrons into available O $2p$ empty states. The O- K near-edge structure of the SMO strained series in figure 2.10(b) exhibits three major peaks, a, b, and c, caused by hybridizations of unoccupied O $2p$ orbitals with Mn $3d$, Sr $4d$, and Mn $4sp$ orbitals, respectively[119–121]. For clarity, all spectra were normalized to the intensity maxima of the main peak b, and the same energy shift used to align the Mn- L_2 edges was applied to the O- K spectra. By doing so, the O- K_b peak in all spectra is aligned at 537 eV, while the positions and intensity of the adjacent O- K_a and O- K_c peaks change steadily with strain as indicated with dashed lines. According

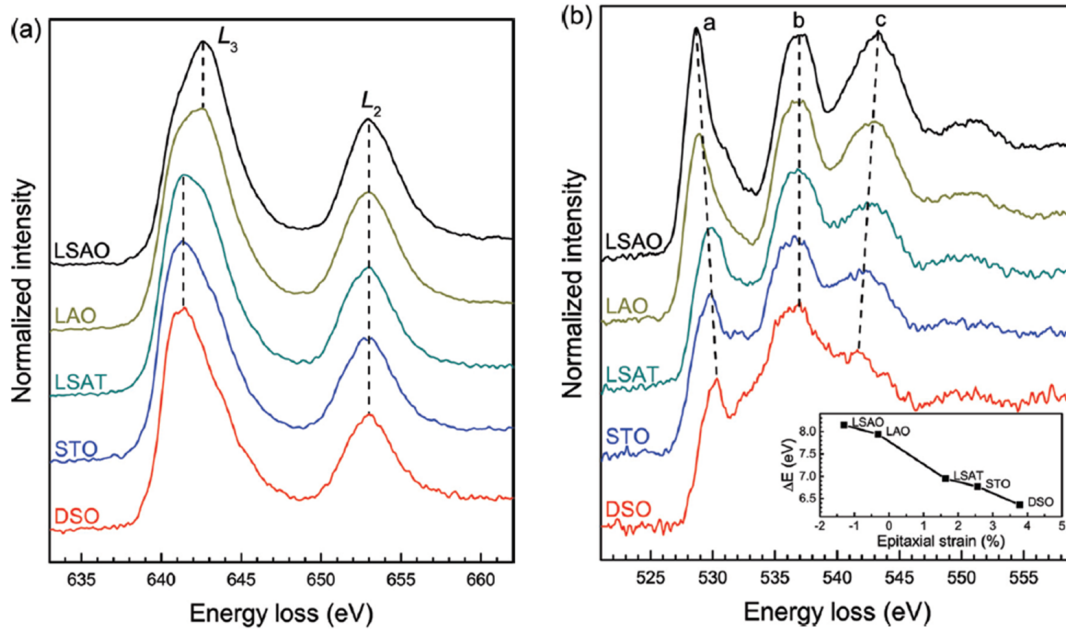


Figure 2.10 – Comparison of Mn- L and O- K edges among the SMO films grown on different substrates. (a) The energy scales have been shifted so the L_2 lines match. The intensity is normalized to the L_3 line. Dashed lines are used to show the shift in energy of the L_3 peak. (b) The energy scales have been shifted so the main peaks at 537 eV are aligned, and the intensity normalized. Dashed lines are used to show the shift in energy of the adjacent peaks. The energy difference between the O- K_b main peak and the O- K_a prepeak is quantitatively shown in the inset. All spectra are displaced vertically for clarity. This figure is adapted from ref[105].

to previous reports, since the O- K_a prepeak has a very strong contribution from the Mn $3d_{eg}$ band occupancy, it can be used to extract information on the Mn oxidation state[122].

Estimation of the local oxidation state of Mn ions of the SMO films were made by applying the procedure reported by Varela et al.[122]. Thus, by fitting Gaussian peaks to the O- K_a and O- K_b peaks, the peak positions were determined and the energy difference [see inset in figure 2.10(b)] was used to obtain an average oxidation state of +4.04, +3.98, +3.70, +3.65, and +3.53 for the SMO films grown on LSAO, LAO, LSAT, STO, and DSO, respectively. Clearly, the increment in the tensile strain leads to a reduction in the manganese oxidation state.

2.2.4 Highlights

The main experimental achievements can be summarized as follows:

- Variations in O *K*-edge and Mn *L*-edge EELS were experimentally recorded for the five different strained SMO films.
- Oxidation states of Mn atoms in different SMO films were determined based on the changes observed in the position of peaks in O *K*-edge EELS.
- It was not clear from the experiments whether the change in EELS is due to v_o or strain or both.

Theoretical achievements:

- Ab-initio models were prepared with different concentration of v_o and strained lattice parameters to match the trend of EELS observed in experimentally-recorded EELS.
- Based on the comparison with the experimental data, it was demonstrated that the change in the EELS is mainly due to the effect of v_o and to a lesser extent to the effect of strain.
- Further investigation revealed the effect on bonding states of two different kind of oxygen classified on the basis of distance from the Mn-atom around the vacancy.

2.2.5 Computational Details

To compare experimental spectra with theoretical ELNES, and to investigate the effect of v_0 on the O-*K* and Mn-*L*_{2,3} edge fine structures, three systems out of five were selected. They are namely LSAO, LSAT, and DSO, and correspond to the maximum compression (LSAO) and tensile (DSO) strains, and an additional intermediate point (LSAT) in the low tensile regime.

WIEN2k calculations were performed using the generalized gradient approximation GGA+*U* method [123]. The Perdew-Burke-Ernzerhof (PBE) generalized gradient approximation (GGA) was employed for the exchange-correlation function under the framework of spin polarized calculations. A Coulomb interaction $U = 2.7$ eV and on-site exchange interaction $J_H = 1.0$ eV were used to treat the Mn *d* electrons [112]. The same U values were adopted and the G-type AFM Mn spin-ordering were studied for all the calculations with WIEN2k. Uniform $8 \times 8 \times 8$ mesh of *k* points is used to sample the Brillouin zone. The valence and core states were separated by 6.5 Ry of energy and the plane-wave cutoff parameter $R_{\text{mt}} \times k_{\text{max}}$ was set to 7.00. The EELS spectra were computed using the TELNES 3.0 module of WIEN2k using an electron beam energy of 200 keV, semicollection angle of 5 mrad, and semiconvergence angle of 2 mrad. A broadening of 1.0 eV was used to account for the instrumental energy resolution.

To clarify the influence of strain and v_0 on the electronic structure of SMO, each effect was addressed separately. Three sets of calculations were performed:

- Strained + no vacancies. For all three structures, a $2 \times 2 \times 2$ supercell and optimized lattice parameters were used in the calculations.
- Unstrained + vacancies. For this set of calculations all supercell structural models were based on a cubic unit cell with lattice parameter $c = 3.80$ Å [115]. A $2 \times 2 \times 2$ supercell was modeled for LSAT by removing one oxygen out of a $\text{Sr}_8\text{Mn}_8\text{O}_{24}$ unit, and a $2 \times 2 \times 2$ supercell was used for DSO by removing two oxygen out of a $\text{Sr}_8\text{Mn}_8\text{O}_{24}$ unit to get a Mn oxidation state of +3.75 and +3.50, respectively. These values are very close to the ones observed experimentally, i.e., Mn(LSAT)

Table 2.4 – Experimental lattice parameters and optimized out-of-plane parameters calculated for strained SMO structures without v_{O} .

Substrate	a=b (Å)	c (Å)	Optimized parameter c (Å)
LSAO	3.756	3.927	3.925
LSAT	3.868	3.803	3.624
DSO	3.955	3.826	3.626

= +3.70 and Mn(DSO)=+3.53. Subsequently, the lattice parameters of the cells were kept unaltered and the internal atomic coordinates were optimized.

- Strained + vacancies. A $2 \times 2 \times 2$ supercell was modeled for LSAT by removing one oxygen out of Sr₈Mn₈O₂₄, and a $2 \times 2 \times 2$ supercell was used for DSO by removing two oxygen out of Sr₈Mn₈O₂₄. The optimized *c* lattice parameters were used for the calculations, and then the internal atomic positions were relaxed.

2.2.6 Computational Results

The epitaxial constraint was set by fixing the IP parameters to match those of the experimental substrates. Subsequently, the OOP lattice parameters and internal atomic coordinates were optimized for all the structures. The experimental substrate parameters, and the measured and optimized OOP parameters, are tabulated in Table 2.3. Note that for LSAO the optimized *c* parameter is in very good agreement with the experimental value, while for the films under tensile strain (LSAT, DSO) the optimized parameters are about 5% smaller than the experimental ones, suggesting the presence of v_{O} in the tensile-strained SMO films. The O-*K* edge EELS spectra were calculated for the above mentioned three cases. The calculations were repeated for all nonequivalent oxygen atoms and appropriately averaged. Similar to the experimental data, all obtained spectra are normalized to the intensity maxima of the O-*K*_b peak, and an energy shift of a few eV was applied to align the peak at 537 eV. All calculated oxygen *K* edge spectra of the strained and unstrained SMO structures with and without v_{O} are shown in figure 2.11. The good agreement with experiment concerns the trend

Chapter 2. Point Defects in Complex Oxides

in energy difference between the O- K_a prepeak and the O- K_b main peak, as well as the intensity ratio between the two peaks which decreases with increasing tensile strain. The calculated O- K edge spectra assuming the presence of v_o [figure 2.11 (b) and 2.11(c)] compare very well with the experimentally obtained O- K edge spectra [figure 2.11(d)]. On the other hand, if no vacancies are included in the structural

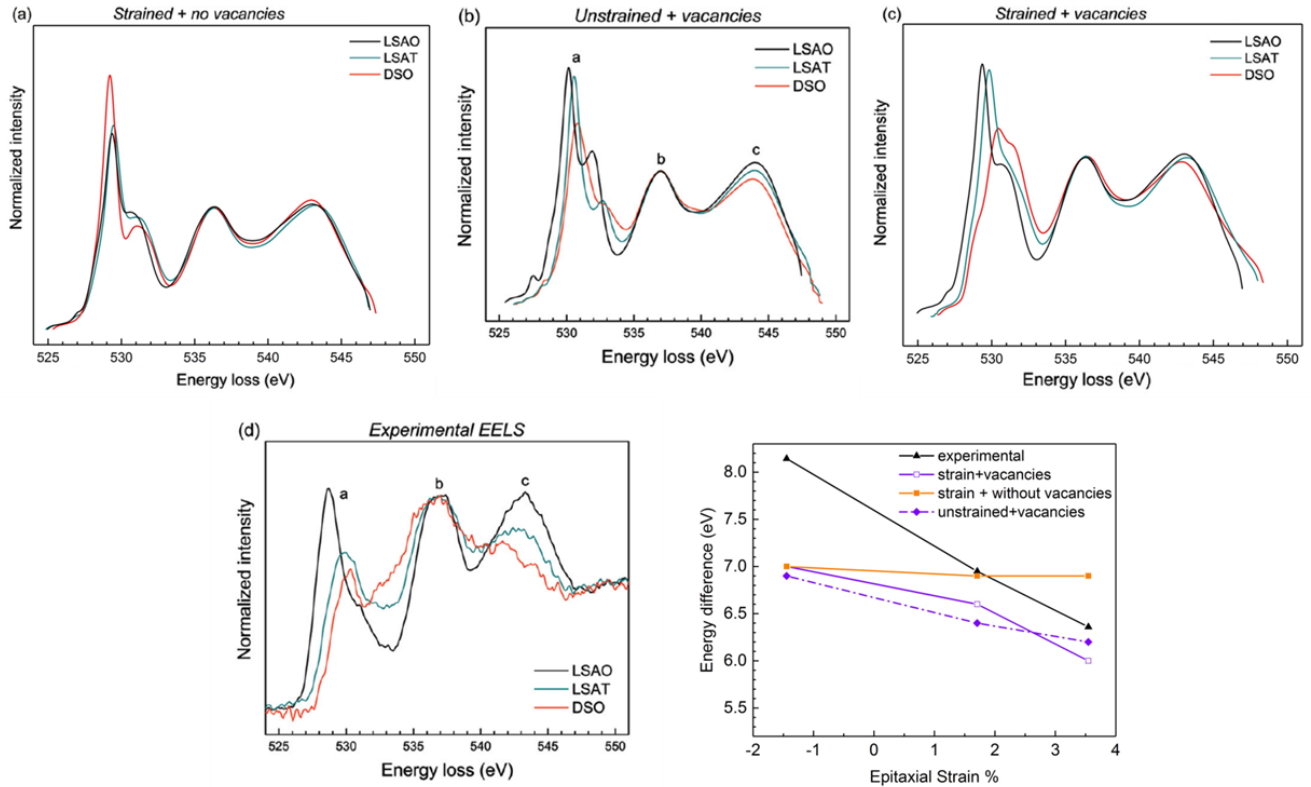


Figure 2.11 – O- K edge EEL spectra of SMO structures on LSAO, LSAT, and DSO. (a) The O- K edge spectra are calculated assuming strained lattice parameters and no v_o . (b) The O- K edge spectra are calculated assuming unstrained lattice parameters and the presence of v_o . (c) The O- K edge spectra are calculated assuming strained lattice parameters and the presence of v_o . (d) Experimental O- K edge spectra. (e) Energy difference between the O- K_a prepeak and the O- K_b main peak as a function of epitaxial strain for all four cases.

models, neither the experimentally observed depletion of the O- K_a peak with respect to the O- K_b peak nor the peak energy difference decrease upon increasing tensile strain is reproduced [figure 2.11(a)]. These findings are summarized in figure 2.11(e), which shows the energy difference between the O- K_a and O- K_b peaks for all cases. The

2.2. Strain Effects on Point Defects in SrMnO₃

simulations assuming the presence of v_0 in the strained SMO structures gives the best match to the experimental results, whereas for the strained SMO structures without v_0 the energy difference is almost constant across the different substrates. Besides, it was also discovered that the SMO structures that incorporate v_0 are energetically more favorable in the presence of tensile strain (by 0.29 eV for LSAT and 0.30 eV for DSO). The origin of this energy reduction is mainly of electrostatic nature, as tensile strain reduces the electron-electron repulsion along the broken Mn-O-Mn bond axis[58].

Figure 2.12 shows the DOS of the O 2*p* and Mn 3*d* (spin-up and spin-dn) states in the

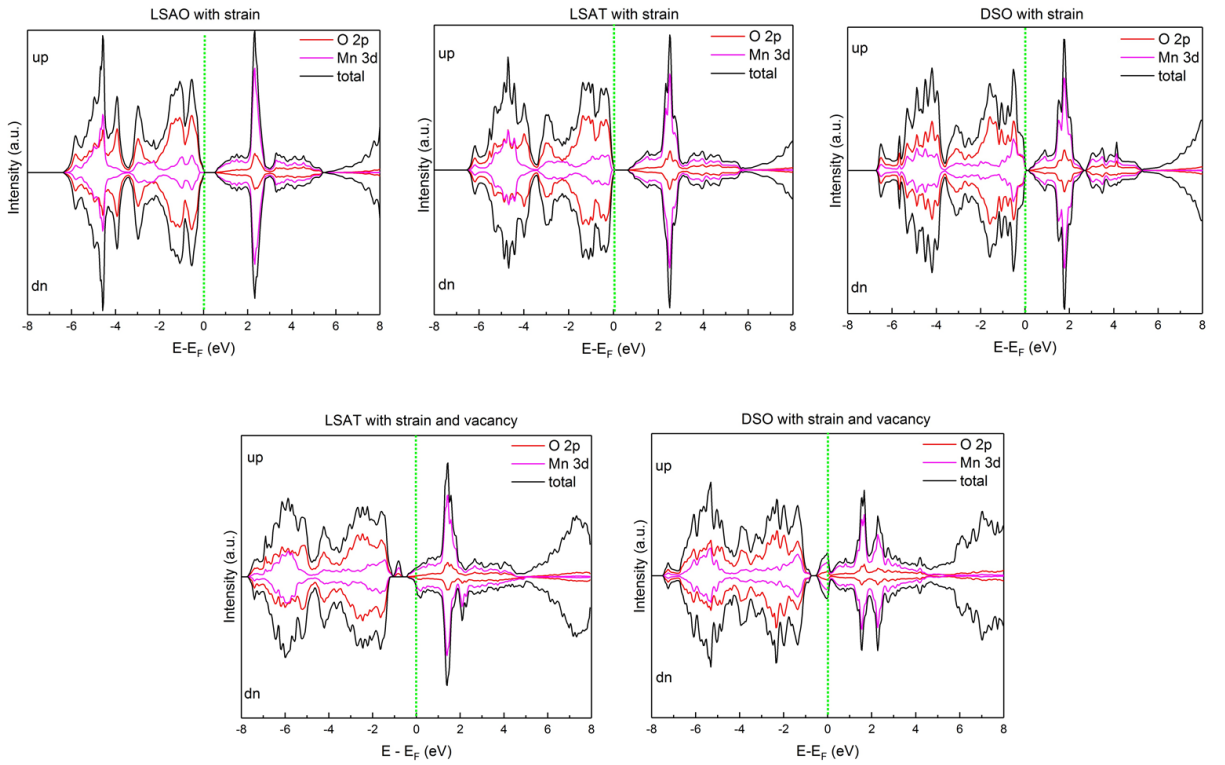


Figure 2.12 – DOS of the Mn 3*d*, O 2*p* and total (spin-up and spin-dn) states in strained SMO structures on different substrates (LSAO, LSAT, and DSO) with and without v_0 .

strained SMO structures on LSAO, LSAT, and DSO with and without v_0 . The calculated magnetic moments of Mn ions in all the structures is around $2.4 \mu_B$. We notice the following (1) all strained SMO structures have reasonable band gap and with the least band gap of 0.2 eV for SMO on DSO (2) one sharp peak around 2 eV is observed in the pDOS for both O 2*p* (spin-up and spin-dn) and Mn 3*d* (up- and down-) for all SMO structures without vacancies (see top panels in figure 2.12) (3) when comparing

Chapter 2. Point Defects in Complex Oxides

Table 2.5 – Calculated Mn–O interatomic distances in SMO on LSAO, LSAT, and DSO.

Mn - O distance Å						
Substrate	O1	O2	O3	O4	O5	O6
LSAO	1.88	1.88	1.88	1.88	1.97	1.97
LSAT	1.93	1.93	1.93	1.93	1.81	1.81
DSO	1.98	1.98	1.98	1.98	1.81	1.81
Substrate	O1	O2	O3	O4	O5	O6
LSAT						
Close	1.92	1.92	1.80		1.80	1.80
Far	1.97	1.97	1.91	1.95	1.81	1.81
DSO						
Close	1.96	1.96	1.80		1.85	1.85
Far	2.02	2.02	1.99	1.97	1.81	1.81

the pDOS for the structures with vacancies, both LSAT and DSO the structures are not insulating anymore (4) the SMO structure on LSAT has become ferrimagnetic, given the starting configuration was antiferromagnetic, which is also in agreement with results from Marthinsen et al. [124] (5) the SMO structure on DSO with higher strain is still AFM in nature but it has two oxygen vacancy and is different in structure comparing to the one on LSAT (6) it is evident that the O $2p$ and Mn $3d$ peaks at ~ 2 eV markedly vary in the two models; they are split in two components for the SMO structures on LSAT (spin-dn) and DSO (total-spin DOS), and they are shifted to lower energies (bottom panels in figure 2.12).

The separated contributions arising from the oxygen atoms surrounding the Mn ion sitting next to the v_o ; from those far away from the v_o . These oxygen atoms are henceforth denoted as close and far, respectively. The Mn-O interatomic distances for all oxygen atoms are tabulated in Table 2.4. In both LSAT and DSO cases, the results show that the formation of v_o results in a decrease in the average Mn–O_{close} interatomic distances. To further see the effect of these two different sets of oxygen atoms (close and far) on the EELS spectra, the calculated EELS spectra are plotted together with the corresponding decomposed O $2p$ states in figure 2.13. Figure 2.13(a) show the results for the less strained SMO structure on LSAT, where 9 O_{close} and 14 O_{far} atoms are present. Focusing on the peak at ~ 2 eV, we note that the DOS of the O

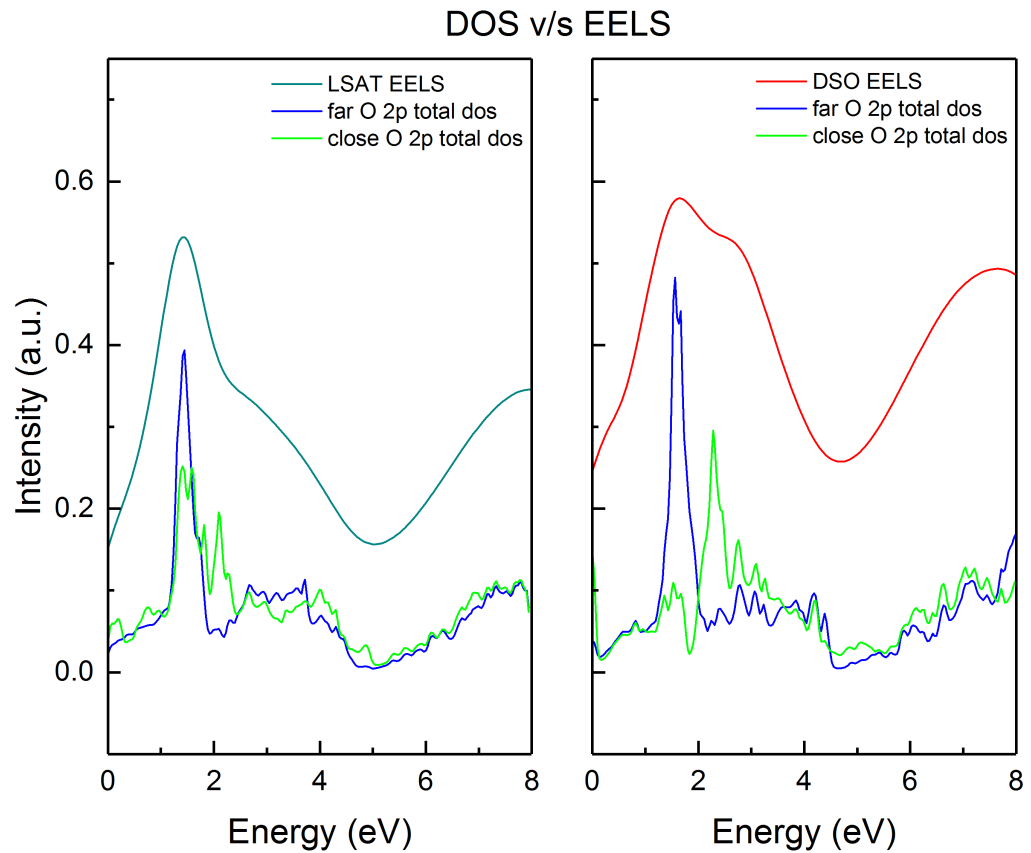


Figure 2.13 – Comparison of the calculated O-K edge EEL spectra with corresponding DOS of the O 2p states decomposed into contributions from the close and far oxygen atoms for SMO on LSAT (left) and on DSO (right).

$2p$ states arising from the O_{close} atoms are peaked at a higher energy. However, the largest contribution to the O $2p$ states arises from the O_{far} atoms and is found at lower energies. The EELS spectrum reflects the relative concentration of O_{far} and O_{close} atoms. Figure 2.13(b) shows the more strained SMO structure on DSO with a larger density of v_o , where 14 O_{close} and 8 O_{far} atoms are present. Also in this case the splitting at ~ 2 eV is evident, but the largest peak is found at higher energies due to the increased concentration of O_{close} atoms. This results in a shift of the O- K_a EELS peak to higher energies. Overall, the net effect in the O- K EELS spectra is that the distance between the O- K_a and O- K_b peaks is reduced due to the presence of vacancies in the SMO structure, in agreement with the experimental EELS data [see figure 2.11(d)].

Lastly, the vacancy formation energy was also calculated based on the study from Aschauer et al. [58]. The v_{O} formation energy was computed by calculating the total energies of the stoichiometric SMO unit cell and the strained supercells containing v_{O} . Compared to the unstrained material, the formation energy of the v_{O} is reduced by 0.24 eV under 3.78% and by 0.09 eV under 1.63% strain.

2.2.7 Conclusion

In this sub-chapter, the structural and electronic properties of epitaxial SMO films deposited on different substrates inducing different strains are investigated. In particular, it has been examined by means of aberration-corrected HAADF-STEM and EELS how the v_{O} density is modified by biaxial strain. The experimental EELS data reveal pronounced peak-height changes and energy shifts as a function of strain, which were previously ascribed to differences in the v_{O} density [113, 122, 125]. The results suggest that the observed energy difference decrease between the O- K_{a} pre-peak and the O- K_{b} main peak with increasing tensile strain is concomitant with an increase of v_{O} concentration. The formation of v_{O} is charge compensated by reducing the formal oxidation state of the Mn cations, as inferred from the changes observed in the Mn- $L_{2,3}$ edges.

These experimental findings are complemented with WIEN2k calculations of the DOS and of the electron energy loss near-edge structure. For this purpose, systematic simulations with different v_{O} concentrations and strains are compared with the EELS experimental results. It is shown that the O- K and Mn- $L_{2,3}$ electron energy-loss near-edge structures are strongly modified by oxygen non-stoichiometry and, to a lesser extent, by strain (only when combined with the presence of v_{O}). Remarkably, the calculations also show that strain solely does not change the intensity nor the distance between the O- K_{a} and O- K_{b} peaks. The net effect in the O- K EELS spectra is that the distance between the O- K_{a} and O- K_{b} peaks is reduced due to the presence of vacancies in the SMO structure. Thus the results presented clarify the origin of the peak-height changes and energy shifts of the O- K and Mn- $L_{2,3}$ edge-fine structures in SMO. It thus follows that the formation of v_{O} in the SMO structure is likely to be enhanced by tensile

2.2. Strain Effects on Point Defects in SrMnO₃

strain. It was also shown that compared to the unstrained material the formation energy of v_{O} is reduced by 0.24 eV under 3.78% tensile strain. Finally, the presence of v_{O} are anticipated which might hinder the potential multiferroic applications of SMO as highly resistive thin films are required.

2.3 Pre-peak in O-K Edge X-ray Spectra of Ni Substituted LaFeO₃

Unlike other chapters in this thesis, this sub-chapter is about simulating X-ray spectra which is very similar to simulating EELS spectra. For details, see section 1.7.2.

2.3.1 Introduction

LaFeO₃ (LFO) shows interesting changes in its physical and chemical properties by cation doping and substitution, and has been applied in advanced technologies such as electronic and magnetic materials[126], solid oxide fuel cells[127], gas sensor[128] and catalysts[129, 130]. It is generally accepted that substitution of the A-site La³⁺ by Sr²⁺ causes changes in the 3*d* electronic configuration, namely oxidation of Fe³⁺ toward Fe⁴⁺ [131], thereby providing a substitution parameter to control the valency of the TM ions. Chainani et al. found that, heterovalent substitution of La³⁺ with Sr²⁺ leads to the formation of hole states near the Fermi level, which has a substantial impact on the electronic transport properties. Due to the formation of doped hole states, the lowest energy charge excitation in the parent insulating oxides of the late transition metal is thus proven to be of the charge-transfer type. There is a wealth of electronic structure studies of La_{1-x}Sr_xFeO₃ ($x=0.0-0.4$) reported in literature with X-ray photoelectron spectroscopy (XPS), ultraviolet photoelectron spectroscopy, bremsstrahlung isochromatic (BI) spectroscopy, and Auger electron spectroscopy[132]. The mechanism of A-site substitution is thus relatively well understood.

In contrast to the aforementioned A-site heterovalent substitution, the effects on valence and conduction band deriving from B-site homovalent substitution is less understood. Sarma et al.[133] investigated heterovalent A-site (La with Sr in LaMnO₃) and homovalent B-site substitution (with Mn, Fe and Co) of LaNiO₃ using X-ray absorption spectroscopy. Through their X-ray absorption measurements they provided some evidence that in the latter case the substitution leads to an empty state redistribution without creation of new holes, whereas no specific explanation about the atomistic origin of the empty state redistribution was given. Since it is of great im-

2.3. Pre-peak in O-K Edge X-ray Spectra of Ni Substituted LaFeO₃

portance to investigate the correlation between electronic structure and electronic conductivity, and the electron-phonon and proton-phonon coupling in cathodes and electrolytes, a systematic study of the hole doping states of La_{1-x}Sr_xFe_{0.75}Ni_{0.25}O_{3-δ} (LSFN) was carried out by synchrotron X-ray spectroscopy and Ligand Field Multiplet Calculations (LFMC) [134–136].

Similarly, in this study the 25% Ni doped LFO is investigated with X-ray and theoretical investigation. The spectroscopic data on homovalent B-site substituted LaFe_{0.75}Ni_{0.25}O₃ (LFNO) shows pre-peak in O-K edge X-ray spectra which is also responsible for the insulator-metal transition. It is not clear from experiments that the origination of this pre-peak is due to the Fe-O or Ni-O bonding. The Fe-L edge is recorded for LFNO and it does not contain the pre-peak feature similar to the O-K edge X-ray spectra. Unfortunately, the Ni-L edge coincides with the La-M edge making it impossible from experiments to conclude anything. With the help of calculations, in particular, by focusing on projected-DOS on specific atomic kinds, and at specific crystallographic sites, it is shown that the closing of the band gap is caused by the appearance of Ni-derived states close to the Fermi level. Then, there is a discussion on the role of Ni in the bonding redistribution of the states close to the Fermi level which explains the origin of the pre-peak observed in the O-K edge both in experiments and calculations.

2.3.2 Experimental Details

LFO and LFNO were synthesized in a strongly distorted orthorhombic symmetry with space group Pbnm (62)[137]. Based on the Rietveld analysis[138, 139] of the X-ray diffractograms, LFO presents orthorhombic symmetry, as well as LFNO (having tolerance factor with Ni³⁺ high (low) spin $t=0.960$ (0.964)), with space group Pbnm (62), - a pseudocubic space group[137]. The unit cell parameters are related to the ideal cubic perovskites as $a \approx ap$, $b \approx ap$, and $c \approx 2ap$. This tilting system is classified as (a+b-b-) according to Glazer's notation[140]. The oxygen NEXAFS spectra of LFO and LFNO are shown in figure 2.14. The spectra originate from the transition of 1s electron into unoccupied O 2p states hybridized with the metal states (in our case Fe and/or

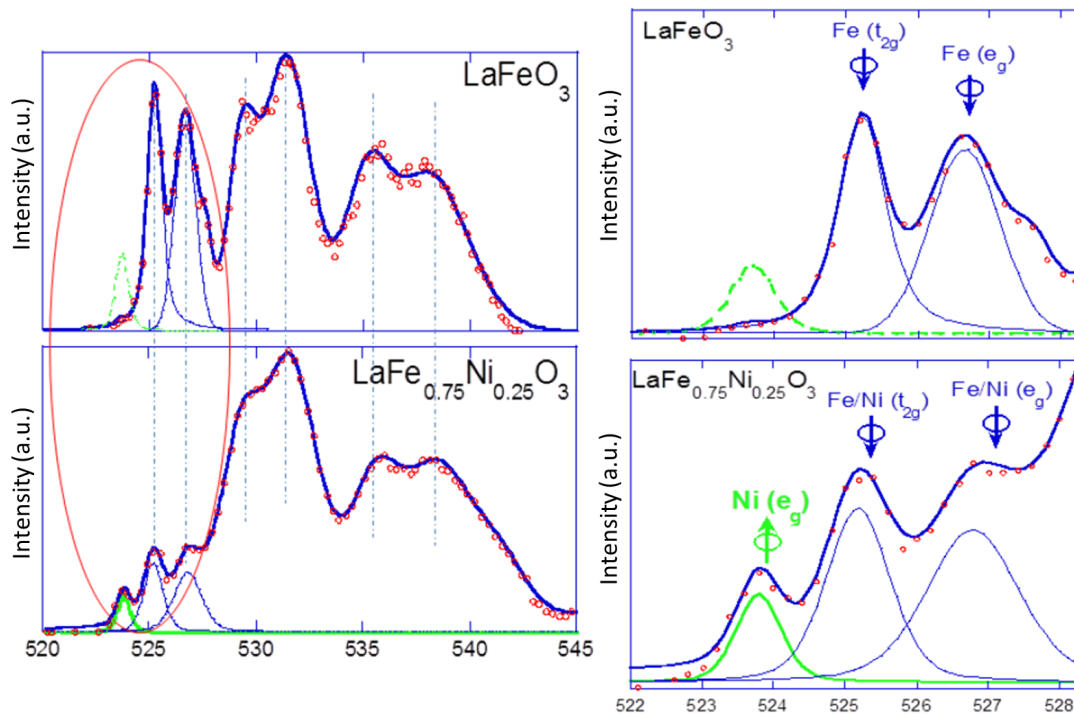


Figure 2.14 – The comparison of the NEXAFS spectra of LFO and LFNO at O-*K* edge for the full energy region (left) and for the pre-edge region (right). The red circles are experimental data and the blue solid line is the fit.

Ni). As it is clear from the figure, the doublet of LFO and a clear pre-peak of LFNO at lower energy region, closer to Fermi energy, are found, which is consistent with previous results[135]. The Fe 3*d* doublet above threshold is ascribed to the minority of Fe 3*d* states bands split by the octahedral crystal field (10 Dq) into threefold *t*_{2*g*} and twofold *e*_{*g*} orbitals. This is consistent with the high spin states *S*=5/2 for Fe³⁺ in these compounds, which will be discussed again in the next section. The energy separation between the doublet peaks in LFO is 1.5 eV, which is in good agreement with the previous result of 1.2 eV with soft X-ray absorption spectroscopy.

The Fe L_{2,3} NEXAFS spectra of LFO and LFNO were supported by Ligand Field Multiplet Calculations (LFMC)[135, 137]. Further information about O-*K* edge NEXAFS spectra of La_{1-*x*}Sr_{*x*}FeO₃, La_{0.5}Sr_{0.5}Fe_{1-*y*}Ta_{*y*}O₃, La_{0.5}Sr_{0.5}Fe_{1-*y*}Ti_{*y*}O₃ can be found in literature[134]. Here, the experiments on LFO/LFNO represent an important part of the PhD work by Selma Erat[135, 137], in the group of Artur Braun (High Performance Ceramics Laboratory) at EMPA, Dübendorf.

2.3.3 Highlights

The main experimental achievements can be summarized as follows:

- The pre-peak in O-*K* edge NEXAFS of LFNO as compared to O-*K* edge X-ray spectra of LFO was observed in experiments.
- The origin of the pre-peak can not be confirmed from experiments because the Ni-*L* edge coincides with the La-*M* edge.

Theoretical achievements:

- Importance of Hubbard corrections to correctly compute the O-*K* edge and Fe/Ni-*L* edge NEXAFS spectra.

2.3.4 Computational Details

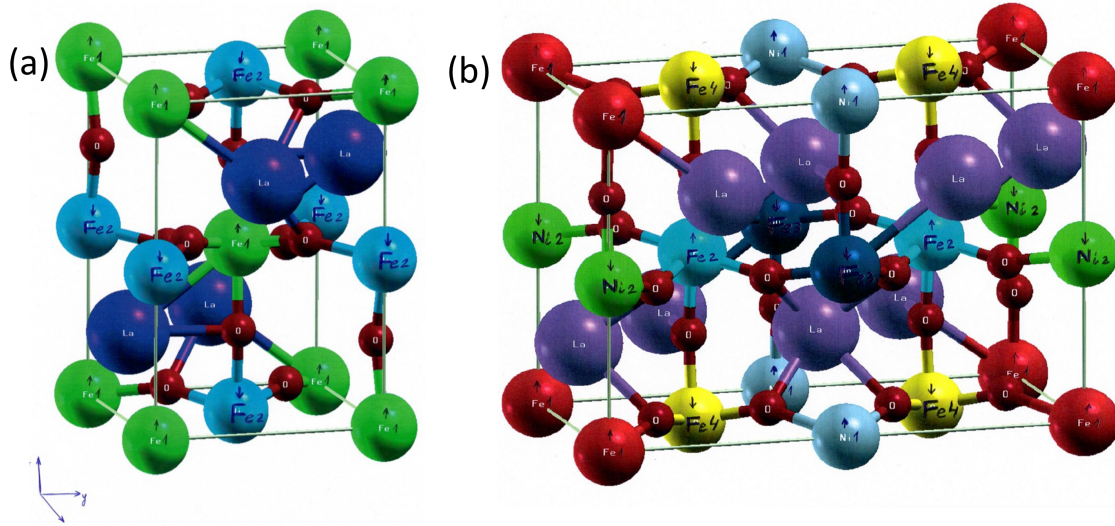


Figure 2.15 – (a) LFO supercell and (b) LFNO supercell representing different Fe atoms with different colors and labels. Courtesy of Iurii Timrov and Matteo Cococcioni.

A supercell with 40 atoms is used (with 8 atoms of Fe for LFO and 2 of them replaced by Ni in case of LFNO; the choice of the substituted sites is somewhat arbitrary; two Fe atoms with opposite magnetization with maximum distance were replaced with Ni atoms) for both LFNO and LFO. Structure of both LFO and LFNO is shown in figure 2.15. The repulsion energy U is determined self-consistently with the help of Quantum ESPRESSO [141] using PBE functional following the protocol of Cococcioni et. al. [142]. Quantum ESPRESSO is an open-source code based on density-functional theory, plane waves, and pseudopotentials for electronic-structure calculations. The calculated U -value for Fe is 4.0 eV. The U -value for Fe and Ni for LFNO are yet to be computed. These values are computed by our collaborators Iurii Timrov and Matteo Cococcioni, at EPFL, using atomic and ortho-atomic orbitals basis set.

2.3.5 Computational Results

Initially, I plan to use FEFF to calculate the NEXAFS spectra for both LFO and LFNO to understand the role of Ni in the origin of pre-peak in LFNO. However, it is very important to assess the effect of Hubbard model corrections before calculating the electronic

2.3. Pre-peak in O-*K* Edge X-ray Spectra of Ni Substituted LaFeO₃

structure and excitation spectra of materials with correlated d- and f-electrons. Since, the Hubbard interactions are not yet implemented in FEFF9.6 I calculated the electronic structure of LFO with PBE and PBE+*U* using WIEN2k and compared it with the one calculated by FEFF. This comparison will be helpful to understand the effect of missing Hubbard interactions in FEFF and how much can it effect the electronic structure of LFO.

The *U*-values calculated by Quantum ESPRESSO were adopted for WIEN2k calculations. Figure 2.16 shows the comparison of pDOS obtained from WIEN2k (with PBE and PBE+*U*) and FEFF. The DOS obtained from WIEN2k with PBE and FEFF do not show any band gap whereas the one obtained with PBE+*U* shows a band-gap of 2.1 eV. The known experimental band-gap for LFO is around 2.4 eV. This comparison shows that Hubbard corrections are needed to correctly interpret the experimentally obtained NEXAFS which are absent in the FEFF simulations.

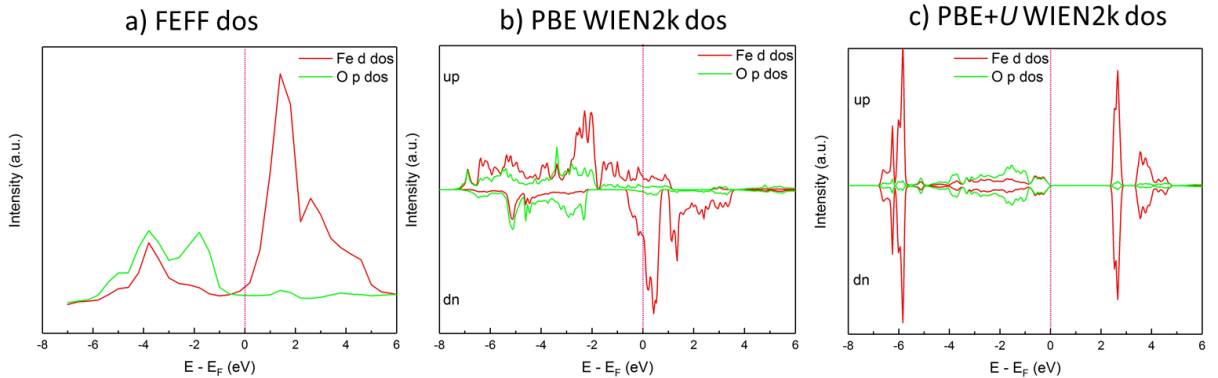


Figure 2.16 – The calculated pDOS obtained from FEFF and WIEN2k using PBE and PBE+*U* for LFO.

2.3.6 Future Perspectives

To address this question correctly the following steps will be performed in the near future:

- The Hubbard *U*-values will be calculated for Ni and Fe in LFNO. These values are being presently calculated by Iuri Timrov and Matteo Cococcioni at EPFL,

Lausanne using an automated procedure based on Quantum ESPRESSO.

- Using these U -values, electronic structure will be calculated for both LFO and LFNO.
- The experimental NEXAFS data can be interpreted by analysing the calculated unoccupied-pDOS to understand the origin of pre-peak in LFNO.
- The bonding states correlated to pre-peak will be further investigated to inquire which atoms are hybridization states are involved. This will indicate whether Ni/Fe are involved directly or indirectly in reorganization of the bonding states around Fermi-level.

2.4 Discussion

In the first two parts of the chapter, I have shown the effect of v_{O} on the bulk properties which are influenced either by strain or by surface reduction. These effects are important in determining the efficiency of a material for particular applications. The combined study of experimental and theoretical EELS was helpful in answering important questions about the presence of the v_{O} and determining their concentration. After validating the concentration and the position of the v_{O} , the models were further investigated to get insights into the electronic structure of the defect system and its effect on the overall bulk properties. In the third section, it was difficult with the experiments to confirm the origin of the pre-peak in LFNO, which is responsible for the insulator-metal transition. With the help of the mentioned future steps, it will be possible to understand the role of the Ni or Fe $3d$ states responsible for the pre-peak in O- K edge X-ray spectra of LFNO.

3 Line Defect: Edge Dislocation

3.1 Structural Configuration of Edge Dislocation Core in BiFeO₃

3.1.1 Introduction

BiFeO₃ (BFO) has been in news for more than a decade now. It is well-known for its multiferroic properties and is considered a potential candidate to replace lead-based piezoelectric materials[143]. BFO is known as ferroelectric and antiferromagnetic with a cycloidal spin arrangement. Among a few room temperature multiferroics, BFO shows the highest ferroelectric polarization with a ferrielectric Curie temperature of 1100 K and an antiferromagnetic Néel temperature of 640 K. However, there have been ample number of studies in order to further improve the multiferroic properties of BFO by chemical modification, using different dopants like La³⁺ [144], Co³⁺ [145], Nd³⁺ [146], Nb⁵⁺ etc[147]. To obtain ferroelectrics with larger polarizations, the current research focuses on perovskites with strongly elongated unit cells. This effect results in charge distribution with large dipolar moments. Using this approach BFO has been grown on different substrates like MgO, LaAlO₃, SrTiO₃ which introduces different level of lattice mismatch[148–150].

Misfit strains introduced by lattice mismatch are compensated by various kinds of defects and dislocations are one of them. Misfit dislocation reduce the mobility of fer-

Chapter 3. Line Defect: Edge Dislocation

roelectric domain walls[151] and are known to hinder the ferroelectric performance of the material. That's why it is important to analyze structural and electronic properties of such crystal defects and further engineer them to improve their efficiency in various devices. In fact, such studies have been made in the past using both experimental and theoretical tools to better understand the effect of these defects on the material properties. Few years ago, unexpected ferromagnetic dislocations were discovered in NiO [65] as described in section 1.11.

Strain engineering of oxide thin films offers a new route to enhance the multiferroic properties of oxide materials. Engineering these defects will be an asset in future for electronic and magnetic devices. There are ample studies on different aspects of strain influence and oxygen vacancies in BFO [152–155]. Two of the common strained phases are the rhombohedral (*R* phase) and the tetragonal (*T* phases) phases. The *R*-phase is the ground state phase with space group *R3c* and the *T*-phase is strained with space group *P4mm*. These phases have been analyzed using EELS and theoretical calculations in various papers[152, 153]. Other than DFT, a classical potential was also developed based on bond valence vector summation (BVVS) conservation principle[71] to deal with full dynamic behavior of BFO. These potentials were used to study the phase transition and temperature dependent cation displacement in BFO. The same potential was initially developed for PbTiO₃[72] and was used to reproduce experimental phase transitions which are driven by temperature and pressure.

In this chapter, a combined study of HAADF-STEM microscopy, EELS and theoretical calculations is used to unfold the structural configuration of dislocation core and its effect on the bulk properties of BFO. In particular, edge dislocation model of BFO has been proposed earlier by Rossell et al. [156] using HAADF imaging/simulations but the possibility of non-stoichiometry in the dislocation core was neglected. Here, the investigation focuses on the structural arrangement and chemical composition of the dislocation core. Molecular dynamics using BVVS potentials was performed to obtain the optimized structural configuration of the dislocation core which was benchmarked by FEFF-calculated EELS.

3.1.2 Experimental Details

BFO was epitaxially grown in (001)_{pc} orientation on a SrRuO₃ buffer layer (a = 0.393 nm, thickness = 35 nm) by pulsed laser deposition. High-pressure reflection high-energy electron diffraction (RHEED) indicated layer-by-layer growth mode followed by step flow growth mode without any island formation. STEM-EDX/EELS measurements were performed using JEOL JEM-ARM200F microscope operated at 200 kV. HAADF and ABF-STEM were performed using a probe semiconvergence angle of 18 mrad and setting the collecting angles ranges to 90 - 170 mrad and 9 - 18 mrad, respectively.

3.1.3 Experimental Results

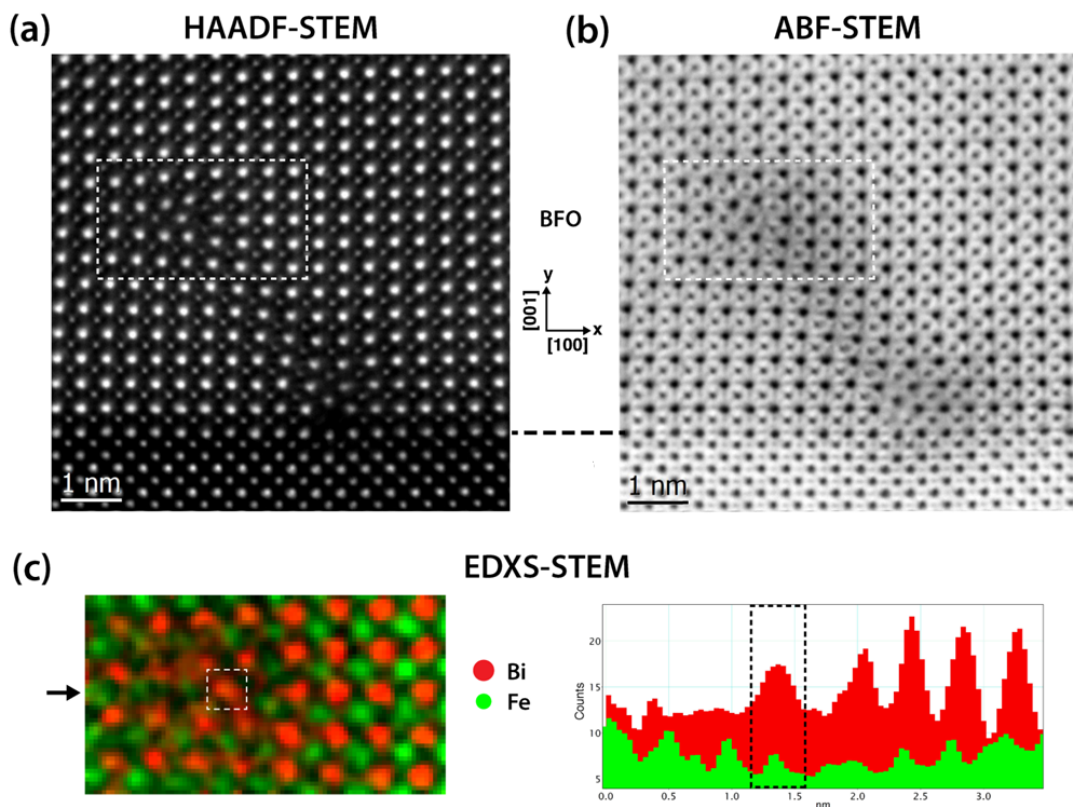


Figure 3.1 – (a) HAADF image and (b) ABF image of an edge dislocation core. (c) EDX map of edge dislocation core structure along dislocation line.

Figure 3.1(a),(b) represent the HAADF-STEM and ABF image of the edge dislocation

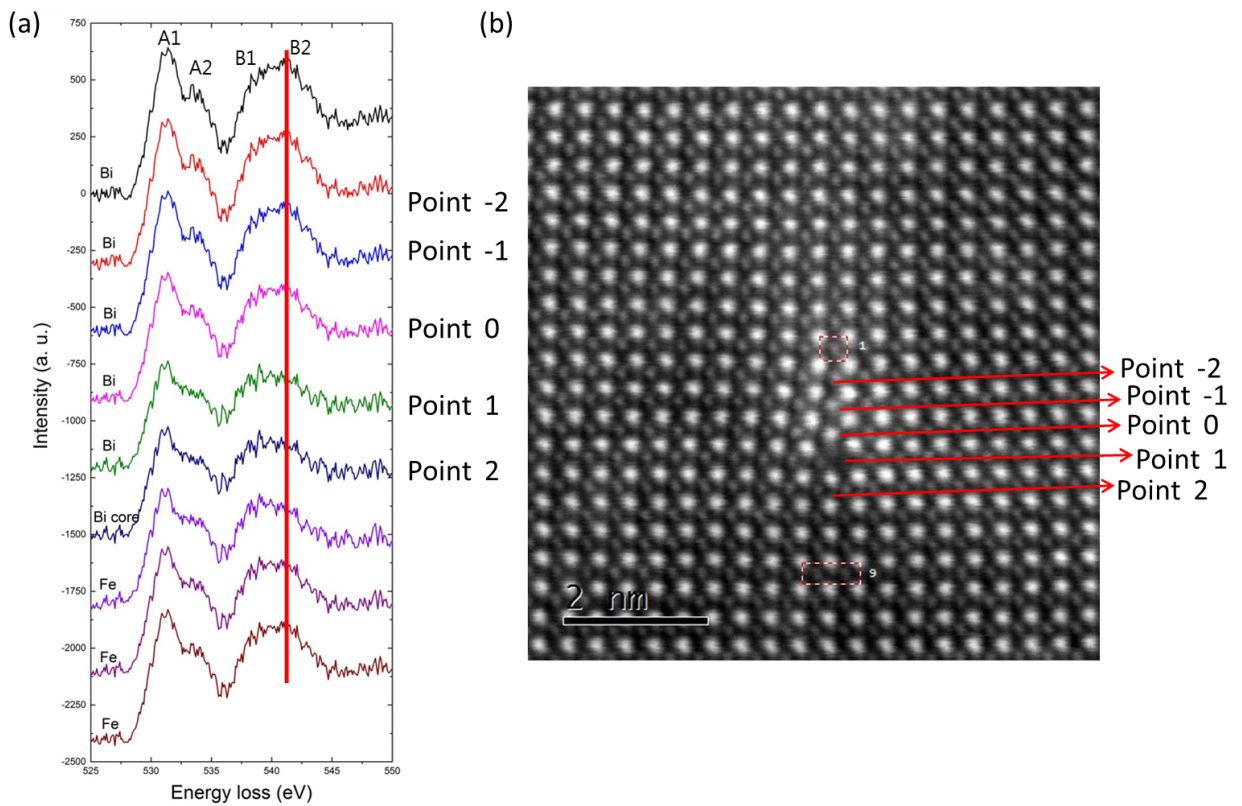


Figure 3.2 – (a) O K-edge EEL spectra recorded point by point starting from the atomic columns along the dislocation line. Points above and below are marked as point -2, point -1, point 0 (core), point 1 and point 2. (b) HAADF-STEM image of the edge dislocation in a BFO thin film.

core in BFO. Figure 3.1(c) shows the EDX elemental map along the dislocation line. EDX map at dislocation core confirms the presence of both Bi and Fe atoms in the core. Figure 3.2 shows the experimentally recorded O-K edge EEL spectra of all the points above and below dislocation core including the dislocation core. Following features are observed from the experimental O-K edge EEL spectra:

1. away from the core (point -2) there is a clear splitting in both the peaks A and B representing A1, A2 and B1, B2 respectively.
2. closer to the dislocation core (point -1, point 0 (core) and point 1), intensity B1:B2 decreases

3.1. Structural Configuration of Edge Dislocation Core in BiFeO₃

3. ratio B1:B2 increases for the points (point 2) below the core.

These spectral features are crucial in benchmarking the theoretical dislocation core model by carefully comparing the calculated-EELS with the experiments.

3.1.4 Highlights

The main experimental achievements can be summarized as follows:

- The BFO films were grown by Pu Yu at Tsinghua University and the experimental measurements were carried out by Marta Rossell.
- EDX measurements confirms the presence of both Fe and Bi in the core.
- The experimental O-*K* edge EELS shows specific features for oxygen atoms present away from the core and at the core.

Theoretical achievements:

- An optimized model of dislocation core is obtained by using classical molecular dynamics with LAMMPS, validated with HAADF-STEM image simulations.
- To benchmark the optimized dislocation core model, FEFF-calculated O *K*-edge EELS for models with different concentrations of Fe/Bi in the dislocation core were compared with experimental EELS.

3.1.5 Computational Details and Results

Firstly, I will discuss about the modeling of the dislocation core structure. To simulate the dislocation core structure, 7-8 extra layers were required both in x and y direction to avoid the artificial interactions between the dislocation core and its periodic images. Further, to study the effect of the presence of Fe atoms in the core on the dislocation core structure and EELS, large number of supercells were also required in the z-direction as well. Taking all this into consideration, a huge supercell with thousands of atoms was required for simulation. WIEN2k or other DFT codes were not the obvious choice to deal with this particular problem. So, in the next section, I discuss about how I used the P-N model and molecular dynamics to obtain the optimized structural configuration of the dislocation core structure. Later, I discuss the implementation of real-space FEFF code to calculate O-K edge EELS for the optimized dislocation core structures.

P-N model

In this section, I will briefly talk about building the edge-dislocation core model using P-N model. Although the output configurations from this method were not used for further investigation (see below), this procedure has been a useful exercise to get acquainted with the connection between a continuum and an atomistic level of description. Firstly, to obtain the shear distribution function $S(x)$ for BFO, GSF energies are calculated, as mentioned in eq. 1.42. DFT calculations were performed to calculate GSF energies, using the Gaussian-plane wave (GPW) method as implemented in CP2K package [20] with DZVP basis sets for the representation of Kohn-Sham orbitals, with the plane-wave cut-off for the charge density of 600 Ry. A $4 \times 4 \times 4$ supercell (figure 3.3) is used with 10 Å vacuum added in the direction normal to the slip plane [100] to avoid interaction between repeated stacking faults.

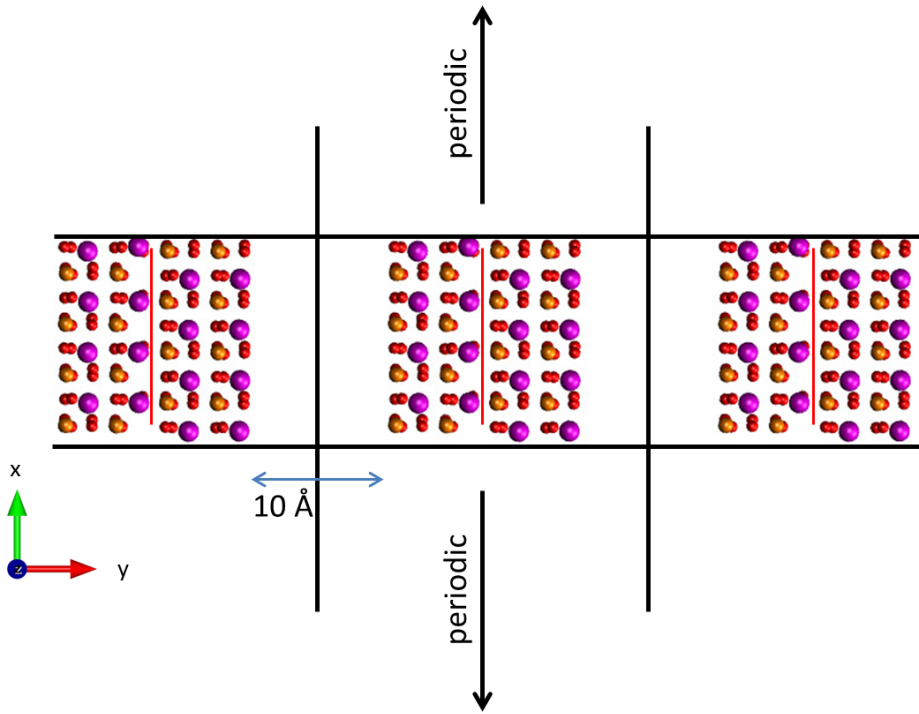


Figure 3.3 – Structure model used for GSF energy calculation with slip-plane represented in red line and with 10 Å vacuum perpendicular to the slip plane.

P-N Model Results

Figure 3.4(a) shows the GSF energies plot against the shear distribution $S(x)$. Using this plot the restoring force is calculated to solve the P-N equation (eq. 1.41). Figure 3.4(b) shows the restoring force against stacking fault w.r.t to $S(x)$. The shear distribution is given by:

$$S(x) = \frac{b}{2} + \frac{b}{\pi} \sum_{i=1}^N \alpha_i \arctan \frac{x - x_i}{c_i} \quad (3.1)$$

Substituting the $S(x)$ into the left-hand side of the P-N equation, gives the restoring force:

$$F^{PN} = \frac{Kb}{2\pi} \sum_{i=1}^N \alpha_i \frac{x - x_i}{(x - x_i)^2 + c_i^2} \quad (3.2)$$

3.1. Structural Configuration of Edge Dislocation Core in BiFeO₃

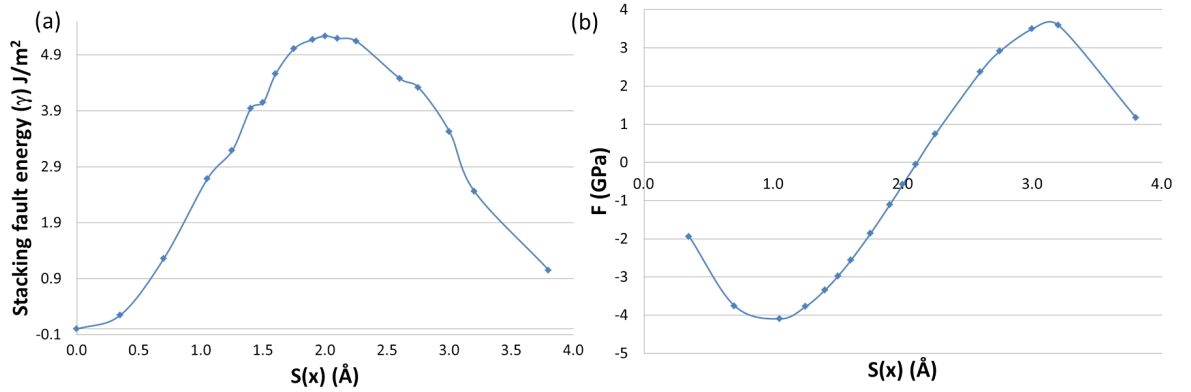


Figure 3.4 – (a) plot showing values of GSF energy w.r.t $S(x)$ and (b) shows the variation of restoring force (F) w.r.t to $S(x)$.

The variational constants were obtained from the least square minimisation of the difference between F^{PN} and the restoring force was calculated from ab-initio calculations. Using these values, the shear distribution was calculated for the atoms in the slip plane. Figure 3.5(a) shows the model obtained after applying the shear distribution to the bulk structure. Then, the elastic displacements due to the shear stress were calculated for all the atoms close and far away from dislocation core using eq. 1.43 and 1.44. Figure 3.5(b) shows the dislocation core model of BFO using the P-N model. Geometrically, the arrangement of Bi atoms around the dislocation core in

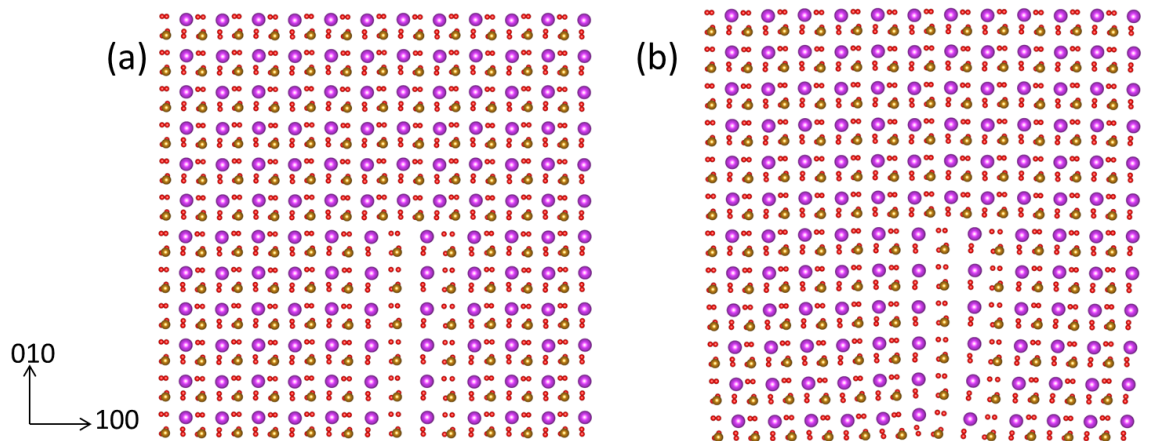


Figure 3.5 – (a) model obtain after applying shear distribution $S(x)$. (b) final model obtained after applying elastic strain to the shear strained model.

the final model (figure 3.5(b)) does not look very close to the one in the experimental

Chapter 3. Line Defect: Edge Dislocation

HAADF-STEM images. Although, in this exercise lot of improvements can still be applied in terms of calculating GSF energies for other slip planes and minimizing the variational constants. I did not further investigated about the model obtained from this strategy and I chose to use molecular dynamics as a tool to optimize the dislocation core structure. Now, I talk about modeling dislocation core with the help of molecular dynamics using BVVS potentials.

Molecular Dynamics: BVVS Potentials

Before discussing the initial configuration model for ab-initio simulations, I briefly mention about the BVVS potentials which were used to simulate the edge dislocation in BFO. These potentials are based on bond valence and bond-valence vector conservation principle. This principle states that each atom i prefers to have the total bond-valence of its bonds to its atomic valence, defined by $V_{0,i}$. The actual atomic valence V_i for atom i can be calculated by summing over the individual bond valences V_{ij} for bonds between the atom and its nearest neighbors. The bond-valence can be defined as,

$$V_{ij} = \left(\frac{r_{0,ij}}{r_{ij}} \right)^{C_{ij}} \quad (3.3)$$

where r_{ij} and C_{ij} are Brown's empirical parameters and are readily available for many atomic pairs[157]. The total interatomic potential for BFO is given by summation of Coulomb energy, short-range repulsive Lennard-Jonnes energy, the bond-valence energy and the bond-valence vector energy. Further details on these potentials can be found in ref[158].

Molecular Dynamics: Starting Configuration for the Edge Dislocation

The initial bulk configuration was built using the experimental lattice parameters of R-BFO[152] with a $24 \times 24 \times 12$ supercell. In order to generate the edge dislocation with dislocation line along the $\langle 001 \rangle$ direction, two strategies were tried. Firstly, the

3.1. Structural Configuration of Edge Dislocation Core in BiFeO₃

bulk configuration were divided into two halves and a 2D slice of (12 × 12) unit cell was deleted from lower half of the model. But, this created two asymmetric dislocation core after structural optimization. This strategy proved to be unsuccessful as the dislocation core were not symmetric on both the ends.

In the second strategy, a 2D slice of (12 × 12) unit cell is deleted from the central region of the model (figure 3.6(a)). The remaining 23 layers of unit cells are distributed uniformly across the space (figure 3.6(b)). This created two symmetric dislocation core structures separated by 12 unit cells. Two manual modifications were made to this model using the findings from the Lubk et al.[156]. Firstly the Fe atoms in the core were replaced by Bi atom and a column of O atom in the core was deleted completely (figure 3.7). To confirm the findings from the experiments, three models

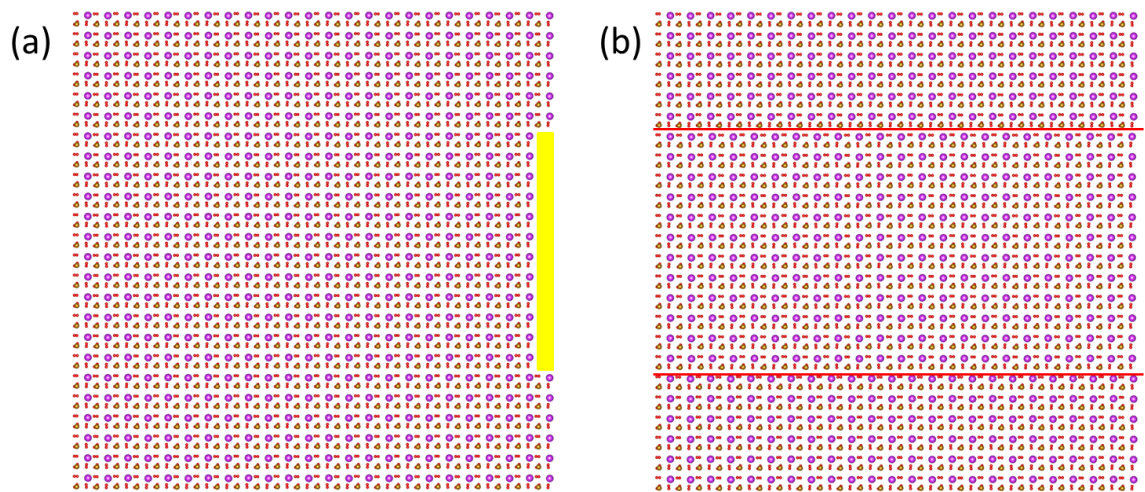


Figure 3.6 – (a) Model with 23 layers in the middle and the yellow box highlight the profile of the deleted slice. (b) Model obtained after distributing uniformly rest of 23 layers.

were prepared with different concentration of Fe atoms in the core. Following are the three models,

1. Model 1: Dislocation model with Bi atom in the each core.
2. Model 2: Dislocation model with $\frac{1}{3}$ Bi atom and $\frac{2}{3}$ Fe atom in the core.

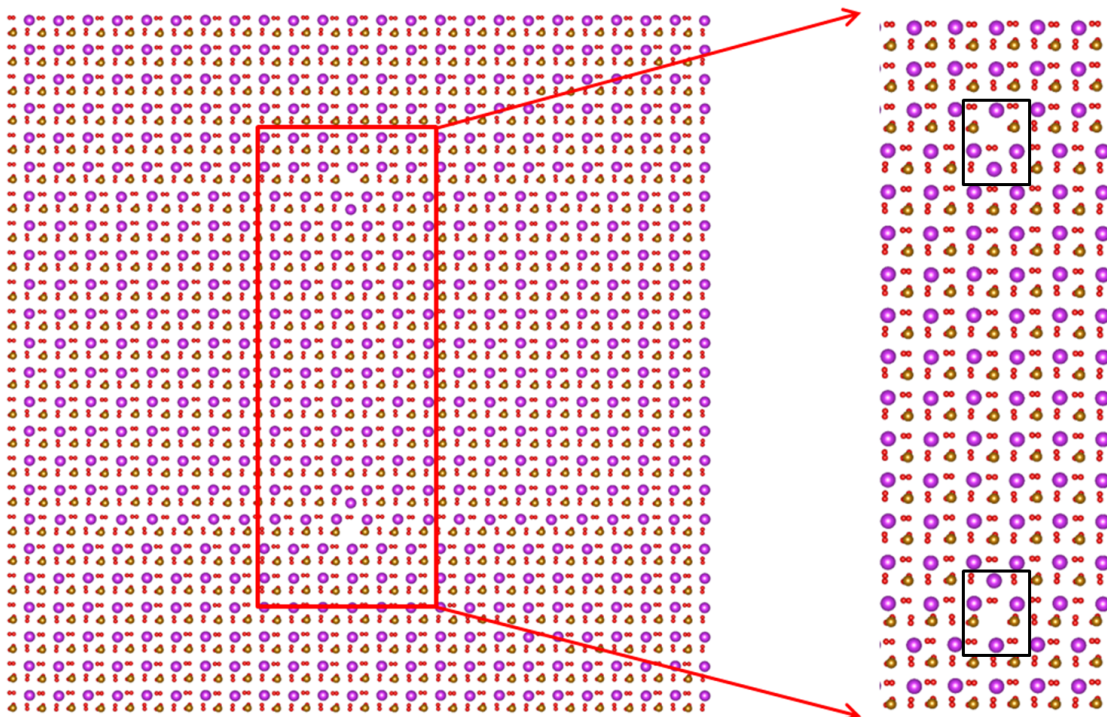


Figure 3.7 – Final model of starting configuration obtained after implementing the suggested modification[156] to the core structure. The core structure of dislocation is marked in black box where the oxygen removal and Fe/Bi substitutions as described in the text were implemented.

3. Model 3: Dislocation model with $\frac{2}{3}$ Bi atom and $\frac{1}{3}$ Fe atom in the core.

All these changes were made manually by simply replacing the Bi atoms with Fe atoms in the core.

Molecular Dynamics Details

The BVVS potentials are implemented in the classical molecular dynamics code called LAMMPS[159, 160]. It contains potentials for solid state materials and soft matter and coarse-grained mesoscopic systems. All calculations in this section were performed using this code. Firstly, the simulated annealing global optimization method was used to optimize the bulk lattice parameters. Optimized lattice parameters are $a = b = c = 3.882 \text{ \AA}$ which are underestimated by 2% with respect to experimental parameters.

3.1. Structural Configuration of Edge Dislocation Core in BiFeO₃

These optimized parameters were used in the calculations for all the models. Structural optimization of the dislocation core structure was performed in the following way: a) gradually increase the temperature from 0 K to 300 K and b) equilibrate the system at 300 K. The final configuration was obtained by averaging structures from various frames acquired at 300 K.

Molecular Dynamics: Results

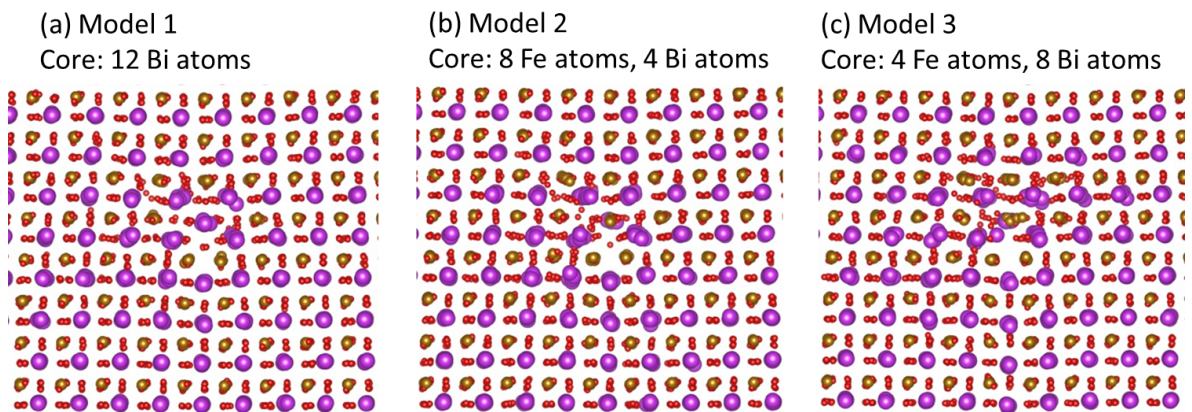


Figure 3.8 – Optimized configuration of all the three models obtained after molecular dynamics simulation.

The optimized structures for model 1, model 2 and model 3 are shown in figure 3.8(a),(b) and (c), respectively. They all are similar to each other in terms of the geometry of the dislocation core structure. To further benchmark these structures with the available experimental HAADF images, HAADF-STEM simulations were performed for each model.

3.1.6 HAADF Image Simulations

HAADF-STEM Simulation where performed using STEM_CELL software, based on Kirkland code for TEM image simulations [161]. The simulation were performed by Dr. Marco Campanini using the multislice algorithm, taking into account the thermal diffuse scattering by means of the frozen phonons approximation. In order to

Chapter 3. Line Defect: Edge Dislocation

estimate the thickness of the sample, a thickness series (thickness range: 0-46 nm) was performed on bulk BFO comparing the intensity ratio $\frac{I_{\text{Bi}}}{I_{\text{Fe}}}$ with experimental data obtained in regions far from the dislocations, where the dislocation strain fields are negligible. The estimated thickness was 33 nm. For all the considered models, the simulations were performed computing the average of 10 frozen phonon configurations, using constant Debye-Waller factors for all the atomic species. Figure 3.9(a) shows

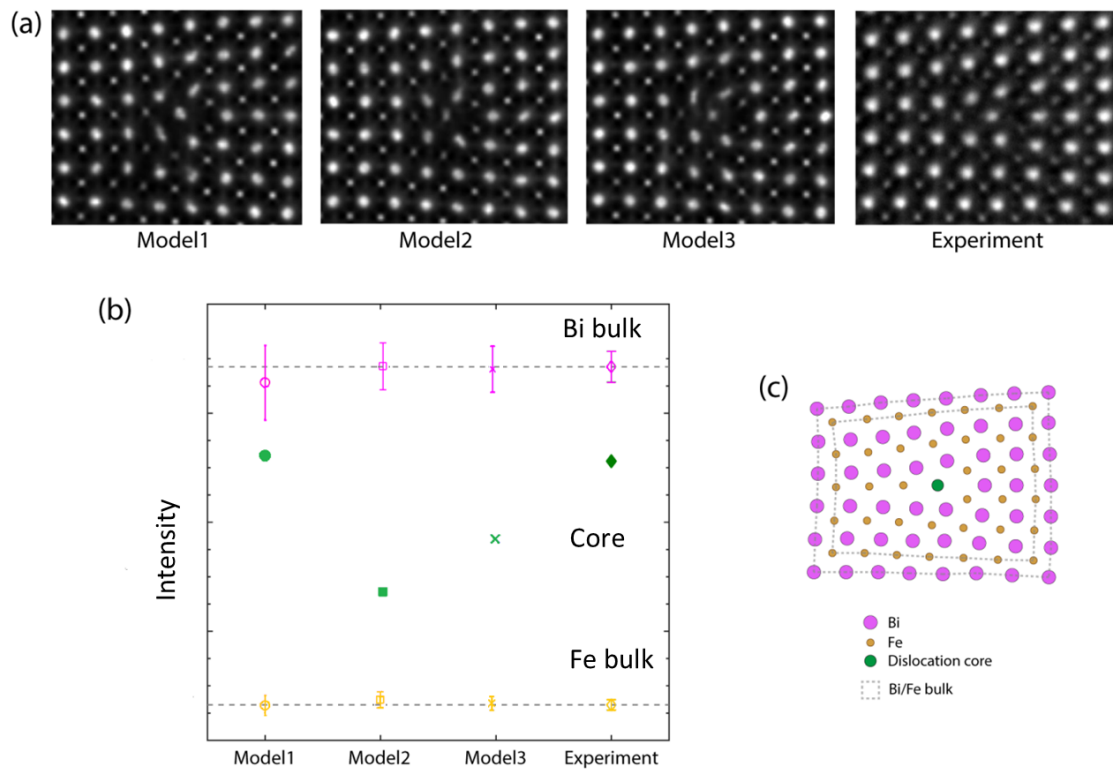


Figure 3.9 – a) Comparison between simulated HAADF-STEM images for the three different structural models and the experimental data. b) Average HAADF Intensities for simulated images and experimental data, calculated following the scheme given in c). The Bi bulk are in blue, Fe bulk in yellow and core in green.

the comparison of simulated HAADF-STEM images for the three models with the experimental data. The local change in the experimental images contrast highlights a strain field associated to the coupled dislocations. Figure 3.9(b) summarizes the average HAADF intensities for simulated images and experimental data. In particular, the Fe-bulk and Bi-bulk values were respectively obtained averaging the intensities of

3.1. Structural Configuration of Edge Dislocation Core in BiFeO₃

Bi and Fe columns along the dashed gray lines, shown in figure 3.9(c). The plot shows that the simulated intensities far from the dislocation (where the HAADF intensity is least affected by strain effects) are in good agreement with the experimental ones. The value obtained for the core is closer to experiment for the model 1, where the core itself is only made up by Bi atoms. Nevertheless, due to the complexity of the strain fields for the investigated system showing coupled dislocations, it is not possible to select the right structural model from the sole comparison of simulated and experimental HAADF-STEM images. Note that the intensity at the core is closer to the results of model 1 and model 3, so we resort to a further analysis to obtain a further hint on the correct core structure.

That's why further validation was done by calculating O-*K* edge EELS of O atoms around the dislocation core for each model and compared with the experimental EELS. For calculations, two points above the core, two points below the core and core itself were considered for comparison with the experiments. These points are: point -2, point -1, point 0 (core), point 1 and point 2.

3.1.7 EELS Calculated with FEFF

The optimized structure of the dislocation core obtained from molecular dynamics was used for further calculation of EELS. Real space multiple scattering code FEFF 9.0[162] is used for calculation of O-*K* edge EELS for the different points above and below dislocation core, see section 1.7 for the description of FEFF program. Each point represents the contribution from all the neighbors around the atom in the corresponding atomic column. The potentials were calculated self-consistently over the radius of 5.1 - 5.3 Å using Hedin-Lundqvist (local density approximation) self-energy. For the full multiple-scattering (FMS) calculations, the calculations converged for clusters as small as 260 atoms. The spectra and density-of-state calculations presented here were all modeled for 330 atoms in the FMS cluster. The O-*K* edge spectra of oxygen atoms surrounding Fe atom were calculated separately for each atom and the spectra for each point was obtained by averaging the contribution from all oxygen atoms. All EELS spectra were simulated with core-hole.

FEFF analysis

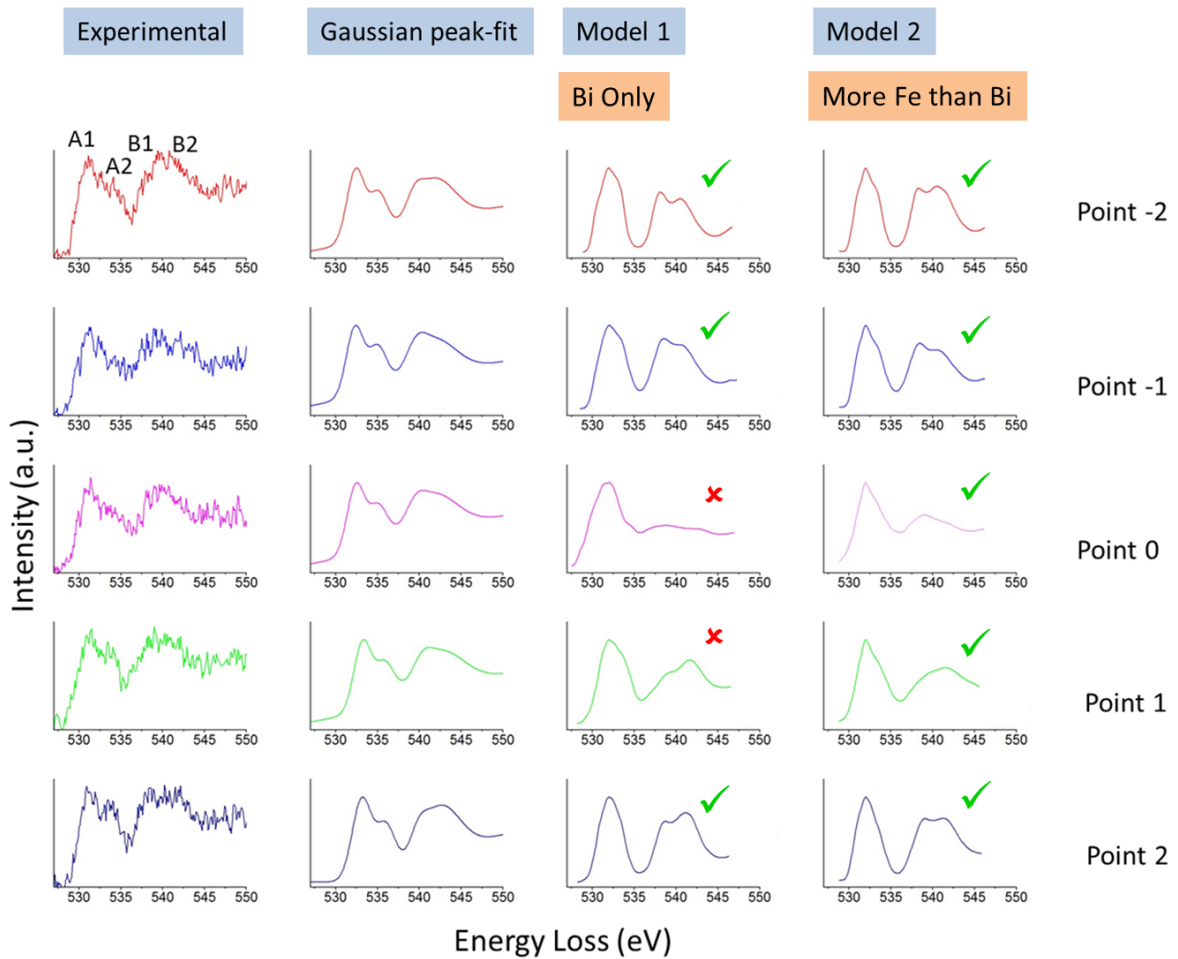


Figure 3.10 – Comparing calculated O-K edge EELS for model 1 and model 2 with experimentally recorded O-K edge EELS. For better comparison, the Gaussian-peak fit is used to represent the original experimental data. Based on matching the B1:B2 intensity ratio with experiments each point in model 1 and model 2 is given a tick mark (green) or a cross-sign (red).

Figure 3.10 shows the comparison of model 1 and model 2 with Gaussian peak-fit experimental data. The calculated EELS for the model 1 and model 2 compares relatively well with experiments for points above and below the core. On the basis of intensity ratio (B1:B2) match with the experiments, each point in the model is given a tick-mark (green) if it matches and a cross sign (red) if it doesn't. In case of model 1, the O-K EELS at the core has very small B1 and B2 peaks and are also shifted to lower energy as compared to the experiments. But for model 2 the B1 and

3.1. Structural Configuration of Edge Dislocation Core in BiFeO₃

B2 peaks are slightly higher in intensity as compared to model 1. This indicates that the incorporation of Fe atoms in the core increase the unoccupied density of states at 10 eV from the edge of the spectra. For further analysis, the energy difference between the peak B1 and A1 were calculated for the experiments and for the calculated model 1 and model 2 and are summarized in figure 3.11. For experimental data, the E_{diff} (where $E_{\text{diff}} = E_{\text{B1}} - E_{\text{A1}}$) is around 7.5-8.0 eV for all the points. For the calculated-EELS the E_{diff} values are underestimated by 1.5 eV for both the models. For both model 1 and model 2, the E_{diff} value of the core is either 1 eV smaller or 1 eV larger than the E_{diff} value of the core for experiments, respectively.

Till now, the O-K edge EELS for model 3 is calculated for only O atoms present in the

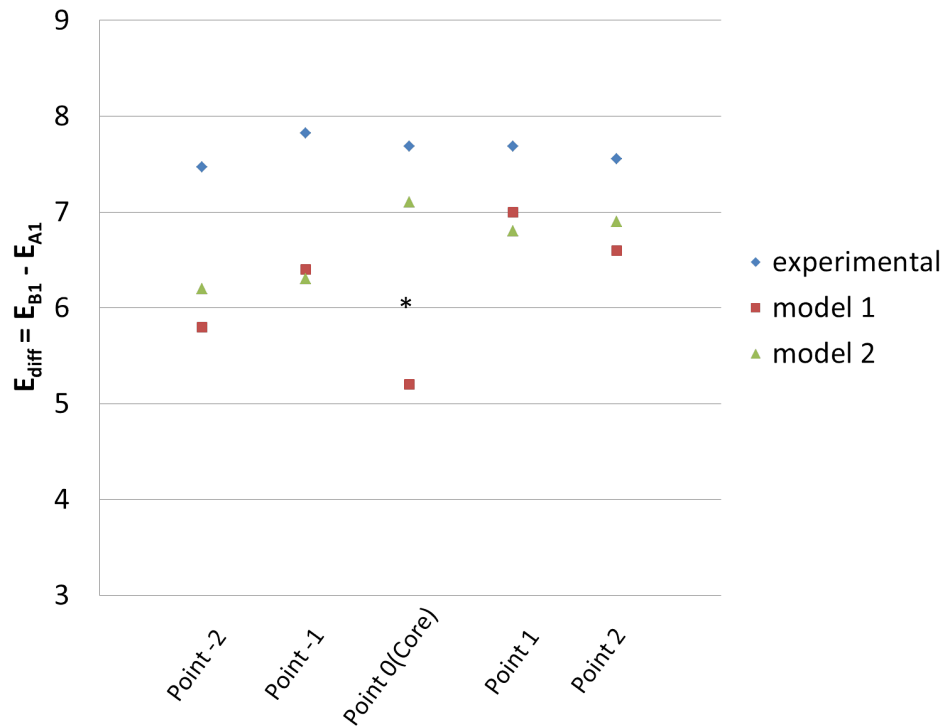


Figure 3.11 – Values of E_{diff} for model 1, model 2 and experimentally recorded O-K edge EELS spectra. The asterisk (*) shows the E_{diff} for the O-K edge EELS obtained from the core of the model 3.

core. The E_{diff} corresponding to this core is labeled as * in the figure 3.11. This values lies close to the E_{diff} value of point 1 in model 1 and model 2. Although, the O-K edge EELS for other points in the model 3 are yet to be calculated. This indicates that the

Chapter 3. Line Defect: Edge Dislocation

concentration of Fe atoms is also important to accurately determine the dislocation core structure. The results of these section seem indeed to indicate a better agreement with experiment in the case of model 2.

3.1.8 Conclusions

The combined approach of HAADF-STEM, EDX, reveals the presence of non-stoichiometry in the dislocation core. Though, there is some work remaining from simulation point of view to come to a final conclusion. The HAADF analysis seems to indicate that Bi should be present in the dislocation core, with or without Fe atoms. The EELS conversely give an indication of an admixture of Bi and Fe, or pure Fe.

But the FEFF calculated EELS for model 1 (core consisting of Bi) was not the best match with the experimental EELS. It was seen that the calculated EELS for Fe atoms (model 3) in the core were closer with the experiments as compared to model 1 or model 2. The HAADF-STEM simulations also suggests that the core is mostly composed of Bi atoms. Further investigation are required to approximately quantify the concentration of the Fe atoms and also to understand their arrangement in the structure of the core.

The non-stoichiometry of Fe atom in the core further supports the idea of these dislocation cores to be magnetic. The first experiments from electron holography hints these cores to be magnetic. Though there are more experiments planned in near future to verify these results. Another experiment planned is to perform magnetic force microscopy on this sample to get more insights into these dislocation cores and also to understand the origin of possible magnetism.

4 Planar Defects: Stacking Faults

4.1 Modeling Interacting Stacking Faults Resulting in Stair-rod Dislocations in GaAs Nanowires

In this chapter, I will describe modeling of interacting stacking faults in GaAs nanowires as one of the examples of planar defects. Most of the part of this chapter has been extracted with slight modifications from Bologna et al.[163], under review by Physical Review Letters. The GaAs nanowires were grown by Moritz Knödler and were characterized by Nicolas Bologna at IBM, Rüschlikon, Zurich. I would also like to thank Marta Rossell, Marco Campanini, Rolf Erni and Daniele Passerone for their contribution and great effort.

4.1.1 Introduction

III-V semiconductor nanowires (NWs) are low dimensional structures receiving increasing interest from the research community due to their superior physical properties. Compared to silicon, a higher electron mobility combined with the possibility of band gap engineering makes these materials particularly suited for electronic and optoelectronic devices [164–167]. Furthermore, due to their high aspect-ratio, nanowires are attractive building blocks to be integrated on Si for a broad range of applications, such as photovoltaic devices, field effect transistors and lasers [168–170]. However,

Chapter 4. Planar Defects: Stacking Faults

besides the novel device architecture possibilities [171, 172], what makes nanowires superior to their thin-film counterparts is that below a certain critical nanowire diameter the density of misfit dislocations can be significantly reduced, allowing improved growth efficiencies and better device performances [173–175]. In this context, the presence of bulk crystallographic defects (i.e. partial dislocations, stacking faults, etc.) might play a decisive role on the device properties.

In this work, aberration-corrected scanning transmission electron microscopy (STEM) and energy dispersive x-ray (EDX) spectroscopy were used to characterize two stair-rod dislocation cores formed at the intersection of three v-shaped intrinsic stacking faults (ISFs) in a horizontally grown gallium arsenide (GaAs) nanowire. Based on the experimental observations, a 3D atomic model was developed and used to perform DFT calculations. The simulations reveal the presence of quasi- sp^2 hybrid orbitals at the two defect cores and the presence of highly localized DOS shifting along the stacking fault from the valence band in the gallium core to the conduction band in the arsenic core. This confirms the antithetical nature of these two types of defects suggesting for this particular case of the formation of parallel preferential paths for both electrons and holes along the nanowire.

4.1.2 Experimental Details

GaAs horizontal NWs were grown via template assisted selective epitaxy (TASE) in a metal organic chemical vapor deposition (MOCVD) tool for 60 min at 550°C as reported previously [36]. The JEOL JEM-ARM200F microscope operated at 200 kV was employed for EDX analysis. In STEM mode, a convergence semiangle of 25 mrad was used in combination with a high angle annular dark field (HAADF) detector with inner and outer collection semiangles of 90 and 370 mrad, respectively.

4.1. Modeling Interacting Stacking Faults Resulting in Stair-rod Dislocations in GaAs Nanowires

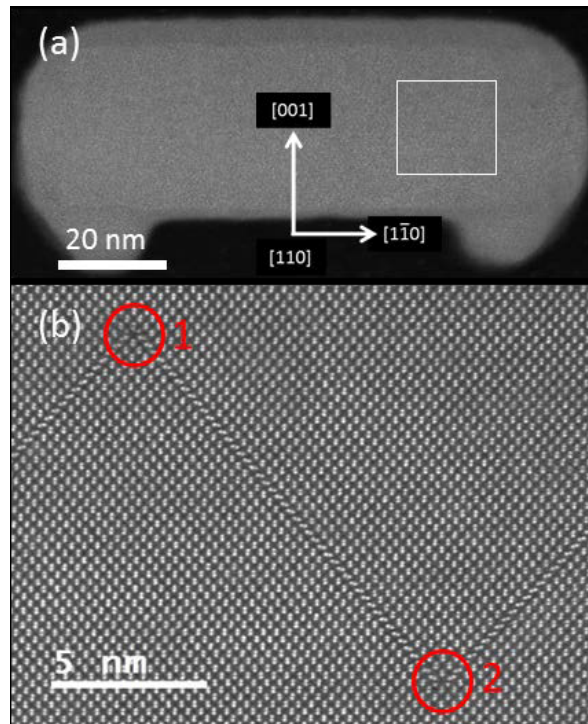


Figure 4.1 – HAADF-STEM micrographs, recorded along the $[110]$ zone axis, showing (a) the front section of the nanowire and (b) an enlarged view of the square indicated in panel (a). The intrinsic stacking faults intersecting at 70.5° are visible as v-shaped planar defects. The stair-rod dislocations at the vertexes are highlighted with red circles. The two cores are ~ 15 nm apart. This figure is adapted from ref[163].

4.1.3 Experimental Results

Figure 4.1(a) shows a low magnification HAADF-STEM micrograph of a GaAs nanowire front section projected along the $[110]$ zone axis. This front section exhibits an average width and height of 100 nm and 38 nm, respectively. Unless otherwise specified, the same orientation and zone axis of the nanowire is maintained for all subsequent micrographs and models. An atomically resolved image of the inset marked with a white square in figure 4.1(a) is displayed in figure 4.1(b). Three intrinsic stacking faults on different 111 glide planes intersect at an acute angle of 70.5° and create the dislocation cores highlighted with two red circles labeled 1 and 2. These two cores, connected via an intrinsic stacking fault, are about 15 nm apart and are expected to propagate along the whole length of the nanowire. The dumbbell atomic columns in the intrinsic stacking faults exhibit the typical change in orientation due to the

Chapter 4. Planar Defects: Stacking Faults

removal of one close-packed plane from the perfect zinc blende crystal structure. The

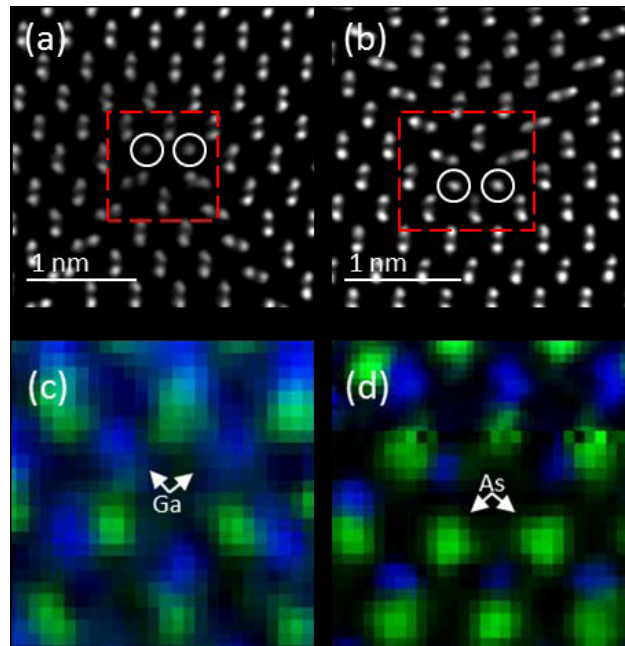


Figure 4.2 – HAADF-STEM micrographs, recorded along the [110] zone axis, showing (a) the front section of the nanowire and (b) an enlarged view of the square indicated in panel (a). The intrinsic stacking faults intersecting at 70.5° are visible as v-shaped planar defects. The stair-rod dislocations at the vertexes are highlighted with red circles. The two cores are ~ 15 nm apart. This figure is adapted from ref[163].

cores are formed by the interaction of 30° Shockley partial dislocations annihilating each other in two different stair-rod dislocations. These types of stair-rod dislocations, also called Lomer-Cottrell locks, are characterized by the presence of single unpaired atomic columns [32], clearly visible in figure 4.2(a) and (b) where the two dislocation cores, previously marked as 1 and 2, are illustrated at higher magnification. The mirrored symmetry between the two structures with the unpaired atomic columns (marked with white circles) is distinctly visible on different lattice sites.

Due to the small atomic number difference between Ga ($Z=31$) and As ($Z=33$), the Z^2 contrast intensity difference, usually used to recognize atomic species in HAADF micrographs, was not significant enough to safely determine the nature of the single elements. For this reason, atomic-scale EDX chemical maps were recorded in the red dashed area of the two cores. As illustrated in figure 4.2(c), the core in panel (a) exhibits Ga single atomic columns while, in figure 4.2(d), the core corresponding to

4.1. Modeling Interacting Stacking Faults Resulting in Stair-rod Dislocations in GaAs Nanowires

panel (b) consists of As single atomic columns, where gallium and arsenic atoms are colored in blue and green, respectively.

4.1.4 Highlights

The main experimental achievements can be summarized as follows:

- The GaAs nanowires were grown by Moritz Knödler and all the experimental measurements were done by Nicolas Bologna at IBM, Rüschlikon.
- HAADF-STEM micrographs recorded intrinsic stacking faults forming a stair-rod dislocation with single atomic columns in the core.
- EDX measurements confirms the presence of single As- and Ga-columns in the dislocation core connected by a stacking fault line.

Theoretical achievements:

- Using a range-separated hybrid functional, special basis sets and techniques implemented in CP2k were used to simulate a 1000+ atom system; a reduction of the band gap compared to the bulk structure was observed.
- Variations in the projected-DOS along the stacking fault line and difference in electronic structure of the two cores were investigated.
- Upon calculating electron density-maps and electrostatic potential along the stacking fault line joining the two dislocation cores, the presence of an electric dipole between them was demonstrated as a promising feature for future applications.

4.1.5 Building the Stair-rod Dislocation Model and Computational Details

3D atomic models of the dislocation cores were created with the Rhodius software [176, 177]. This software allows to cut the bulk sample in different planes and then combine them at a given orientation and distance. Figure 4.3(a) shows the different cut planes which were joined to form the stair-rod dislocation model. Figure 4.3(b) shows the final model obtained from Rhodius with single atom dislocation cores marked with red circles. This model was used as input for the DFT calculations in

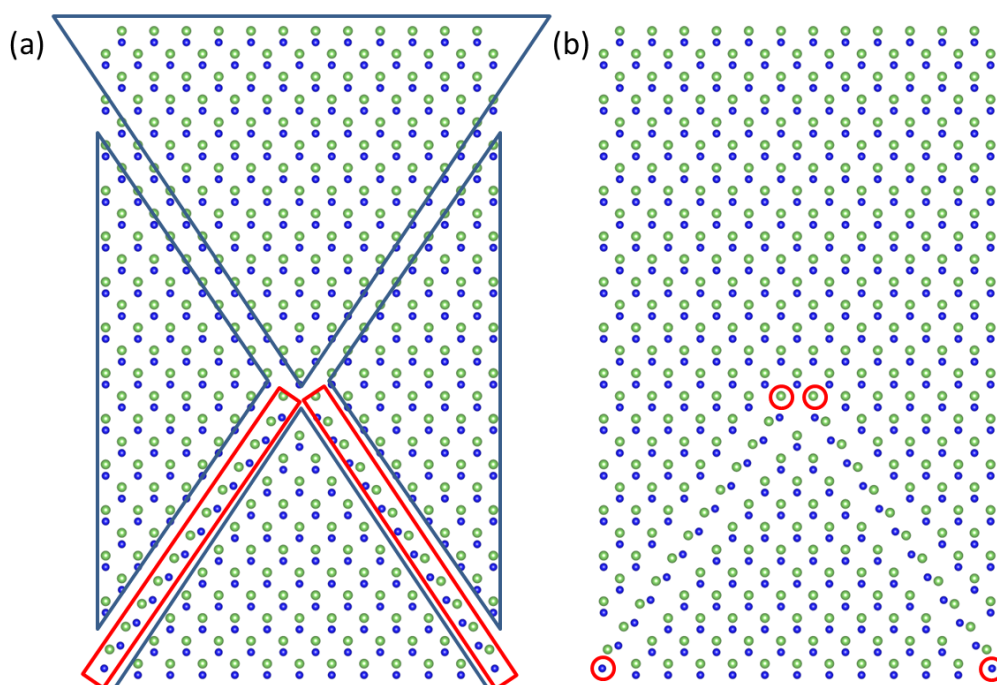


Figure 4.3 – (a) different cut-planes of the bulk model used to model the initial configuration of stair-rod dislocation (b) Initial model of the stair-rod dislocation model generated by Rhodius with single atomic dislocation cores circled in red.

order to study the effect they might induce on the band gap and more in general, on the electronic structure of bulk GaAs. DFT calculations were performed within the Gaussian-plane wave (GPW) method as implemented in the CP2K package [178] with DZVP basis sets for the representation of Kohn-Sham orbitals, with plane-wave cutoff for the charge density of 600 Ry. An initial geometry optimization was performed using

Chapter 4. Planar Defects: Stacking Faults

the Perdew-Burke-Ernzerhof (PBE) [16] GGA exchange-correlation functional. In this case, PBE severely underestimates the band gap; therefore, single point calculations were performed using the hybrid functional developed by Heyd-Scuseria-Ernzerhof (HSE06) [20], as discussed in chapter 1.

To speed up the calculations, the auxiliary density matrix method (ADMM) [179]

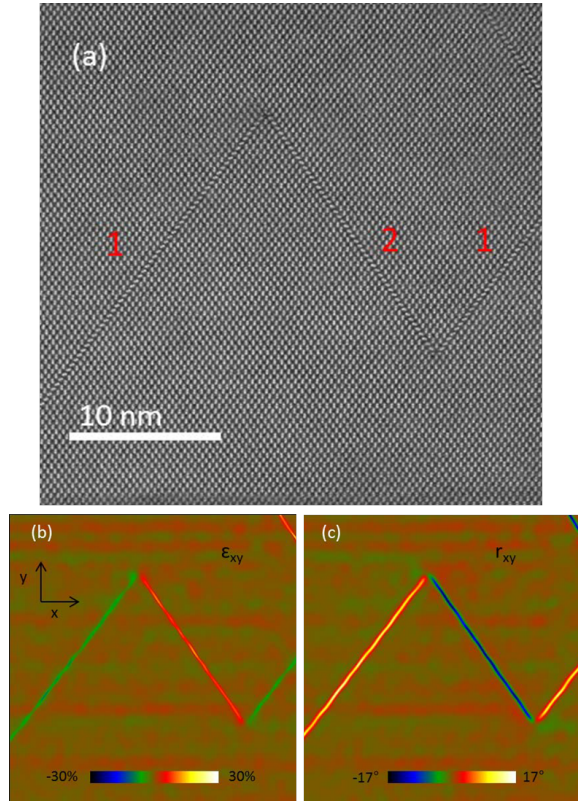


Figure 4.4 – HAADF-STEM micrograph showing the three different intrinsic stacking faults, labeled with 1 and 2 depending on the glide plane, merging together to form two distinct stair-rod dislocations. Panels (b) and (c) illustrate the ϵ_{xy} strain and the rotational maps, respectively. The lattice deformation was determined relative to an internal reference lattice selected at an area close to the upper stair-rod dislocation. While the detected strains and rotations are attributable to the intrinsic stacking faults, no long-range strain fields are detected at the vicinity of the dislocation cores. This figure is adapted from ref[163].

with FIT6 auxiliary basis sets was employed. Maximally localized Wannier functions [180] were extracted using CP2K. In order to investigate the effect of the stair-rod defects on the electronic properties of GaAs, DFT calculations were performed on two different models. A $6 \times 6 \times 6$ supercell (corresponding to 16.96 Å in each direction)

4.1. Modeling Interacting Stacking Faults Resulting in Stair-rod Dislocations in GaAs Nanowires

with 1728 atoms was adopted for the bulk structure, while the defective area was incorporated in a supercell with 924 atoms consisting of $12 \times 12 \times 2$ unit cells. After properly relaxing the structure, the models were imported in STEMCELL and used to simulate HAADF images[161, 181]. To validate the ab-initio simulated structures strain mapping was performed by the use of geometric phase analysis (GPA)[182] within the FRWR plugin. The results obtained from the DFT-relaxed model were then compared with the GPA maps of experimentally obtained images. Subsequently, GPA maps of the modeled structure were compared with the experimental ones. Concordantly, both experimental and simulated data show quantitatively comparable strain and rotational maps at the intrinsic stacking faults with no long-range strain fields contributions stemming from the dislocation cores (figures 4.4 and 4.5). This confirms the structural validity of the adopted DFT model.

4.1.6 Computational Results

Figure 4.6(a) and figure 4.7(a) show the bulk and defective supercells simulated with DFT to investigate the effect induced by the defects on the GaAs electronic properties. Both structures were relaxed using PBE functional until the force acting on each atom was less than 0.01 eV/\AA . The PBE band gap of the bulk GaAs was 0.53 eV , highly underestimated with respect to the 1.43 eV experimentally reported in literature[183] with a difference of 63%. Single point calculation with hybrid functional HSE06 was then performed to correct the error and a band gap of $\sim 1.14 \text{ eV}$ with a difference of 21% was obtained. The DOS for the bulk structure is shown in figure 4.6(b). The majority of valence states are equally contributed by both Ga and As atoms, with a signature of localized states rising at $+1.14 \text{ eV}$, as visible in figure 4.6(c). The major unoccupied states contribute above $+2.0 \text{ eV}$ with a slightly higher intensity from the Ga atoms. The bonding hybridization simulation for the defect-free bulk is shown in the inset of figure 4.6(a). The model is here oriented along the $[100]$ zone axis to exhibit the Wannier orbitals geometry. As expected, four different sp^3 hybrid orbitals separated by 109.5° connecting the Ga atom to the neighboring As atoms are obtained. The same

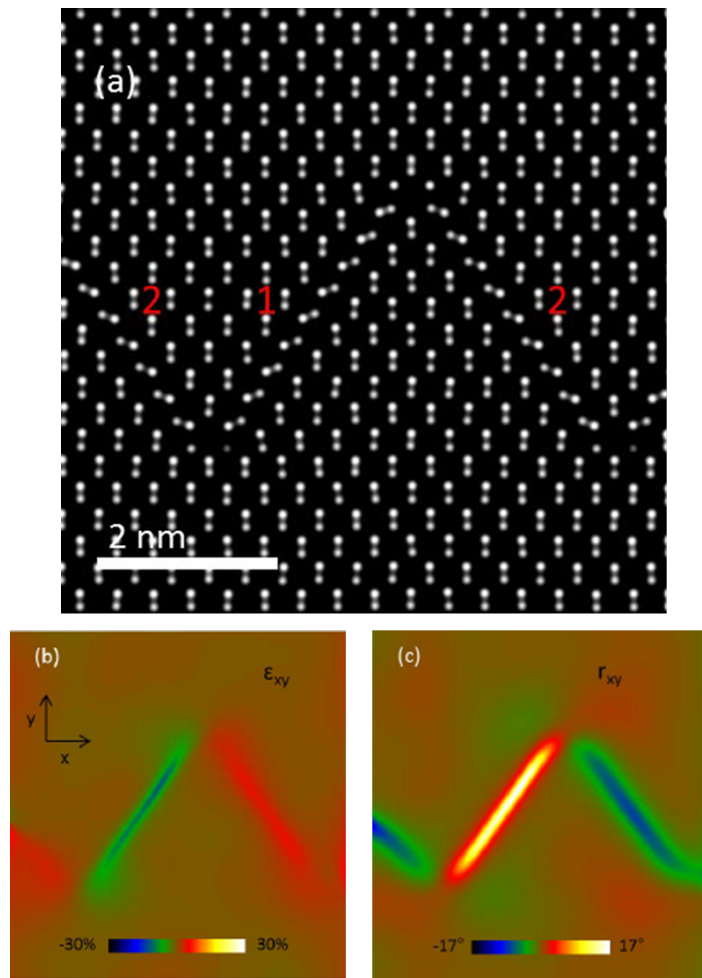


Figure 4.5 – HAADF-STEM simulated micrograph obtained from the relaxed model. As in the previous case, the intrinsic stacking faults creating the dislocation cores are labeled with 1 and 2 depending on the glide plane. (b,c) GPA maps (obtained using the same parameters used for the experimental data) of the modeled structure reproducing the ϵ_{xy} strain and rotational magnitude. Also in this case, no strain fields are detected in the proximity of the dislocation cores; only the planar defects contribute to the strains and rotations. These results, compared to the experimental ones of figure 4.4, confirm the structural validity of the model employed to perform the DFT calculations. This figure is adapted from ref[163].

4.1. Modeling Interacting Stacking Faults Resulting in Stair-rod Dislocations in GaAs Nanowires

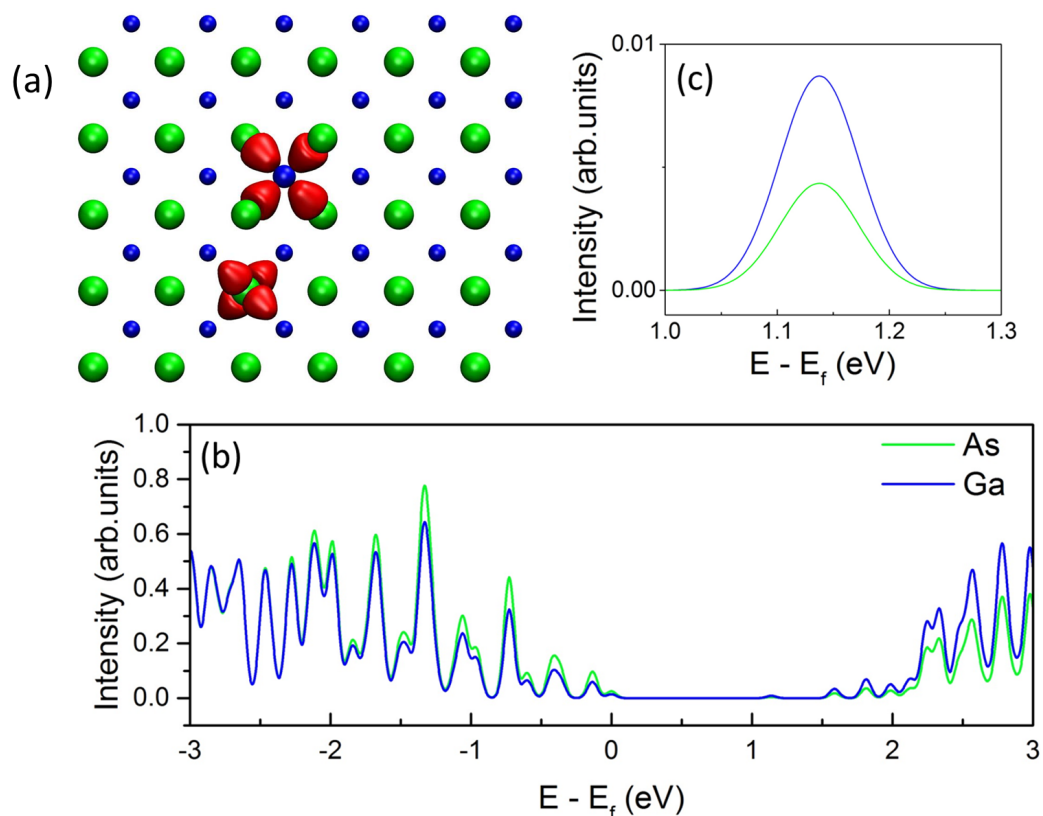


Figure 4.6 – (a) Bulk structure model of GaAs (Gallium (blue) and arsenic (green)). The orbitals simulation represented in panel illustrates the four sp^3 hybrid wannier orbitals present among around Ga and As atoms (b) associated DOS plot. The states are equally contributing along the whole energy range with a slight difference for the unoccupied states after 2.0 eV only. (c) The first localized state is observed at ~ 1.14 eV and these states are shown in this window. This figure is adapted from ref[163].

hybridization is also visible for the As atom connected with the four Ga atoms. The distance between the two dislocations in the modeled defective structure is not equal to the experimental observations due to the complexity to perform the calculations on such large crystal. For this reason, the distance in the simulated model is around 1/3 of the experimental one.

The defect model is divided into four regions as illustrated in figure 4.7(a), the regions are; As core (green), Ga core (blue), intrinsic stacking faults (red) and the remaining atoms in the bulk (gray). Similarly, in Figure 4.7(b) the analysis is performed by further dividing the intrinsic stacking fault into three parts: Ga core proximity (pink block 1), intermediate stacking faults (orange block 2) and As core proximity (black block

3). As done previously, the single point calculation with HSE06 functional was performed for the defective structure. The HSE06 calculated localized state, previously observed at +1.14 eV for the bulk structure, decreases to +0.67 eV (figure 4.7(e),(f)). The peak, present in all the areas taken into consideration in the structure, suggests an overall influence by the dislocation cores on the electron cloud of the entire modeled crystal. A comparison of the DOS contributions coming from the Ga and As dislocation core atoms is presented in figure 4.7(c). Ga core atoms (blue line) show a major contribution in the valence band states while the As core atoms (green line) have a predominant distribution in the conduction band states with a double peak present around 1.25 eV.

Major contributions at +1 eV are due to the As core atoms followed by the contributions from the atoms on the intrinsic stacking faults (red) and then from the remaining atoms (gray line). For the Ga core atoms, the effective contribution starts only after +1.7 eV. As in the defect-free bulk model, the bonding orbitals were simulated in correspondence of the two dislocation cores. The results are illustrated in figure 4.8(a) and 4.8(b) for the Ga and As single atoms, respectively. The dislocation cores develop a configuration between sp^3 and sp^2 where three hybrid orbitals separated by 120° are obtained. The presence of an unpaired orbital generates a distortion in the three orbitals geometry not allowing the standard sp^2 planar configuration. This can be connected to the difference in DOS in the valence and conduction band present in the single Ga and As atoms. These results further made us explore the behavior of the DOS contribution of the atoms connecting these two different dislocation cores. Figure 4.7(d) shows the DOS plots from the atoms in the three different sections as previously described for the structure in Figure 4.7(b). The DOS distribution of block 1 (pink line) is very similar to that of the Ga core atoms where there is a minimum contribution in the conduction band after +1.7 eV and a significant increase in the states below the Fermi level. Similarly, block 3 (black line) follows the trend of the As core atoms where the majority of unoccupied states are concentrated at +1.0 eV and almost zero states in the valence band states. Atoms in block 2 (orange line) have a distribution in between the As and Ga core DOS plots. In fact, both conduction and valence band states are visible with a lower intensity with respect to both block 1 and

4.1. Modeling Interacting Stacking Faults Resulting in Stair-rod Dislocations in GaAs Nanowires

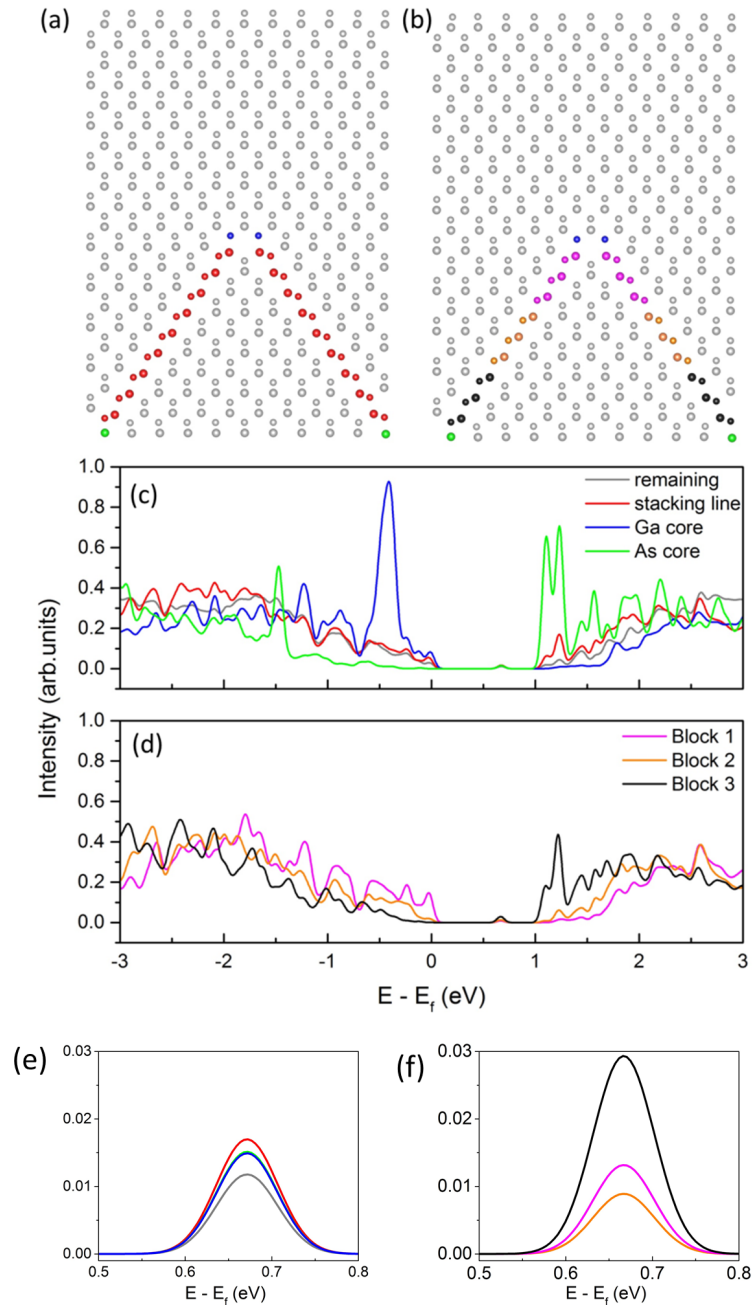


Figure 4.7 – (a) Model used to investigate the DOS in the Ga core (blue), As core (green), entire stacking fault (red) and remaining crystal (gray). The associated DOS plot (c) shows, with same color codes for the first three sections, the reduction in energy gap and the presence of valence and conduction band states. (b) Model where the calculations were performed by dividing the stacking fault into three sections labeled as block 1, 2 and 3. The associated DOS plot in panel (d) shows the transition from Ga core valence states to As core conduction states. (e) and (f) shows the localized states present at +0.57 eV. This figure is adapted with some modifications from ref[163].

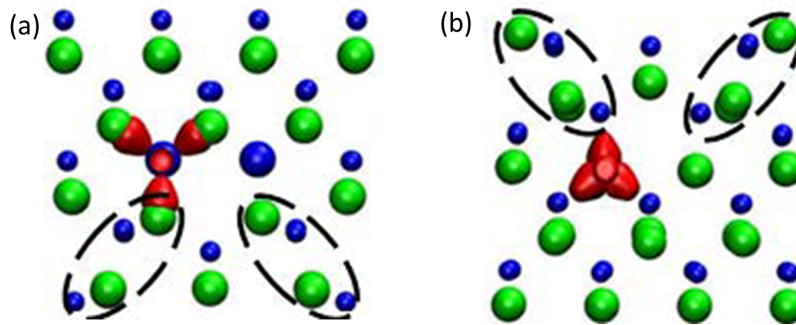


Figure 4.8 – The Wannier orbitals (in red) showing the quasi-sp² geometry are illustrated in panel (a) and (b) for the Ga and As dislocation core, respectively. The black dashed ellipses highlight the position of the stacking faults. This figure is adapted with some modifications from ref[163].

3. This effect is probably emphasized as a consequence of the shorter distance, but the same qualitative behavior, with respect to the experimental structure.

Furthermore, an analysis of the potential energy is performed in figure 4.9(a) where the electron density map of the two dislocation cores with potential color scale is shown. Figure 4.9(b) represents the electrostatic energy along the stacking fault line with the As core showing the highest potential energy acting as LUMO and the Ga core with the lowest potential energy acting as HOMO. This investigation clearly shows the formation of an electric field between the Ga core and As core suggesting a donor and acceptor behavior, respectively. This could lead to an improved carrier separation and a reduction in detrimental recombination.

Furthermore, since the dislocation cores in both cases are assumed to propagate along the whole length of the nanowire, the highly localized nature of the DOS can induce the formation of nano-channels, as shown in figure 4.9(c), able to facilitate the transport of electrons and holes for the Ga and As core, respectively. This phenomenon, recently studied for a transition-metal-dichalcogenide [184], can be further analyzed and exploited in future for the realization of innovative devices where the combination of different growth conditions and materials can lead to the formation of preferential paths for improved mono-dimensional carrier transport.

4.1. Modeling Interacting Stacking Faults Resulting in Stair-rod Dislocations in GaAs Nanowires

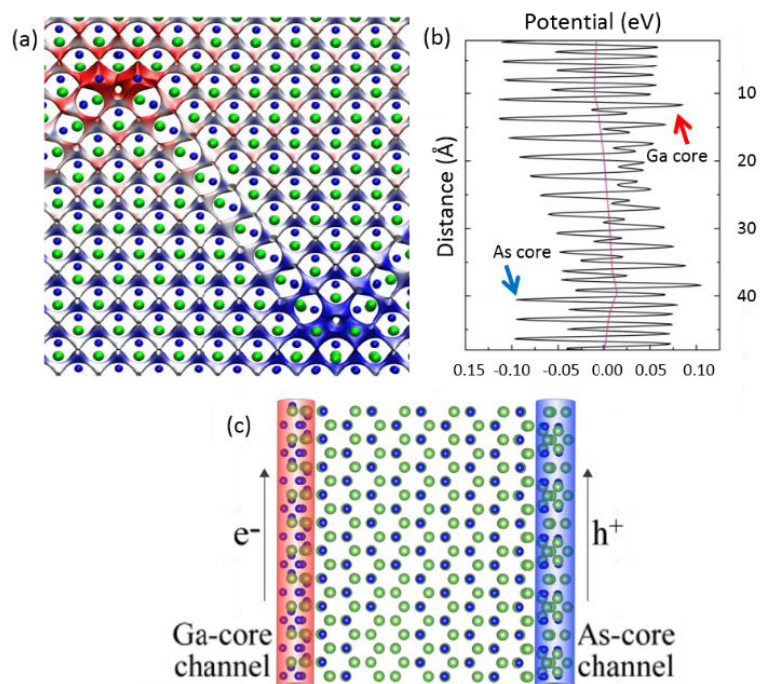


Figure 4.9 – Electron density map with an isosurface value of $4.1 \times 10^{-3} \text{ e}/\text{\AA}^3$ and potential color gradient scale in red (max) and blue (min). (b) Distribution of the electrostatic potential in the [001] direction along the stacking fault with average potential energy represented with a magenta line. (c) Graphical representation, along the $[1\bar{1}1]$ zone axis perpendicular to the intrinsic stacking fault, of the nano-channels generated by the two dislocations. Preferential paths for electrons and holes, reflecting the behavior described with the potential energy map, are formed along the Ga- and As-cores, respectively. This figure is adapted with some modifications from ref[163].

4.1.7 Conclusions

In conclusion, aberration-corrected STEM has been used to assess the atomic structure of two stair-rod dislocations obtained by merging multiple stacking faults in v-shaped defects. Elemental EDX mapping has been employed to unambiguously identify the nature of the single atomic columns at the dislocation cores, revealing that they consist of either solely gallium or arsenic. Their effect on the electronic properties has been investigated by means of DFT calculations showing a reduced energy gap with respect to the bulk material. Furthermore, a shift of highly localized DOS from the valence band in the gallium core (acceptor center) to the conduction band in the arsenic core (donor center) has been observed, probably attributable to

Chapter 4. Planar Defects: Stacking Faults

the unpaired p -orbitals in the quasi- sp^2 bonding configuration of the single atomic columns. These results suggest the possibility to obtain preferential paths within the nanowire where electron and holes are trapped and transported along the two dislocation cores.

5 Conclusions and Outlook

5.1 Conclusions

This thesis presents advanced computational methods in the field of electron microscopy and spectroscopy to characterize crystal defects supported by advanced experimental data. The focus of my work has been the atomistic modeling of several systems with classical and ab initio methods. My analysis, along with the experimental measurements, builds up a sort of "computationally augmented experimental laboratory" with the aim of understanding the observations and suggesting novel directions in important fields of applied materials science. The main focus of this thesis is on characterizing defects. It is very important to characterize such defects at the atomic level and to develop a better understanding of their local bonding characteristics. Such valuable insights would help in further engineering these defects to utilize the functional material in an efficient way. Experimental and theoretical investigations were performed for different dimensional (point, line and planar) defects to shed light on the nature of the defect and their impact on the performance of the material. This thesis demonstrates how the combined approach of advanced experimental techniques and atomistic simulations complemented each other's limitation to reveal the defect bonding characteristics, structural information and their correlation with the material functionality. Having demonstrated the applicability of WIEN2k and FEFF code to calculate EELS or XANES, reliable computational methodologies were

Chapter 5. Conclusions and Outlook

implemented to study the impact of defects on the functional properties of the material. Considerable success has been achieved using these methodologies in deducing the structural properties of defects.

In chapter 2.1, the role of v_o in photocatalytic-activity of BiVO_4 (BVO) was studied using HAADF-STEM and EELS by recording V-L edge EELS line profile perpendicular to the surface. The experimental finding suggests the reduction of Vanadium ion towards the surface. The next task was to estimate the amount of v_o concentration which was helpful to build the theoretical model for simulations. Another set of experiments were planned, where EELS for three different Vanadium oxide samples (V_2O_3 , VO_2 and V_2O_5) was recorded and compared with the V-L edge EELS from the surface of BVO. These interpretations gave a rough estimate of 15% presence of v_o on the surface. The next question was to figure out how the v_o affect the photocatalytic activity in BVO. This is where DFT simulations proved to be crucial. DFT simulations were performed to benchmark the model using EELS simulations and comparing it with experimentally-recorded EELS. The main results from my simulations shows that v_o on the surface give rise to donor states between valence and conduction band responsible for deploying the photocatalytic activity in BVO.

Similarly, in chapter 2.2, the electronic structure of SrMnO_3 (SMO) on different substrates leading to different strains were examined using HAADF-STEM and EELS. The recorded EELS spectra show considerable changes in the O-K edge EELS of SMO across different substrates. DFT simulations were performed to confirm that the changes in the EELS are affected by the amount of oxygen vacancies incorporated in the structure and least by the strain effects due to the substrate. These theoretical findings provide more insights into the electronic structure of strained SMO and will help in future research to better control its multiferroic properties using strain as a parameter.

In chapter 3, the HAADF-STEM investigation suggested the presence of Bi atoms in the edge dislocation core of BiFeO_3 . Based upon this finding, a theoretical methodology was presented to model edge dislocations and simulate dislocation core structures by performing molecular dynamics using classical BVVS potentials. Then, FEFF, a real-space multiple-scattering code, was employed to calculate the O-K edge EELS for

O atoms above and below the core to compare them with the experiments. Using this combined strategy, it was found that EELS does not compare well with experiments for the system with only Bi atoms in the core. After carefully paying attention to the EDX data, the presence of Fe atoms was confirmed in the core. Different concentration of Fe atoms was incorporated in the dislocation core model and EELS was computed for each of them. This also improved the comparison with experimentally-recorded EELS. This investigation further gave birth to the idea of magnetic dislocations cores and the first results from electron holography suggested the cores to be magnetic. There are more experiments planned in near future to figure out the magnitude of magnetism in the core and how it can be utilized for future magnetic and electronic devices. Thus, the main achievement here was the interpretation of data from different techniques based on my atomistic simulations, together with the development of a methodology to prepare structural models based on classical potentials, continuum models, and experimental information. Such strategy will be applicable also to other classes of systems.

The methodology of performing experiments and atomistic simulations in tandem proved very fruitful in deducing structural properties and physical properties of defects in materials. Such methodology is helpful in overcoming the shortcomings of both experiments and theoretical calculations by supporting each other within their limitations. Furthermore, the approaches implemented in this dissertation will be helpful in future to study interesting complex materials and their defects.

5.2 Outlook

In this thesis, I have presented work on characterizing defects in different complex oxides and GaAs. Here, I want to make some comments on possible future work and challenges.

During this work, the edge dislocation in BFO were found to be weakly ferromagnetic, which makes this defect quite interesting. I characterized this system with classical molecular dynamics and FEFF. Though, there is some work remaining to understand such magnetism and provide insights into the applicability in future electronic and

Chapter 5. Conclusions and Outlook

magnetic devices. Firstly, the dislocation cores in BFO require further investigation to fully understand their magnetic nature. Magnetic force microscopy experiments are required to confirm the magnetic nature of these dislocation cores and possibly to quantify this effect.

From the simulation point of view, it would be helpful to perform spin-polarized DFT calculations for the dislocation core model. The challenge lies in dealing with an ab-initio model involving a large number of atoms. A different methodology is required to find out the optimized spin-arrangements of Fe-atom in the dislocation core and understand the origin of these magnetic dislocations.

In chapter 2.1, the findings suggested that the reduced surface give rise to localized donor states deploying its photocatalytic activity. These finding needs further research in optimizing the surface of BVO in a way which will enhance its photocatalytic activity. One straightforward solution is to find suitable dopants for Vanadium ions on the surface which would help in canceling those localized donor states. There have been many studies in the literature on various dopants in BVO and estimating its photocatalytic activity. But such findings will give rise to directed-research after having the clear understanding of the impact of v_o on the electronic states in BVO.

I would also like to briefly mention one of my ongoing work which I have not talked about in this thesis. This work is about studying perovskite-type ferrites where Fe is in a rather unusual oxidation state of 4+. SrFeO_3 , where Sr exists strictly in 2+ state forces Fe to be in the tetravalent state. This material is not only interesting because it contains Fe^{4+} but because of its structural features displays oxygen deficient phases. These phases exhibit a wide variety of structural and physical properties depending on their oxygen vacancy concentrations.

The HAADF-STEM images are recorded for this material grown on SrTiO_3 . Figure 1(a) shows the HAADF STEM images of SrFeO_3 with planar defects. O-K edge EEL spectra are also recorded from the bulk and the planar defects. Figure 1(b) shows the O-K edge EELS spectra from the two regions (planar defect and bulk). The questions to be addressed here are: 1) what is the structure of the planar defects? 2) Are there v_o present in these planar defects? 3) If yes, what is the concentration v_o ? The different features in EELS signals are due to the structural arrangement or v_o concentration

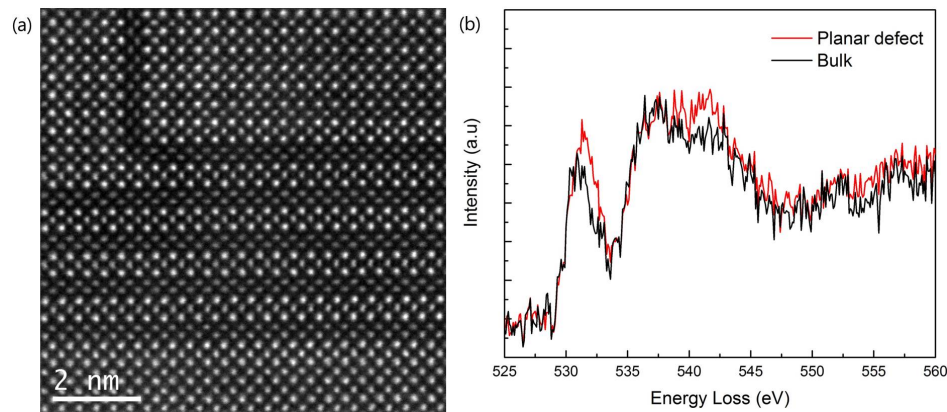


Figure 5.1 – (a) HAADF+STEM image of planar defects within a SrFeO_3 thin film grown on a SrTiO_3 substrate. (b) O- K edge EEL spectra for obtained at the planar defects and the SrFeO_3 bulk (i.e. far from the defects).

also has a role to play?

The questions asked above need to be answered with the help of atomistic simulations. Theoretically, different models can be built with the known structural configuration from HAADF-STEM images. Then, structural optimization can be performed with and without v_{O} . After obtaining the optimized structural, the simulated EELS can be compared with the experiments to confirm the ambiguity about the v_{O} .

In order to be able to solve such problems, which are accessible by STEM/EDX/EELS, it was also important to implement atomistic modeling within this thesis. The implementation of theoretical tools proved to be essential in further deducing the structural configuration of defects and their effect on the physical properties of the bulk material.



Bibliography

- [1] M. Dawber, K. M. Rabe and J. F. Scott, “Physics of thin-film ferroelectric oxides”, *Rev. Mod. Phys.*, 2005, **77**, 1083–1130.
- [2] S. A. Chambers, T. C. Droubay, C. M. Wang, K. M. Rosso, S. M. Heald, D. A. Schwartz, K. R. Kittilstved and D. R. Gamelin, “Ferromagnetism in oxide semiconductors”, *Materials Today*, 2006, **9**, 28–35.
- [3] G. Chen, J.-M. Langlois, Y. Guo and W. A. Goddard, “Superconducting properties of copper oxide high-temperature superconductors”, *Proc Natl Acad Sci U S A*, 1989, **86**, 3447–3451.
- [4] E. Fortunato, P. Barquinha and R. Martins, “Oxide Semiconductor Thin-Film Transistors: A Review of Recent Advances”, *Advanced Materials*, 2012, **24**, 2945–2986.
- [5] N. Setter, D. Damjanovic, L. Eng, G. Fox, S. Gevorgian, S. Hong, A. Kingon, H. Kohlstedt, N. Y. Park, G. B. Stephenson, I. Stolitchnov, A. K. Taganstev, D. V. Taylor, T. Yamada and S. Streiffer, “Ferroelectric thin films: Review of materials, properties, and applications”, *Journal of Applied Physics*, 2006, **100**, 051606.
- [6] A. Khan, Z. Abas, H. S. Kim and I.-K. Oh, “Piezoelectric thin films: an integrated review of transducers and energy harvesting”, *Smart Materials and Structures*, 2016, **25**, 053002.
- [7] <https://www.ccber.ucsb.edu/collections-botanical-collections-plant-anatomy/transmission-electron-microscope>.
- [8] O. Scherzer, “The Theoretical Resolution Limit of the Electron Microscope”, *Journal of Applied Physics*, 1949, **20**, 20–29.

- [9] O. Scherzer, “Sphärische und chromatische Korrektur von Elektronenlinsen”, *Optik*, 1947, **2**, 114.
- [10] Serin, Virginie, Zanchi, Gerald and Sévely, Jean, “EXELFS as a structural tool for studies of low Z -elements”, *Microsc. Microanal. Microstruct.*, 1992, **3**, 201–212.
- [11] T. Sikora, G. Hug, M. Jaouen and J. J. Rehr, “Multiple-scattering EXAFS and EXELFS of titanium aluminum alloys”, *Phys. Rev. B*, 2000, **62**, 1723–1732.
- [12] J. Hillier and R. F. Baker, “Microanalysis by Means of Electrons”, *Journal of Applied Physics*, 1944, **15**, 663–675.
- [13] M. Nelhiebel, P.-H. Louf, P. Schattschneider, P. Blaha, K. Schwarz and B. Joffrey, “Theory of orientation-sensitive near-edge fine-structure core-level spectroscopy”, *Phys. Rev. B*, 1999, **59**, 12807–12814.
- [14] P. Hohenberg and W. Kohn, “Inhomogeneous Electron Gas”, *Phys. Rev.*, 1964, **136**, B864–B871.
- [15] W. Kohn and L. J. Sham, “Self-Consistent Equations Including Exchange and Correlation Effects”, *Phys. Rev.*, 1965, **140**, A1133–A1138.
- [16] J. P. Perdew, K. Burke and M. Ernzerhof, “Generalized Gradient Approximation Made Simple”, *Phys. Rev. Lett.*, 1996, **77**, 3865–3868.
- [17] S. L. Dudarev, G. A. Botton, S. Y. Savrasov, C. J. Humphreys and A. P. Sutton, “Electron-energy-loss spectra and the structural stability of nickel oxide: An LSDA+ U study”, *Phys. Rev. B*, 1998, **57**, 1505–1509.
- [18] C. Lee, W. Yang and R. G. Parr, “Development of the Colle-Salvetti correlation-energy formula into a functional of the electron density”, *Phys. Rev. B*, 1988, **37**, 785–789.
- [19] A. D. Becke, “Density functional thermochemistry. III. The role of exact exchange”, *The Journal of Chemical Physics*, 1993, **98**, 5648–5652.
- [20] A. V. Krukau, O. A. Vydrov, A. F. Izmaylov and G. E. Scuseria, “Influence of the exchange screening parameter on the performance of screened hybrid functionals”, *The Journal of Chemical Physics*, 2006, **125**, 224106.

Bibliography

- [21] A. Svane and O. Gunnarsson, “Transition-metal oxides in the self-interaction–corrected density-functional formalism”, *Phys. Rev. Lett.*, 1990, **65**, 1148–1151.
- [22] S. Massidda, M. Posternak and A. Baldereschi, “Hartree-Fock LAPW approach to the electronic properties of periodic systems”, *Phys. Rev. B*, 1993, **48**, 5058–5068.
- [23] E. Kaxiras, *Atomic and Electronic Structure of Solids*, Cambridge University Press, 2003.
- [24] E Sjöstedt, L Nordström and D. Singh, “An alternative way of linearizing the augmented plane-wave method”, *Solid State Communications*, 2000, **114**, 15–20.
- [25] C. J. Pickard, M. C. Payne, L. M. Brown and M. N. Gibbs, “Ab initio EELS with a plane wave basis set”, *Electron Microscopy and Analysis*, 1995, 211–214.
- [26] C. J. Pickard and M. C. Payne, “Ab initio EELS: beyond the fingerprint”, *Electron Microscopy and Analysis*, 1997, 179–182.
- [27] C. Hébert, “Practical aspects of running the WIEN2k code for electron spectroscopy”, *Micron*, 2007, **38**, 12–28.
- [28] C. Hébert-Souche, P.-H. Louf, P. Blaha, M. Nelhiebel, J. Luitz, P. Schattschneider, K. Schwarz and B. Jouffrey, “The orientation-dependent simulation of ELNES”, *Ultramicroscopy*, 2000, **83**, 9–16.
- [29] <http://theory.cm.utexas.edu/henkelman/research/bader/>.
- [30] R. F. W. Bader, *Available from:* <http://www.chemistry.mcmaster.ca/faculty/bader/aim/>.
- [31] J Sofo and J Fuhr, *WIENROOT/SRC/aimsofonotes.ps*, 2001.
- [32] B. M. and M. Goppert-Mayer, “in *Handbuch der Physik*”, 1933, **24**, 623.
- [33] R. Resta, “Macroscopic polarization in crystalline dielectrics: the geometric phase approach”, *Rev. Mod. Phys.*, 1994, **66**, 899–915.
- [34] R. Resta and D. Vanderbilt, “in *Theory of polarization: a modern approach. Physics of Ferroelectrics, Topics Appl. Physics*”, 2007, **105**, 31–68.

- [35] P. Ghosez, <http://www.phythema.ulg.ac.be/webroot/misc/books/PhD-Ph.Ghosez.pdf>.
- [36] R. D. King-Smith and D. Vanderbilt, “Theory of polarization of crystalline solids”, *Phys. Rev. B*, 1993, **47**, 1651–1654.
- [37] M. V. Berry, “Quantal phase factors accompanying adiabatic changes”, *Proceedings of the Royal Society of London A: Mathematical, Physical and Engineering Sciences*, 1984, **392**, 45–57.
- [38] S. Ahmed, J. Kivinen, B. Zaporzan, L. Curiel, S. Pichardo and O. Rubel, “BerryPI: A software for studying polarization of crystalline solids with WIEN2k density functional all-electron package”, *Computer Physics Communications*, 2013, **184**, 647–651.
- [39] L. Campbell, L. Hedin, J. J. Rehr and W. Bardyszewski, “Interference between extrinsic and intrinsic losses in x-ray absorption fine structure”, *Phys. Rev. B*, 2002, **65**, 064107.
- [40] J. J. Rehr and R. C. Albers, “Theoretical approaches to x-ray absorption fine structure”, *Rev. Mod. Phys.*, 2000, **72**, 621–654.
- [41] E. A. Stern, “Theory of the extended x-ray-absorption fine structure”, *Phys. Rev. B*, 1974, **10**, 3027–3037.
- [42] J. S. Faulkner, “Multiple-scattering approach to band theory”, *Phys. Rev. B*, 1979, **19**, 6186–6206.
- [43] A. L. Ankudinov, B. Ravel, J. J. Rehr and S. D. Conradson, “Real-space multiple-scattering calculation and interpretation of x-ray-absorption near-edge structure”, *Phys. Rev. B*, 1998, **58**, 7565–7576.
- [44] M. Moreno, K. Jorissen and J. Rehr, “Practical aspects of electron energy-loss spectroscopy EELS calculations using FEFF8”, *Micron*, 2007, **38**, 1–11.
- [45] K. Jorissen, J. J. Rehr and J. Verbeeck, “Multiple scattering calculations of relativistic electron energy loss spectra”, *Phys. Rev. B*, 2010, **81**, 155108.
- [46] L. Hedin, “New Method for Calculating the One-Particle Green’s Function with Application to the Electron-Gas Problem”, *Phys. Rev.*, 1965, **139**, A796–A823.

Bibliography

- [47] L. Hedin and S. Lundqvist, “Effects of Electron-Electron and Electron-Phonon Interactions on the One-Electron States of Solids”, *Solid State Physics*, 1970, **23**, 1–181.
- [48] P. A. M. Dirac, “Note on Exchange Phenomena in the Thomas Atom”, *Mathematical Proceedings of the Cambridge Philosophical Society*, 1930, **26**, 376–385.
- [49] M. Taillefumier, D. Cabaret, A.-M. Flank and F. Mauri, “X-ray absorption near-edge structure calculations with the pseudopotentials: Application to the K edge in diamond and α -quartz”, *Phys. Rev. B*, 2002, **66**, 195107.
- [50] A. L. Ankudinov, Y. Takimoto and J. J. Rehr, “Combined Bethe-Salpeter equations and time-dependent density-functional theory approach for x-ray absorption calculations”, *Phys. Rev. B*, 2005, **71**, 165110.
- [51] C. Zhang and P. D. Bristowe, “First principles calculations of oxygen vacancy formation in barium-strontium-cobalt- ferrite”, *RSC Adv.*, 2013, **3**, 12267–12274.
- [52] B. J. Morgan and G. W. Watson, “A Density Functional Theory + U Study of Oxygen Vacancy Formation at the (110), (100), (101), and (001) Surfaces of Rutile TiO₂”, *The Journal of Physical Chemistry C*, 2009, **113**, 7322–7328.
- [53] A. F. Wright and N. A. Modine, “Comparison of two methods for circumventing the Coulomb divergence in supercell calculations for charged point defects”, *Phys. Rev. B*, 2006, **74**, 235209.
- [54] J. Shim, E.-K. Lee, Y. J. Lee and R. M. Nieminen, “Density-functional calculations of defect formation energies using supercell methods: Defects in diamond”, *Phys. Rev. B*, 2005, **71**, 035206.
- [55] C. W. M. Castleton, A. Höglund and S. Mirbt, “Managing the supercell approximation for charged defects in semiconductors: Finite-size scaling, charge correction factors, the band-gap problem, and the ab initio dielectric constant”, *Phys. Rev. B*, 2006, **73**, 035215.

- [56] S. B. Zhang and J. E. Northrup, “Chemical potential dependence of defect formation energies in GaAs: Application to Ga self-diffusion”, *Phys. Rev. Lett.*, 1991, **67**, 2339–2342.
- [57] C. G. Van de Walle, D. B. Laks, G. F. Neumark and S. T. Pantelides, “First-principles calculations of solubilities and doping limits: Li, Na, and N in ZnSe”, *Phys. Rev. B*, 1993, **47**, 9425–9434.
- [58] U. Aschauer, R. Pfenninger, S. M. Selbach, T. Grande and N. A. Spaldin, “Strain-controlled oxygen vacancy formation and ordering in CaMnO₃”, *Phys. Rev. B*, 2013, **88**, 054111.
- [59] S. Cheng, M. Li, Q. Meng, W. Duan, Y. G. Zhao, X. F. Sun, Y. Zhu and J. Zhu, “Electronic and crystal structure changes induced by in-plane oxygen vacancies in multiferroic YMnO₃”, *Phys. Rev. B*, 2016, **93**, 054409.
- [60] Y. Arroyo Rojas Dasilva, R. Kozak, R. Erni and M. Rossell, “Structural defects in cubic semiconductors characterized by aberration-corrected scanning transmission electron microscopy”, *Ultramicroscopy*, 2017, **176**, 11–22.
- [61] G. Lu, in *Handbook of Materials Modeling: Methods*, Springer Netherlands, 2005, pp. 793–811.
- [62] J. W. Christian and V Vitek, “Microanalysis by Means of Electrons”, *Rep. Prog. Phys.*, 1970, **33**, 307.
- [63] B. Joós, Q. Ren and M. S. Duesbery, “Peierls-Nabarro model of dislocations in silicon with generalized stacking-fault restoring forces”, *Phys. Rev. B*, 1994, **50**, 5890–5898.
- [64] D. Ferré, P. Carrez and P. Cordier, “Modeling dislocation cores in SrTiO₃ using the Peierls-Nabarro model”, *Phys. Rev. B*, 2008, **77**, 014106.
- [65] I. Sugiyama, N. Shibata, Z. Wang, S. Kobayashi, T. Yamamoto and Y. Ikuhara, “Ferromagnetic dislocations in antiferromagnetic NiO”, *Nature Nanotechnology*, 2013, **8**, 266–270.

Bibliography

- [66] B. von Sydow, J. Hartford and G. Wahnström, “Atomistic simulations and Peierls-Nabarro analysis of the Shockley partial dislocations in palladium”, *Computational Materials Science*, 1999, **15**, 367–379.
- [67] T. Ishida, K. Kakushima, T. Mizoguchi and H. Fujita, “Role of Dislocation Movement in the Electrical Conductance of Nanocontacts”, *Scientific Reports*, 2012, **2**, srep00623.
- [68] M. Camarda, A. Canino, A. L. Magna, F. L. Via, G. Feng, T. Kimoto, M. Aoki and H. Kawanowa, “Structural and electronic characterization of (2,33) bar-shaped stacking fault in 4H-SiC epitaxial layers”, *Applied Physics Letters*, 2011, **98**, 051915.
- [69] R. Han and D. S. Sholl, “Computational Model and Characterization of Stacking Faults in ZIF-8 Polymorphs”, *The Journal of Physical Chemistry C*, 2016, **120**, 27380–27388.
- [70] C. Li, Y. Wu, T. J. Pennycook, A. R. Lupini, D. N. Leonard, W. Yin, N. Paudel, M. Al-Jassim, Y. Yan and S. J. Pennycook, “Carrier Separation at Dislocation Pairs in CdTe”, *Phys. Rev. Lett.*, 2013, **111**, 096403.
- [71] S. Liu, I. Grinberg and A. M. Rappe, “Development of a bond-valence based interatomic potential for BiFeO₃ for accurate molecular dynamics simulations”, *Journal of Physics: Condensed Matter*, 2013, **25**, 102202.
- [72] S. Liu, I. Grinberg, H. Takenaka and A. M. Rappe, “Reinterpretation of the bond-valence model with bond-order formalism: An improved bond-valence-based interatomic potential for PbTiO₃”, *Phys. Rev. B*, 2013, **88**, 104102.
- [73] M. D. Rossell, P. Agrawal, A. Borgschulte, C. Hébert, D. Passerone and R. Erni, “Direct Evidence of Surface Reduction in Monoclinic BiVO₄”, *Chemistry of Materials*, 2015, **27**, 3593–3600.
- [74] A. Kudo, K. Omori and H. Kato, “A Novel Aqueous Process for Preparation of Crystal Form-Controlled and Highly Crystalline BiVO₄ Powder from Layered Vanadates at Room Temperature and Its Photocatalytic and Photophysical Properties”, *Journal of the American Chemical Society*, 1999, **121**, 11459–11467.

- [75] Y. Zhou, K. Vuille, A. Heel, B. Probst, R. Kontic and G. R. Patzke, “An inorganic hydrothermal route to photocatalytically active bismuth vanadate”, *Applied Catalysis A: General*, 2010, **375**, 140–148.
- [76] Y. K. Kho, W. Y. Teoh, A. Iwase, L. Mädler, A. Kudo and R. Amal, “Flame Preparation of Visible-Light-Responsive BiVO₄ Oxygen Evolution Photocatalysts with Subsequent Activation via Aqueous Route”, *ACS Applied Materials & Interfaces*, 2011, **3**, 1997–2004.
- [77] S. Kohtani, J. Hiro, N. Yamamoto, A. Kudo, K. Tokumura and R. Nakagaki, “Adsorptive and photocatalytic properties of Ag-loaded BiVO₄ on the degradation of 4-n-alkylphenols under visible light irradiation”, *Catalysis Communications*, 2005, **6**, 185–189.
- [78] M. M. Qurashi and W. H. Barnes, “The structure of pucherite BiVO₄”, *Am. Mineral.*, 1953, **38**, 489.
- [79] J. Granzin and D. Z. Pohl, “Refinement of pucherite, BiVO₄”, *Z. Kristallogr.*, 1984, **169**, 289.
- [80] A. W. Sleight, “Accurate cell dimensions for ABO₄ molybdates and tungstates”, *Acta Crystallographica Section B*, 1972, **28**, 2899.
- [81] S. Tokunaga, H. Kato and A. Kudo, “Selective Preparation of Monoclinic and Tetragonal BiVO₄ with Scheelite Structure and Their Photocatalytic Properties”, *Chemistry of Materials*, 2001, **13**, 4624–4628.
- [82] D. J. Payne, M. D. M. Robinson, R. G. Egdell, A. Walsh, J. McNulty, K. E. Smith and L. F. J. Piper, “The nature of electron lone pairs in BiVO₄”, *Applied Physics Letters*, 2011, **98**, 212110.
- [83] A. Kudo, K. Ueda, H. Kato and I. Mikami, “Photocatalytic O₂ evolution under visible light irradiation on BiVO₄ in aqueous AgNO₃ solution”, *Catalysis Letters*, 1998, **53**, 229–230.
- [84] W. Luo, Z. Yang, Z. Li, J. Zhang, J. Liu, Z. Zhao, Z. Wang, S. Yan, T. Yu and Z. Zou, “Solar hydrogen generation from seawater with a modified BiVO₄ photoanode”, *Energy Environ. Sci.*, 2011, **4**, 4046–4051.

Bibliography

- [85] B. Zhou, X. Zhao, H. Liu, J. Qu and C. Huang, "Visible-light sensitive cobalt-doped BiVO₄ (Co-BiVO₄) photocatalytic composites for the degradation of methylene blue dye in dilute aqueous solutions", *Applied Catalysis B: Environmental*, 2010, **99**, 214–221.
- [86] K. Zhang, X.-J. Shi, J. K. Kim and J. H. Park, "Photoelectrochemical cells with tungsten trioxide/Mo-doped BiVO₄ bilayers", *Phys. Chem. Chem. Phys.*, 2012, **14**, 11119–11124.
- [87] W.-J. Yin, S.-H. Wei, M. M. Al-Jassim, J. Turner and Y. Yan, "Doping properties of monoclinic BiVO₄ studied by first-principles density-functional theory", *Phys. Rev. B*, 2011, **83**, 155102.
- [88] G. Wang, Y. Ling, X. Lu, F. Qian, Y. Tong, J. Z. Zhang, V. Lordi, C. Rocha Leao and Y. Li, "Computational and Photoelectrochemical Study of Hydrogenated Bismuth Vanadate", *The Journal of Physical Chemistry C*, 2013, **117**, 10957–10964.
- [89] L. Fitting Kourkoutis, Y. Hotta, T. Susaki, H. Y. Hwang and D. A. Muller, "Nanometer Scale Electronic Reconstruction at the Interface between LaVO₃ and LaVO₄", *Phys. Rev. Lett.*, 2006, **97**, 256803.
- [90] M. Chi, T. Mizoguchi, L. W. Martin, J. P. Bradley, H. Ikeno, R. Ramesh, I. Tanaka and N. Browning, "Atomic and electronic structures of the SrVO₃-LaAlO₃ interface", *Journal of Applied Physics*, 2011, **110**, 046104.
- [91] H. Wadati, D. G. Hawthorn, J. Geck, T. Z. Regier, R. I. R. Blyth, T. Higuchi, Y. Hotta, Y. Hikita, H. Y. Hwang and G. A. Sawatzky, "Interface reconstruction in V-oxide heterostructures determined by x-ray absorption spectroscopy", *Applied Physics Letters*, 2009, **95**, 023115.
- [92] V. A. Morozov, A. V. Arakcheeva, G. Chapuis, N. Guiblin, M. D. Rossell and G. Van Tendeloo, "KNd(MoO₄)₂: A New Incommensurate Modulated Structure in the Scheelite Family", *Chemistry of Materials*, 2006, **18**, 4075–4082.

- [93] V. A. Morozov, A. V. Mironov, B. I. Lazoryak, E. G. Khaikina, O. M. Basovich, M. D. Rossell and G. V. Tendeloo, “Ag_{1/8}Pr_{5/8}MoO₄: An incommensurately modulated scheelite-type structure”, *Journal of Solid State Chemistry*, 2006, **179**, 1183–1191.
- [94] V. Babin, P. Bohacek, A. Krasnikov, M. Nikl, A. Stolovits and S. Zazubovich, “Origin of green luminescence in PbWO₄ crystals”, *Journal of Luminescence*, 2007, **124**, 113–119.
- [95] Z. Zhao, Z. Li and Z. Zou, “Electronic structure and optical properties of monoclinic clinobisvanite BiVO₄”, *Phys. Chem. Chem. Phys.*, 2011, **13**, 4746–4753.
- [96] K. Ding, B. Chen, Z. Fang and Y. Zhang, “Density functional theory study on the electronic and optical properties of three crystalline phases of BiVO₄”, *Theoretical Chemistry Accounts*, 2013, **132**, 1352.
- [97] J. K. Cooper, S. Gul, F. M. Toma, L. Chen, P.-A. Glans, J. Guo, J. W. Ager, J. Yano and I. D. Sharp, “Electronic Structure of Monoclinic BiVO₄”, *Chemistry of Materials*, 2014, **26**, 5365–5373.
- [98] M. Arai, *wien2venus.py*. Available from: <http://www.nims.go.jp/cmsc/staff/arai/wien/venus.html>.
- [99] R. F. W. Bader, “in Atoms in Molecules: A Quantum Theory; Oxford University Press: New York”, 1990.
- [100] G. Henkelman, A. Arnaldsson and H. Jónsson, “A fast and robust algorithm for Bader decomposition of charge density”, *Computational Materials Science*, 2006, **36**, 354–360.
- [101] R. Vidya, P. Ravindran, K. Knizek, A. Kjekshus and H. Fjellvåg, “Density Functional Theory Studies of Spin, Charge, and Orbital Ordering in YBaT₂O₅ (T = Mn, Fe, Co)”, *Inorganic Chemistry*, 2008, **47**, 6608–6620.
- [102] Y. Wang, S. Lee, L. Zhang, S. Shang, L.-Q. Chen, A. Derecskei-Kovacs and Z.-K. Liu, “Quantifying charge ordering by density functional theory: Fe₃O₄ and CaFeO₃”, *Chemical Physics Letters*, 2014, **607**, 81–84.

Bibliography

- [103] M. Han, T. Sun, P. Y. Tan, X. Chen, O. K. Tan and M. S. Tse, “m-BiVO₄ γ -Bi₂O₃ core-shell p-n heterogeneous nanostructure for enhanced visible-light photocatalytic performance”, *RSC Adv.*, 2013, **3**, 24964–24970.
- [104] F. F. Abdi, L. Han, A. H. M. Smets, M. Zeman, B. Dam and R. V. D. Krol, “Efficient solar water splitting by enhanced charge separation in a bismuth vanadate-silicon tandem photoelectrode”, *Nature Communications*, 2013, **4**, 2195.
- [105] P. Agrawal, J. Guo, P. Yu, C. Hébert, D. Passerone, R. Erni and M. D. Russell, “Strain-driven oxygen deficiency in multiferroic SrMnO₃ thin films”, *Phys. Rev. B*, 2016, **94**, 104101.
- [106] N. A. Hill, “Why Are There so Few Magnetic Ferroelectrics?”, *The Journal of Physical Chemistry B*, 2000, **104**, 6694–6709.
- [107] D. A. Khomskii, “Trend: Classifying multiferroics: Mechanisms and effects”, *Physics*, 2009, **2**, 20.
- [108] C. J. Fennie and K. M. Rabe, “Magnetic and Electric Phase Control in Epitaxial EuTiO₃ from First Principles”, *Phys. Rev. Lett.*, 2006, **97**, 267602.
- [109] T. Katsufuji and H. Takagi, “Coupling between magnetism and dielectric properties in quantum paraelectric EuTiO₃”, *Phys. Rev. B*, 2001, **64**, 054415.
- [110] J. H. Lee, L. Fang, E. Vlahos, X. Ke, Y. W. Jung, L. F. Kourkoutis, J.-W. Kim, P. J. Ryan, T. Heeg, M. Roeckerath, V. Goian, M. Bernhagen, R. Uecker, P. C. Hammel, K. M. Rabe, S. Kamba, J. Schubert, J. W. Freeland, D. A. Muller, C. J. Fennie, P. Schiffer, V. Gopalan, E. Johnston-Halperin and D. G. Schlom, “A strong ferroelectric ferromagnet created by means of spin-lattice coupling”, *Nature*, **466**, 954–958.
- [111] T. Birol, N. A. Benedek, H. Das, A. L. Wysocki, A. T. Mulder, B. M. Abbett, E. H. Smith, S. Ghosh and C. J. Fennie, “The magnetoelectric effect in transition metal oxides: Insights and the rational design of new materials from first principles”, *Current Opinion in Solid State and Materials Science*, 2012, **16**, 227–242.

- [112] J. H. Lee and K. M. Rabe, “Epitaxial-Strain-Induced Multiferroicity in SrMnO₃ from First Principles”, *Phys. Rev. Lett.*, 2010, **104**, 207204.
- [113] R. Guzmán, L. Maurel, E. Langenberg, A. R. Lupini, P. A. Algarabel, J. A. Pardo and C. Magén, “Polar-Graded Multiferroic SrMnO₃ Thin Films”, *Nano Letters*, 2016, **16**, 2221–2227.
- [114] S. Kamba, V. Goian, V. Skoromets, J. Hejtmánek, V. Bovtun, M. Kempa, F. Borodavka, P. Vaněk, A. A. Belik, J. H. Lee, O. Pacherová and K. M. Rabe, “Strong spin-phonon coupling in infrared and Raman spectra of SrMnO₃”, *Phys. Rev. B*, 2014, **89**, 064308.
- [115] T. Takeda and S. Ōhara, “Magnetic Structure of the Cubic Perovskite Type SrMnO₃”, *Journal of the Physical Society of Japan*, 1974, **37**, 275–275.
- [116] K. Kikuchi, H. Chiba, M. Kikuchi and Y. Syono, “Syntheses and Magnetic Properties of La_{1-x}Sr_xMnO_y (0.5 ≤ x ≤ 1.0) Perovskite”, *Journal of Solid State Chemistry*, 1999, **146**, 1–5.
- [117] O. Chmaissem, B. Dabrowski, S. Kolesnik, J. Mais, D. E. Brown, R. Kruk, P. Prior, B. Pyles and J. D. Jorgensen, “Relationship between structural parameters and the Néel temperature in Sr_{1-x}Ca_xMnO₃ (0 < x < 1) and Sr_{1-y}Ba_yMnO₃ (y < 0.2)”, *Phys. Rev. B*, 2001, **64**, 134412.
- [118] R. Søndena, P. Ravindran, S. Stølen, T. Grande and M. Hanfland, “Electronic structure and magnetic properties of cubic and hexagonal SrMnO₃”, *Phys. Rev. B*, **74**, 144102.
- [119] M. Abbate, F. M. F. de Groot, J. C. Fuggle, A. Fujimori, O. Strebel, F. Lopez, M. Domke, G. Kaindl, G. A. Sawatzky, M. Takano, Y. Takeda, H. Eisaki and S. Uchida, “Controlled-valence properties of La_{1-x}Sr_xFeO₃ and La_{1-x}Sr_xMnO₃ studied by soft-x-ray absorption spectroscopy”, *Phys. Rev. B*, 1992, **46**, 4511–4519.
- [120] H. Kurata and C. Colliex, “Electron-energy-loss core-edge structures in manganese oxides”, *Phys. Rev. B*, 1993, **48**, 2102–2108.

Bibliography

- [121] H. L. Ju, H.-C. Sohn and K. M. Krishnan, “Evidence for O_{2p} Hole-Driven Conductivity in $\text{La}_{1-x}\text{Sr}_x\text{MnO}_3$ ($0 \leq x \leq 0.7$) and $\text{La}_{0.7}\text{Sr}_{0.3}\text{MnO}_z$ Thin Films”, *Phys. Rev. Lett.*, 1997, **79**, 3230–3233.
- [122] M. Varela, M. P. Oxley, W. Luo, J. Tao, M. Watanabe, A. R. Lupini, S. T. Pantelides and S. J. Pennycook, “Atomic-resolution imaging of oxidation states in manganites”, *Phys. Rev. B*, 2009, **79**, 085117.
- [123] C. Loschen, J. Carrasco, K. M. Neyman and F. Illas, “First-principles LDA+U and GGA + U study of cerium oxides: Dependence on the effective U parameter”, *Phys. Rev. B*, 2007, **75**, 035115.
- [124] A. Marthinsen, C. Faber, U. Aschauer, N. A. Spaldin and S. M. Selbach, “Coupling and competition between ferroelectricity, magnetism, strain, and oxygen vacancies in AMnO_3 perovskites”, *MRS Communications*, 2016, **6**, 182–191.
- [125] C. Becher, L. Maurel, U. Aschauer, M. Lilienblum, C. Magén, D. Meier, E. Langenberg, M. Trassin, J. Blasco, I. P. Krug, P. A. Algarabel, N. A. Spaldin, J. A. Pardo and M. Fiebig, “Strain-induced coupling of electrical polarization and structural defects in SrMnO_3 films”, *Nature Nanotechnology*, **10**, 661–665.
- [126] K. Mukhopadhyay, A. Mahapatra and P. Chakrabarti, “Multiferroic behavior, enhanced magnetization and exchange bias effect of Zn substituted nanocrystalline LaFeO_3 ($\text{La}_{(1-x)}\text{Zn}_x\text{FeO}_3$, $x=0.10$, and 0.30)”, *Journal of Magnetism and Magnetic Materials*, 2013, **329**, 133–141.
- [127] L. Liu, K. Sun, X. Li, M. Zhang, Y. Liu, N. Zhang and X. Zhou, “A novel doped CeO_2 - LaFeO_3 composite oxide as both anode and cathode for solid oxide fuel cells”, *International Journal of Hydrogen Energy*, 2012, **37**, 12574–12579.
- [128] P. Song, Q. Wang, Z. Zhang and Z. Yang, “Synthesis and gas sensing properties of biomorphic LaFeO_3 hollow fibers templated from cotton”, *Sensors and Actuators B: Chemical*, 2010, **147**, 248–254.
- [129] P. Tang, Y. Tong, H. Chen, F. Cao and G. Pan, “Microwave-assisted synthesis of nanoparticulate perovskite LaFeO_3 as a high active visible-light photocatalyst”, *Current Applied Physics*, 2013, **13**, 340–343.

- [130] K. Parida, K. Reddy, S. Martha, D. Das and N. Biswal, "Fabrication of nanocrystalline LaFeO₃: An efficient sol-gel auto-combustion assisted visible light responsive photocatalyst for water decomposition", *International Journal of Hydrogen Energy*, 2010, **35**, Bio-Ethanol and Other Renewable Sources and Reforming Process for Sustainable Hydrogen Production, 12161–12168.
- [131] X.-D. Zhou, Q. Cai, J. Yang, M. Kim, W. B. Yelon, W. J. James, Y.-W. Shin, B. J. Scarfino and H. U. Anderson, "Coupled electrical and magnetic properties in (La,Sr)FeO_{3-δ}", *Journal of Applied Physics*, 2005, **97**, 10C314.
- [132] A. Chainani, M. Mathew and D. D. Sarma, "Electron spectroscopic investigation of the semiconductor-metal transition in La_{1-x}Sr_xFeO₃", *Phys. Rev. B*, 1993, **47**, 15397–15403.
- [133] D. D. Sarma, O. Rader, T. Kachel, A. Chainani, M. Mathew, K. Holldack, W. Gudat and W. Eberhardt, "Contrasting behavior of homovalent-substituted and hole-doped systems: O K-edge spectra from LaNi_{1-x}M_xO₃ (M=Mn, Fe, and Co) and La_{1-x}Sr_xMnO₃", *Phys. Rev. B*, 1994, **49**, 14238–14243.
- [134] A. Braun, D. Bayraktar, S. Erat, A. S. Harvey, D. Beckel, J. A. Purton, P. Holtappels, L. J. Gauckler and T. Graule, "Pre-edges in oxygen (1s) x-ray absorption spectra: A spectral indicator for electron hole depletion and transport blocking in iron perovskites", *Applied Physics Letters*, 2009, **94**, 202102.
- [135] S. Erat, A. Braun, A. Ovalle, C. Piamonteze, Z. Liu, T. Graule and L. J. Gauckler, "Correlation of O (1s) and Fe (2p) near edge x-ray absorption fine structure spectra and electrical conductivity of La_{1-x}Sr_xFe_{0.75}Ni_{0.25}O_{3-δ}", *Applied Physics Letters*, 2009, **95**, 174108.
- [136] S. Erat, "On the Origin of Enhanced Conductivity in LaSrFe-Oxide upon Ni-Doping: Correlation of Electronic Structure and Transport Properties.", *Diss Eidgenöss. Tech. Hochsch. ETH Zür.*, 2010, **Nr 19155**.
- [137] S. Erat, A. Braun, C. Piamonteze, Z. Liu, A. Ovalle, H. Schindler, T. Graule and L. J. Gauckler, "Entanglement of charge transfer, hole doping, exchange interaction, and octahedron tilting angle and their influence on the conduc-

Bibliography

- tivity of $\text{La}_{1-x}\text{Sr}_x\text{Fe}_{0.75}\text{Ni}_{0.25}\text{O}_{3-\delta}$: A combination of x-ray spectroscopy and diffraction”, *Journal of Applied Physics*, 2010, **108**, 124906.
- [138] A. Larson and R. V. Dreele, “General Structure Analysis System (GSAS)”, *Los Alamos National Laboratory Report LAUR*, 2000, 86–748.
- [139] B. H. Toby, “EXPGUI, a graphical user interface for GSAS”, *J. Appl. Cryst.*, 2001, **34**, 210–213.
- [140] A. M. Glazer, “The classification of tilted octahedra in perovskites”, *Acta Crystallographica Section B*, 1972, **28**, 3384–3392.
- [141] P. Giannozzi, S. Baroni, N. Bonini, M. Calandra, R. Car, C. Cavazzoni, D. Ceresoli, G. L. Chiarotti, M. Cococcioni, I. Dabo, A. D. Corso, S. de Gironcoli, S. Fabris, G. Fratesi, R. Gebauer, U. Gerstmann, C. Gougoussis, A. Kokalj, M. Lazzeri, L. Martin-Samos, N. Marzari, F. Mauri, R. Mazzarello, S. Paolini, A. Pasquarello, L. Paulatto, C. Sbraccia, S. Scandolo, G. Sclauzero, A. P. Seitsonen, A. Smogunov, P. Umari and R. M. Wentzcovitch, “QUANTUM ESPRESSO: a modular and open-source software project for quantum simulations of materials”, *Journal of Physics: Condensed Matter*, 2009, **21**, 395502.
- [142] B. Himmetoglu, A. Floris, S. de Gironcoli and M. Cococcioni, “Hubbard-corrected DFT energy functionals: The LDA+U description of correlated systems”, *International Journal of Quantum Chemistry*, 2014, **114**, 14–49.
- [143] G. Catalan and J. F. Scott, “Physics and Applications of Bismuth Ferrite”, *Advanced Materials*, 2009, **21**, 2463–2485.
- [144] M. Polomska, W. Kaczmarek and Z. Pająk, “Electric and magnetic properties of $(\text{B}_{1-x}\text{La}_x)\text{FeO}_3$ solid solutions”, *physica status solidi (a)*, 1974, **23**, 567–574.
- [145] I. Sosnowska, M. Azuma, R. Przeniosło, D. Wardecki, W.-t. Chen, K. Oka and Y. Shimakawa, “Crystal and Magnetic Structure in Co-Substituted BiFeO_3 ”, *Inorganic Chemistry*, 2013, **52**, 13269–13277.
- [146] G. L. Yuan, S. W. Or, J. M. Liu and Z. G. Liu, “Structural transformation and ferroelectromagnetic behavior in single-phase $\text{Bi}_{1-x}\text{Nd}_x\text{FeO}_3$ multiferroic ceramics”, *Applied Physics Letters*, 2006, **89**, 052905.

- [147] Y.-K. Jun and S.-H. Hong, “Dielectric and magnetic properties in Co- and Nb-substituted BiFeO₃ ceramics”, *Solid State Communications*, 2007, **144**, 329–333.
- [148] R. J. Zeches, M. D. Rossell, J. X. Zhang, A. J. Hatt, Q. He, C.-H. Yang, A. Kumar, C. H. Wang, A. Melville, C. Adamo, G. Sheng, Y.-H. Chu, J. F. Ihlefeld, R. Erni, C. Ederer, V. Gopalan, L. Q. Chen, D. G. Schlom, N. A. Spaldin, L. W. Martin and R. Ramesh, “A Strain-Driven Morphotropic Phase Boundary in BiFeO₃”, *Science*, 2009, **326**, 977–980.
- [149] H. Béa, B. Dupé, S. Fusil, R. Mattana, E. Jacquet, B. Warot-Fonrose, F. Wilhelm, A. Rogalev, S. Petit, V. Cros, A. Anane, F. Petroff, K. Bouzouhane, G. Geneste, B. Dkhil, S. Lisenkov, I. Ponomareva, L. Bellaiche, M. Bibes and A. Barthélémy, “Evidence for Room-Temperature Multiferroicity in a Compound with a Giant Axial Ratio”, *Phys. Rev. Lett.*, 2009, **102**, 217603.
- [150] V. Shelke, G. Srinivasan and A. Gupta, “Ferroelectric properties of BiFeO₃ thin films deposited on substrates with large lattice mismatch”, *physica status solidi (RRL) – Rapid Research Letters*, 2010, **4**, 79–81.
- [151] A. Y. Emelyanov and N. A. Pertsev, “Abrupt changes and hysteretic behavior of 90° domains in epitaxial ferroelectric thin films with misfit dislocations”, *Phys. Rev. B*, 2003, **68**, 214103.
- [152] M. D. Rossell, R. Erni, M. P. Prange, J.-C. Idrobo, W. Luo, R. J. Zeches, S. T. Pantelides and R. Ramesh, “Atomic Structure of Highly Strained BiFeO₃ Thin Films”, *Phys. Rev. Lett.*, 2012, **108**, 047601.
- [153] P. S.S. R. Krishnan, J. A. Aguiar, Q. M. Ramasse, D. M. Kepaptsoglou, W.-I. Liang, Y.-H. Chu, N. D. Browning, P. Munroe and V. Nagarajan, “Mapping strain modulated electronic structure perturbations in mixed phase bismuth ferrite thin films”, *J. Mater. Chem. C*, 2015, **3**, 1835–1845.
- [154] C. Ederer and N. A. Spaldin, “Influence of strain and oxygen vacancies on the magnetoelectric properties of multiferroic bismuth ferrite”, *Phys. Rev. B*, 2005, **71**, 224103.

Bibliography

- [155] Y. Y. Liu, L. Yang and J. Y. Li, “Strain-engineered orthorhombic-rhombohedral phase boundary in epitaxial bismuth ferrite films”, *Journal of Applied Physics*, 2013, **113**, 183524.
- [156] A. Lubk, M. D. Rossell, J. Seidel, Y. H. Chu, R. Ramesh, M. J. Hÿtch and E. Snoeck, “Electromechanical Coupling among Edge Dislocations, Domain Walls, and Nanodomains in BiFeO₃ Revealed by Unit-Cell-Wise Strain and Polarization Maps”, *Nano Letters*, 2013, **13**, 1410–1415.
- [157] I. D. Brown, “Recent Developments in the Methods and Applications of the Bond Valence Model”, *Chemical Reviews*, 2009, **109**, 6858–6919.
- [158] S. Liu, I. Grinberg and A. M. Rappe, “Development of a bond-valence based interatomic potential for BiFeO₃ for accurate molecular dynamics simulations”, *Journal of Physics: Condensed Matter*, 2013, **25**, 102202.
- [159] S. Plimpton, “Fast Parallel Algorithms for Short-Range Molecular Dynamics”, *Journal of Computational Physics*, 1995, **117**, 1–19.
- [160] <http://lammps.sandia.gov>.
- [161] V. Grillo and E. Rotunno, “STEM_CELL: A software tool for electron microscopy: Part I - simulations”, *Ultramicroscopy*, 2013, **125**, 97–111.
- [162] J. J. Rehr, J. J. Kas, F. D. Vila, M. P. Prange and K. Jorissen, “Parameter-free calculations of X-ray spectra with FEFF9”, *Phys. Chem. Chem. Phys.*, 2010, **12**, 5503–5513.
- [163] N. Bologna, P. Agrawal, M. Campanini, M. Knödler, M. D. Rossell, R. Erni and D. Passerone, “Stair-rod dislocation cores acting as nanochannels for monodimensional carrier transport in GaAs nanowires”, *submitted*, 2017.
- [164] X. Duan, C. Niu, V. Sahi, J. Chen, J. W. Parce, S. Empedocles and J. L. Goldman, “High-performance thin-film transistors using semiconductor nanowires and nanoribbons”, *Nature*, 2003, **425**, 274–278.
- [165] X. Jiang, Q. Xiong, S. Nam, F. Qian, Y. Li and C. M. Lieber, “InAs/InP Radial Nanowire Heterostructures as High Electron Mobility Devices”, *Nano Letters*, 2007, **7**, 3214–3218.

- [166] S. Assali, I. Zardo, S. Plissard, D. Kriegner, M. A. Verheijen, G. Bauer, A. Meijerink, A. Belabbes, F. Bechstedt, J. E. M. Haverkort and E. P.A. M. Bakkers, “Direct Band Gap Wurtzite Gallium Phosphide Nanowires”, *Nano Letters*, 2013, **13**, 1559–1563.
- [167] G. Signorello, E. Lörtscher, P. A. Khomyakov, S. Karg, D. L. Dheeraj, B. Gotsmann, H. Weman and H. Riel, “Inducing a direct-to-pseudodirect bandgap transition in wurtzite GaAs nanowires with uniaxial stress”, *Nature Communications*, 2014, **5**, ncomms4655.
- [168] J. V. Holm, H. I. Jørgensen, P. Krogstrup, J. Nygård, H. Liu and M. Aagesen, “Surface-passivated GaAsP single-nanowire solar cells exceeding 10% efficiency grown on silicon”, *Nature Communications*, 2013, **4**, ncomms2510.
- [169] K. Tomioka, M. Yoshimura and T. Fukui, “A III-V nanowire channel on silicon for high-performance vertical transistors”, *Nature*, 2012, **488**, 189–192.
- [170] M. de la Mata, C. Magén, P. Caroff and J. Arbiol, “Atomic Scale Strain Relaxation in Axial Semiconductor III-V Nanowire Heterostructures”, *Nano Letters*, 2014, **14**, 6614–6620.
- [171] A. M. Ionescu and H. Riel, “Tunnel field-effect transistors as energy-efficient electronic switches”, *Nature*, 2011, **479**.
- [172] C. Thelander, P. Agarwal, S. Brongersma, J. Eymery, L. Feiner, A. Forchel, M. Scheffler, W. Riess, B. Ohlsson, U. Gösele and L. Samuelson, “Nanowire-based one-dimensional electronics”, *Materials Today*, 2006, **9**, 28–35.
- [173] H. Ye, P. Lu, Z. Yu, Y. Song, D. Wang and S. Wang, “Critical Thickness and Radius for Axial Heterostructure Nanowires Using Finite-Element Method”, *Nano Letters*, 2009, **9**, 1921–1925.
- [174] F. Glas, “Critical dimensions for the plastic relaxation of strained axial heterostructures in free-standing nanowires”, *Phys. Rev. B*, 2006, **74**, 121302.
- [175] S. Raychaudhuri and E. T. Yu, “Critical dimensions in coherently strained coaxial nanowire heterostructures”, *Journal of Applied Physics*, 2006, **99**, 114308.

Bibliography

- [176] S Bernal, F Botana, J. Calvino, C López-Cartes, J. Pérez-Omil and J. Rodríguez-Izquierdo, “The interpretation of HREM images of supported metal catalysts using image simulation: profile view images”, *Ultramicroscopy*, 1998, **72**, 135–164.
- [177] J. A. Pérez-Omil, *Univ. Cadiz*, 1994.
- [178] *CP2K Version 3.0. CP2K Is Freely Available from www.cp2k.org*.
- [179] M. Guidon, J. Hutter and J. VandeVondele, “Auxiliary Density Matrix Methods for Hartree-Fock Exchange Calculations”, *Journal of Chemical Theory and Computation*, 2010, **6**, 2348–2364.
- [180] I. Souza, N. Marzari and D. Vanderbilt, “Maximally localized Wannier functions for entangled energy bands”, *Phys. Rev. B*, 2001, **65**, 035109.
- [181] V. Grillo and F. Rossi, “STEM_CELL: A software tool for electron microscopy. Part 2 analysis of crystalline materials”, *Ultramicroscopy*, 2013, **125**, 112–129.
- [182] M. J. Hÿtch, E. Snoeck and R. Kilaas, “Quantitative measurement of displacement and strain fields from HREM micrographs”, *Ultramicroscopy*, 1998, **74**, 131–146.
- [183] N. Ashcroft and N. Mermin, *Solid State Physics*, Cengage Learning, 2011.
- [184] M. Gibertini and N. Marzari, “Emergence of One-Dimensional Wires of Free Carriers in Transition-Metal-Dichalcogenide Nanostructures”, *Nano Letters*, 2015, **15**, 6229–6238.

List of Publications:

- Zhang Y., Guerra-Nunez, C., Utke, I., Michler, J., **Agrawal, P.**, Rossell, M. D. and Erni R. Atomic Layer Deposition of Titanium Oxide on Single Layer Graphene: an Atomic Scale Study towards Understanding Nucleation and Growth. *Chem. Mater.* 2017, 29(5), 2232-2238.
- **Agrawal, P.**; Guo, J.; Yu, P.; Hébert, C.; Passerone, D.; Erni, R.; Rossell, M. D. Strain-Driven Oxygen Deficiency in Multiferroic SrMnO₃ Thin Films. *Phys. Rev. B* 2016, 94 (10), 104101.
- **Agrawal, P.**, Rossell, M. D., Hébert, C., Passerone, D. and Erni, R. 2016. Dislocation Modelling: Calculating EELS Spectra for Edge Dislocation in Bismuth Ferrite. *European Microscopy Congress 2016: Proceedings*. 797–798.
- Rossell, M. D.; **Agrawal, P.**; Borgschulte, A.; Hébert, C.; Passerone, D.; Erni, R. Direct Evidence of Surface Reduction in Monoclinic BiVO₄. *Chem. Mater.* 2015, 27 (10), 3593–3600.

In progress:

1. Stair-rod dislocation cores acting as localized potential channels in GaAs nanowires simulated potential cores in GaAs nanowires.
2. Atomic structure and electronic properties of planar defects in oxygen-deficient SrFeO_{3-δ} thin films.
3. Electronic structure of homovalent Ni substituted LaFeO₃ from near edge x-ray absorption fine structure spectra and first-principle calculations.
4. Investigation of electronic structure of edge dislocation core in BiFeO₃

Publications before PhD:

- **Agrawal, P.**; Tkatchenko, A.; Kronik, L. Pair-Wise and Many-Body Dispersive Interactions Coupled to an Optimally Tuned Range-Separated Hybrid Functional. *J. Chem. Theory Comput.* 2013, 9 (8), 3473–3478.
- Sepunaru, L.; Refaely-Abramson, S.; Lovrinčić, R.; Gavrilov, Y.; **Agrawal, P.**; Levy, Y.; Kronik, L.; Pecht, I.; Sheves, M.; Cahen, D. Electronic Transport via Homopeptides: The Role of Side Chains and Secondary Structure. *J. Am. Chem. Soc.* 2015, 137 (30), 9617–9626.

Piyush Agrawal



Date of birth: 30 September 1989

Birth Place: Jodhpur, India

Email ID: piyushjunjanuwala@gmail.com

Nationality: Indian

Education:

Nov 2013 – Dec 2017: **Degree:** Doctorate in Physics

University: École polytechnique fédérale de Lausanne, EPFL, Switzerland

Thesis title: Defects in Materials – Structural Determination and exploiting their electronic structure properties based on theoretical and experimental Electron Energy Loss Spectra

Supervisors: Prof. Cecile Hébert (EPFL), Dr. Rolf Erni and Dr. Daniele Passerone (EMPA)

Aug 2007 – May 2013: **Degree:** Integrated Bachelors and Masters of Science

University: Indian Institute of Science Education and Research, IISER, Pune

Master thesis at Weizmann Institute of Science, Israel: Pair-wise dispersive correction of an optimally-tuned range-separated hybrid functional

Supervisor: Prof. Leeor Kronik

Courses: Courses in Basic Sciences with Physics and Chemistry as major disciplines

Research Experience:

March 2012 – June 2013: Weizmann Institute of Science, Israel
Visiting Researcher

Propose a nonempirical, pair-wise or many-body dispersion-corrected, optimally tuned range-separated hybrid functional. This functional retains the advantages of the optimal-tuning approach in the prediction of the electronic structure. At the same time, it gains accuracy in the prediction of binding energies for dispersively bound systems, as benchmark on sets of weakly bound dimers.

March 2010 – Dec 2010: IICT, Hyderabad
Research Intern

A multi-step structure-based virtual screening approach has been employed to identify novel and selective GSK-3 β inhibitors. Initial screening was performed on 12,000,000 chemical compounds present in all-purchasable subset of ZINC database, which represents huge diversity. Identified compounds were clustered into six scaffolds based on chemical structure and validation of their inhibitory potential was done by molecular dynamics simulation.

IT Skills:

- Programming languages: Python, Shell scripting, C++, MATLAB
- Simulation packages: AutoDock CCDC – GOLD; Schrodinger packages –Glide, Desmond;
- Quantum Simulation codes: GAUSSIAN, NWChem, Q-Chem, CP2k, WIEN2k, FEFF
- Molecular Dynamics: LAMMPS, CHARMM
- Visualisation Packages: Material Studio, PyMOL, MOE, Jmol, VMD, Vesta, XCrySDen

Awards and Honors:

- Travel grants for conferences
- Visiting Student Fellowship in Israel
- INSPIRE Fellow during graduate studies

